Alma Mater Studiorum – Università di Bologna

DOTTORATO DI RICERCA IN

SCIENZE E TECNOLOGIE DELLA SALUTE

Ciclo 34

Settore Concorsuale: 03/C2 – CHIMICA INDUSTRIALE

Settore Scientifico Disciplinare: CHIM/04 – CHIMICA INDUSTRIALE

NANOSTRUCTURED SMART MATERIALS AS FUNCIONAL COMPONENTS OF MEDICAL DEVICES

Presentata da: Maria Elena Gino

Coordinatore Dottorato

Marco Viceconti

Supervisore

Maria Letizia Focarete

Co-supervisore

Henk van de Meent
Andrei Kholkin

Esame finale anno 2022

Preface

The present research project is focused on the development of nanostructured composite materials, in which a component is an intelligent material, for possible applications as functional elements of advanced medical devices. The electrospinning process is the main technological process used to produce the functional component.

During the three-years Ph.D. period, I worked on three different research topics having in common the development of smart functional materials.

The discussion of the dissertation will be therefore composed of three main sections:

i. PZT based piezoelectric devices
ii. PVDF-TrFE based piezoelectric devices
iii. Polymeric nanofibers for flexible electronics

In sections (i) and (ii) piezoelectric composite materials based on ceramic and polymeric fillers, respectively, were investigated. In particular, lead zirconate titanate (PZT) and poly(vinylidene fluoride-trifluoroethylene) (PVDF-TrFE) were chosen to introduce the smart elements into the composite material. I dedicated the majority of my time to this research activity, related to the European Project H2020-ICT-25-2017 "*MY LEG*: *Smart and intuitive osseointegrated transfemoral prostheses embodying advanced dynamic behaviours*", under the guidance of Prof. M.L. Focarete.

Due to the project's interdisciplinary nature, experts from fields other than polymer science, such as mechanical and electrical engineering, collaborated on the research. In particular, knowledge of polymer science has been applied to synthesize and produce the smart element while the engineers contributed to the final fabrication of the composite material and to test the functionality for possible applications such as components of advanced prostheses in the aforementioned project. Specifically, thanks to the collaboration of Prof. A. Zucchelli, dr. T. Brugo and their research groups of the Industrial Engineering Department and Prof. D. Fabiani and Ph.D student G. Selleri of the Department of Electrical, Electronic, and Information Engineering it was possible to develop two types of piezo-laminate composites usable as sensors in MY LEG project.

In section (iii), a wavy nanofibrous polymeric network produced through the electrospinning was developed. The nanofiber mesh showed a tuneable mechanical response as a function of the applied stress when it was incorporated in an elastomeric matrix. This work was carried out in collaboration with Prof. T. Cramer and his research group at the Physics and Astronomy Department.

Table of contents

Abstract

The medical devices sector is rapidly growing thanks to the collaboration between different disciplines of the industry and academia, such as biology, engineering, and materials science, to develop devices to monitor, diagnose and treat diseases, thus improving the quality of life of patients. Wearable medical devices with customized functions and features, to monitor physiological parameters, play an important role to detect particular medical conditions and bring innovation in healthcare applications. High sensitivity, excellent mechanical properties, and optimal electronic performance are required for this kind of medical devices. These features can be achieved by exploiting composite materials based on nanostructured smart materials, that due to the inherent characteristics of single constituents (smart materials used as nanostructured filler and polymer matrix) develop unique properties that make them suitable for different applications such as wearable electronics, energy storage, and conversion.

The present Ph.D. Thesis aims at designing, fabricating, and characterizing nanostructured smart materials embedded into a polymeric matrix to obtain a composite material that can be used as a functional component for medical devices.

In particular, it has been demonstrated that the obtained composite materials:

(i) based on nanostructured piezoelectric smart material, ceramic (i.e. lead zirconate titanate) and polymeric (i.e. poly(vinylidene fluoride-trifluoroethylene), can be used as pressure sensors;

(ii) based on a nanostructured network of Poly-L-lactic acid (PLLA) made of curled nanofibers, can present a tuneable mechanical response as a function of the applied stress. For this reason, such material could be used to solve the issue relative to the mechanical discrepancy between rigid electronic materials/soft human tissues/different material of the device.

In the course of the present research activity, PZT nanofibers with specific composition $Pb(Zr_{0,52}Ti_{0,48})O_3$ were obtained by sol-gel electrospinning starting from synthetized PZT precursor solution. Synthesis, sol-gel electrospinning process, and subsequent thermal treatment were accurately controlled to obtain PZT nanofibers dimensionally stable with densely packed grains in the perovskite phase. However, to laid the foundations for understanding the piezoelectric behaviour and defining guidelines for the manufacture of pressure-sensitive PZT composites, PZT powder was chosen for its availability, simple production, and possibility to obtain it in large amounts quantity.

A non-invasive method for the piezoelectric functionalization of composite laminates was developed by interleaving PZT micrometric powder between Glass Fiber Reinforced Polymer

(GFRP) plies. The effect of different powder volume fractions and different morphology (powder vs bulk) on the electromechanical properties was explored in terms of electrical response and laminate inherent strength. Experimental results showed that the PZT powder laminates present greater sensitivity and impact resistance than the PZT bulk material integrated into the laminated composite.

Furthermore, an analytical model was suggested to predict the piezoelectric voltage coefficient g_{33} as a function of the electrical properties, powder volumetric fractions, and polarization process. The model matches the experimental g_{33} coefficients ($R^2 = 0.97$), demonstrating its capability to predict the electromechanical behaviour of piezoelectric composites and to define their design guidelines.

The electrospinning process was employed also to produce PVDF-TrFE electrospun mat. Thanks to electrospinning, the strong electrostatic uniaxial stretching introduces elongation forces in the direction of the jet that promotes the formation of the crystalline phase, while the porosity of the nanofibrous membrane prevents the delamination risk and increases the impact strength of the composite material when embedded in the hosting matrix.

The mechanical and electrical performances of the self-sensing laminate based on PVDF-TrFE nanofibers were preserved after 10^6 cycles of fatigue tests. Furthermore, the piezoelectric response of the piezoelectric nanofibrous sensors embedded in a prosthetic sole follows the ground reaction force with good sensitivity.

Since flexible electronics interact with biological tissues/organs and it is composed of different type of materials, the mechanical mismatch between traditional hard electronic materials and soft biological tissues and between different materials that constitute the electronics device, often lead to severe data acquisition errors and/or premature failure of the medical device. The design strategy used in this Thesis involves the use of a wavy nanofibrous network produced by electrospinning, that provides a high elastic modulus at large strain, limiting, therefore, the strain of the elastomeric matrix in which it is incorporated. Aligned nanofiber PLLA mats were prepared through electrospinning and by exploiting the interaction with plasticizer, curled nanofiber with different curvatures were generated. The obtained composite material based on a network with controlled curvature incorporated into a polymeric matrix (i.e Polydimethylsiloxane (PDMS), showing a specific stress-strain response, is promising for a comfortable integration of the stretchable electronics with the biological tissues/organs and at the same time, reduce the possibility of device failure.

1. Introduction

1.1. Current trend in medical devices innovation

An increase in the average age of the population together with the increasing development of chronic and/or degenerative disorders are the factors that are driving the medical devices market to its growth [1]. While wearable biomedical devices may interact with the human body intimately in an external contact, implantable devices are embedded inside the human body, directly and continuously in contact with organs and tissues. Nevertheless, both families of medical devices must fulfill the requirement of being biocompatible to result safe for the final user. In order to efficiently avoid exposure to biological tissues and fluids, a medical device can be encapsulated within known biocompatible materials [2]. These devices are attracting considerable attention for a wide variety of applications, including but not limited to diagnostic, monitoring, drug delivery, therapeutic application, rehabilitation, and surgery [3]. Flexibility and wearability features may expand the interest in medical devices as they can enlarge the range of applications beyond imagination, including smart wound dressing, electronic skin, flexible electronics, energy harvesting, and storage devices as well as implantable bioelectronics [4].

Indeed, thanks to advancements in design and production methods [5], various microelectronic and micromechanical sensors can now be integrated into a rigid or flexible substrate with good sensitivity at a relatively low cost in a small area [6]. The appropriately designed devices find applications of continuous monitoring of human health state to control the progression of the disease and thus deliver the necessary medications in time, leading to an improvement in human's life.

Existing medical devices are generally based on composite materials [7]. In this field, traditional composite materials are made of two or more constituent materials and designed to have new mechanical, physical and chemical proprieties superior to the individual elements are developed [8]. A particular class of composite materials used to achieve top performance are composed of continuous and oriented fibers, usually made of carbon or glass, embedded in a polymer matrix, typically a thermoplastic such as epoxy resin. When the fibers are 'pre-impregnated' in a partially cured matrix, these composite materials are called 'prepreg'. The high stiff fibers are oriented in specific direction to act as reinforced and the matrix is used to bond them together to form a ply. The fiber-reinforced composites are recently used in fabrication of prosthetic medical devices, thank of the possibility to design materials with

enhanced and tailored mechanical properties by selecting the material constituents (matrix and fiber) and their volume amounts [9].

Moreover, with the incorporation of more materials, as filler, is possible to provide to the composite materials, as the functionality actuators, energy harvesting systems and sensors to allow real-time supervision of the structure status (structural health monitoring, SHM), to determine accurate impact localization or monitoring the pressure distribution.

When a composite material has at least one phase which has nanometric dimensions (10^{-9} m), it is called *nanocomposite.* Commonly nanomaterials filler used for the production of nanocomposites are nanoparticles, nanofiber, and nanocluster [10].

The advantages of using nanomaterials as fillers are attributable to:

- A high ratio between surface area and volume,
- Enhanced mechanical properties (high ductility without strength loss and resistance),
- Specific proprieties (such as mechanical, electrical, optical, piezoelectrical) [11].

In this configuration, the polymer matrix serves mainly to bond the filler firmly, while the filler provides specifically designed functionality to make the final material "smart" [12].

The responsivity of smart materials to external stimuli (e.g., mechanical, chemical, electrical, or magnetic signals make them suitable as innovative sensors, actuators, smart textiles, thin and stretchable polymers for electronic skins and brain, micro-machined semiconductor, shape memory alloy-based actuators for bladder and polymer-based tactile sensors for prosthesis and so on [13].

Powering of active medical devices (especially implanted ones), is the main obstacle in healthcare technology. The need to create micro/nanosystems that are self-powered and can operate for long periods within/on the body without needing to be recharged led to the development of devices that harvest biomechanical energy from the body itself [14].

In summary, several critical elements must be considered when designing a smart medical device.

- The choice of the materials to be used will determine the characteristics of the final device and the ability to respond to different stimuli.
- Adequate mechanical properties (flexibility or stiffness according to the intended use)
- Biocompatibility and stability over time.

Therefore, a medical device must fulfill different requirements (functionality, safety, stability etc.) to be ultimately approved by world regulatory bodies (e.g. FDA for United States)[15].

An example of smart innovative medical devices is provided by the products developed in the MyLeg European project. As anticipated in the preface, sections (i) and (ii) of this Ph.D. project are performed in the framework of the European Project H2020 "MyLeg: Smart and intuitive osseointegrated transfemoral prostheses embodying advanced dynamic behaviors" which is focused on people undergoing amputation of the lower limb at the level of the femur above the knee. In the USA, lower-limb amputation is directly proportional to rates of peripheral arterial occlusive disease, neuropathy, and soft tissue sepsis. Amputation has a substantial impact on individual quality of life such as decreased mobility and increased energy consumption. The recovery of lost mobility remains a great challenge today. MyLeg project aims to develop and realize a transfemoral prosthesis osseointegrated able to incorporate advanced dynamic behaviours for the amputee. In particular, MyLeg prosthetic system will be equipped with sensors and energy harvesting realized with nanostructured materials, exploiting light-weighted nanofibrous materials, to guarantee more comfortable and intuitive use.

1.2. Functional component of medical devices

Medical devices refer to instruments, tools, machines, devices, in vitro reagents, implants, or other similar/related items, including accessories recognized by or components in the official national formulary, United States Pharmacopoeia (USP), or any supplement thereof [16].

Medical devices must meet specific requirements such as safety and biocompatibility and therefore, strict design and risk assessment before the equipment is interfaced with the human body must be carried out [16].

Smart electronic devices are essential in wearable health monitoring systems. In the past years, various configurations of sensors, including resistive sensors, piezoelectric devices, capacitive sensors, and harvesting system-based devices have demonstrated the capability of high sensitivity for monitoring human signals [17].

1.2.1. Sensors

During the last years, an increasing evolution in the development of wearable devices and monitoring devices appeared thanks to the great evolution of nanotechnology.

The wearable medical devices developed can collect information on several activities including heart rate, steps and calories burned, but there exist also sensors that pick up vital signs such as respiration rate, blood-oxygen levels, irregular heartbeats, pressure plantar, muscular activity, and others. Physical and physiological sensors are usually used as smart components for

applications of wearable consumer electronics, soft robotics, medical prosthetics, electronic skins, and real-time health monitoring [18]. However, this paragraph mainly focuses on approaches used to develop sensors for physical rehabilitation and health monitoring indicating the main types of pressure sensors currently being used for biomedical applications. Generally, to detect and quantify the desired physical data such as pressure, the physical sensors are designed to have variations in their electrical parameters, such as resistance, capacitance, or piezoelectricity [19] (Figure 1).

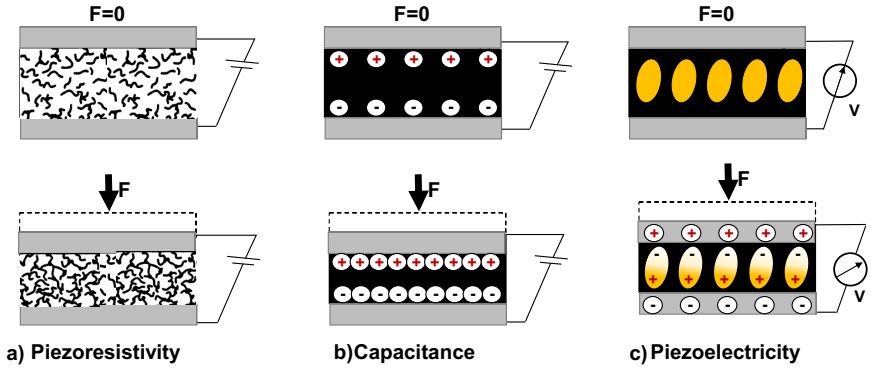

Figure 1: Schematic images of transduction force methods based on: piezoresitivity (a), capacitance (b), and piezoelectricity (c).

Typically, a sensor is based on a nanostructured composite material. Depending on the type of sensing activity, the material chosen can be a polymer, carbon, a semiconductor, and a metal present in different morphologies such as nanotubes, nanowires, nanofibers, nanoparticles, and many others. The choice of appropriate materials is crucial for developing sensors with great sensing capabilities. For the construction of pressure/strain sensors, materials with excellent electrical characteristics, mechanical compliance, large-area, and easy processing are needed[20][21]. Regardless of the type of transduction method of the sensors, changes in the electrical parameters of the majority of physical sensing platforms are induced by mechanical deformations experienced either directly by the sensing elements or imposed by the embedding matrix on the sensing components under an applied load [22].

Regardless of the type of sensors, performance must be evaluated. Some key parameters are sensitivity, limit of detection (LOD), linear response, response time, and stability at long periods. Sensitivity represents the amount of electrical charge that can be generated as a function of the applied force.

In general, pressure sensitivity is described as:

$$S = \frac{dX}{dP}$$

where S is the sensitivity, X provides quantitative output signal, and P defines the imposed external pressure.

LOD, is the threshold pressure, defined as the lowest pressure at which a signal variation is detectable.

A linear response is obtained when, across a specified operating scale, the output signal is proportional to the applied pressure, approximated to a straight line. In the linear operation range, the response to pressure is the most precise and accurate. As a result, a pressure sensor with large linear ranges is very desirable for practical applications.

Another important parameter to consider, especially when designing a dynamic real-time sensor, is the response time [23].

Several examples of resistive sensors are currently available; a resistive sensor consists of a conductive material that changes its geometry as a change in its resistance when an external force is applied. These materials are commonly manufactured by the incorporation of conductive carbon nanotubes (CNTs), silver nanoparticles, or nanowires as filler material, into a polymeric matrix such as polydimethylsiloxane (PDMS)/silicone, poly(styrene-butadiene-styrene) (SBS), fluorosilicone, and dimethacrylate-functionalized perfluoropolyether [21].

Herren et al [24] has developed a nanocomposite based on CNTs embedded into a PDMS elastomeric matrix. A high density of carbon nanotubes embedded in an elastomeric matrix offers unique properties to the final material, such as high flexibility, good carrier mobility, and high electrical conductivity, due to the possibility to create a network of CNTs where adjacent CNTs are electrically connected to each other forming conductive trajectories in the nanocomposite. By bending or deforming the device, the CNTs network follows the moving of matrix reducing the number of contacts between CNTs producing an increase in electrical resistance proportional to the applied deformation.

A sensor thus manufactured, is an example of a biocompatible and stretchable electronic device based on nanocomposite that can be used to monitor tissue deformation. The design of these electronic devices has been created to minimize the mechanical mismatch between stiff electronics and soft tissues [25]. Despite the ease of manufacture, the main problem related to these materials regards their electrical properties which are indeed linked with the viscoelastic nature of the matrix (as creep deformation and stress relaxation) as well as temperature dependency.

Capacitive sensors are generally manufactured by using two conductive layers as electrodes, which are separated by a dielectric material. After the application of a deformation force, the

change in thickness leads to capacitance variation. These sensors are suitable for monitoring high voltages. They are usually assembled into clothing, gloves, and stockings, to detect different types of human movements, such as walking, breathing, speaking, and emotional expressions [26]. Capacitive strain sensors base their transduction mechanism on the geometric change of a soft capacitor when deformed. A capacitive sensor is based on two parallel plates of a defined area (A) separated by an elastomer layer of distance (d) and dielectric constant (ε_r). Since elastomers are good dielectric materials, the result is a capacitor formed by two parallel plates that can be deformed without losing electrical conductivity. During deformation, the length of the capacitor will increase due to the applied voltage, while the width and distance between the plates will decrease, changing the capacitance. Jung et al. [27] designed a 3D porous dielectric elastomer-based flexible capacitive pressure sensor. Due to the microporous nature of the elastomeric dielectric layer, the device is extremely deformable even under low pressure, resulting in improved sensitivity. When the structured layer is compressed, the progressive closing of micropores can enhance the effective dielectric constant, improving sensor sensitivity. The major advantages of the capacitive sensors are the stable sensing performance, good dynamic response, and low power consumption. However, the sensitivity and response/relaxation time of capacitive pressure sensors present the same limitation as the resistive sensor, linked with elastomeric dielectrics[28].

Moreover, the output signal of these sensors is not proportional to the applied pressure. Piezoelectric sensors are based on piezoelectric smart material and employ the direct piezoelectric effect, by converting mechanical stress into an electrical signal. These sensors are usually based on different nanostructured materials such as ZnO, PVDF, and PZT active material, which have been demonstrated to possess rapid response, high sensitivity, own power, and linear response. Moreover, these inorganic piezoelectric materials show linear trend of operation, in a wide range of pressures and temperatures [29].

Piezoelectric materials, like lead zirconate titanate (PZT), are used for elastic waves detection thanks to their higher sensitivity as demonstrated by Saeedifar et al. attacking PZT wafer on surface of carbon fiber reinforced plastic (CFRP) composite plat [30], [31] or the PZT sensors can be embedded into the composite laminate to improve damage localization effectiveness, if compared to sensors attached on the outer surfaces, as demonstrated by Yang et al. [32]. Interleaving bulk materials, as PZT in form of disk or film, between composite plies, constitutes a defect which could induce matrix cracking and subsequent delamination of the composite laminate decreasing dramatically the strength of the hosting material [33].

Between main issues that lead to failure of composite laminate materials, the greatest contributing factors are provided of crack initiation and delamination. Embedding a sensor into the laminate material introduce a discontinuity causing interlaminar failure at that location.
However, changing the morphology of the PZT from disk to micro-filler as microfiber or micro powder, the intrusiveness of the sensor in the hosting laminate can be reduced.
Then, using smart material composite materials, based on piezoelectric material embedded in a laminate, is possible reduce alteration of the mechanical performance of the laminate avoiding environmental conditions and external noise could affect their proper working.

Other types of composite materials based on piezopolymers, are used in the biomedical field to create an interactive human-machine interface capable to collect information, monitoring biomechanical movements and human vital signals or can be integrated into fiber-reinforced plastics (FRP) composite laminates to expand the application such as industrial applications, civil engineering, aerospace, automotive due to their lightweight structure, high mechanical performance. Very interesting for each possible application is that the piezoelectric membrane possesses the requirement of being mechanically flexible, lightweight, low cost, easiness to fabricate, biocompatibility and allow operating without an external power source [34]. There are several examples of PVDF and copolymer-based devices used to continuously and accurately monitor physiological signals using pressure sensors because when a pressure is applied to the polymer, it causes a mechanical deformation and a displacement of charge. The charge generated from polymer is proportional to the pressure applied. The sensitivity and the wide range of frequency response, make PVDF and its copolymer an ideal candidate for the production of smart materials to be utilized to detect the strains or stresses induced by human activity (such as a nasal sensor for monitoring human respiration pattern, sensor for sleep apnea monitoring, monitoring cardiorespiratory signals [35], [36], blood pressure sensor [19][34].
PVDF polymer or its PVDF-TrFE copolymer can be chosen as a matrix and loaded with NPs of metal oxides and/or ceramics, to create a hybrid piezocomposite with improved performance that is used as a sensing element in high-performance biomedical applications. Although inorganic materials possess inferior flexibility and are more complex to manufacture in comparison to their organic counterparts, there are many inorganic nanomaterials, such as nanowires, which exhibit good mechanical flexibility. Therefore, piezoelectric NW arrays based on zinc oxide ZnO, In_2O_3, GeSi, GaAs, etc. have been widely explored to be used to design flexible pressure-sensing devices [19]. Dagdeviren et al. have developed ultrathin and soft piezoelectric devices capable of in vivo evaluation of viscoelastic properties of soft tissues.

These devices were produced from flexible networks of PZT nanoribbons as mechanical sensors and actuators. It was demonstrated that these devices conformed to the underlying complex surface textures of skin and several organs under both static and dynamic conditions [25]. PZT was also used to produce a slide sensor for prosthetic hands. This works as a simple vibration sensor that produces a load proportional to the level of vibration on the surface of the fingertip. When an object is grasped by the prosthetic hand, any movement of the object that indicates the beginning of the slide will produce a vibration that can be quickly detected by the sensor and easily converted to a measurable voltage by using an amplifying charge [37]. Mechanical force-based stimulus is a convenient strategy also to control temporal and spatial drug delivery. An example of strain-triggered drug delivery device based on elastomer matrix microgel depots containing drug-loaded nanoparticles is shown by Di et al. [38]. The application of a tensile strain to the elastomer promotes drug release from the microdepot due to the increased surface area for diffusion and Poisson's ratio-induced compression on the microdepot. As a result, both prolonged drug release from normal body movements and pulsatile drug release from deliberate administration are possible [38].

The design of low-power consumption pressure sensors is always a fascinating but demanding issue. Creating self-powered sensing devices is a significant step toward attaining sustainability in pressure sensors. Self-powered pressure sensors, which can function continuously without the need for an external power supply, could be created by combining the energy generating and sensing processes into one device [29] [39], reason why smart composite material based on the piezoelectric effect are really interesting for these applications.

In addition to sensors that respond to physical signals, sensors responding to physiological signals at molecular level have been designed. Human sweat contains a high amount of valuable physiological and metabolic information. For example, the concentration of electrolytes in sweat and the pH value are important indicators for detecting electrolyte loss and dehydration during exercise. Accordingly, a variety of sensors have been explored for real-time monitoring of physiological signals (e.g., pH, glucose, Na^+, K^+, and Ca^{2+}) in sweat; in principle, an integrated electrochemical textile was used as a portable platform and CNT fiber was used as the conductive skeleton to load different types of active materials to respond to each physiological signal. For example, the pH-sensitive fiber was manufactured by polyaniline electrodeposition on the surface of the CNT fiber. In this case, the hybrid CNT/polyaniline fiber served as the working base electrode, while an Ag/AgCl fiber was used as the reference electrode. At different pH values, the polyaniline surface changes its degree of protonation

leading to different zeta potentials of the fiber hybrid. Instead, glucose-sensitive fiber, was manufactured by a coated permeable film of chitosan containing glucose oxidase as the active layer [26].

1.2.2. Energy harvesting

In medical healthcare, electronic devices should be small, light, and if in contact with human tissues, also biocompatible to avoid an autoimmune response. Sensors, cochlear implants, and cardiac pacemakers are some representative developments of devices for therapeutic application. However, most implantable devices are powered solely using batteries, which might need eventual surgical replacement. Harvesting ambient energies like as mechanical vibrations, heat, electromagnetic radiation, and in vivo energy can provide energy to operate a variety of electronic devices. According to the characteristics of these forms of energy, energy harvesting systems opportune for collecting various forms of energy are designed. Usually, the green energy harvesting systems are based on electromagnetic, piezoelectric, triboelectric, thermoelectric, photovoltaic, and pyroelectric transduction mechanisms [40].

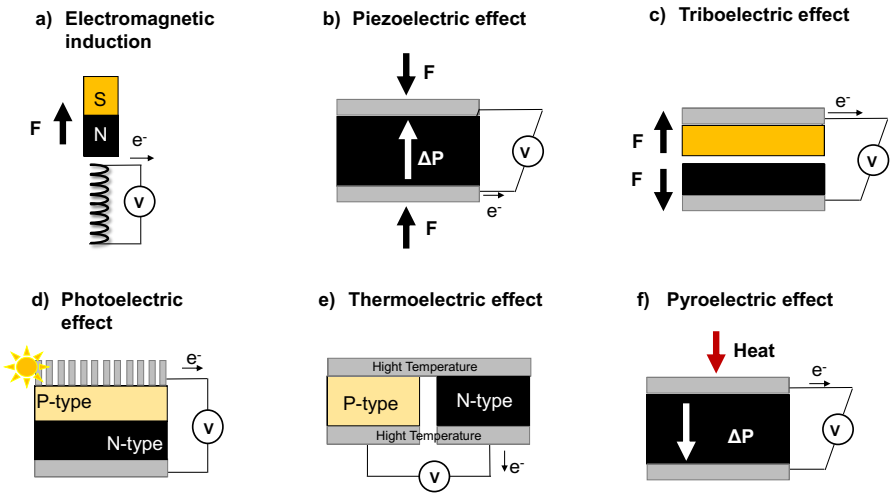

Figure 2: Schematic images of transduction methods based on: electromagnetic (a), piezoelectric(b), triboelectric(c), photovoltaic(d), thermoelectric(e) and pyroelectric(f).

Mechanical energy is the main driving force that can be used from human motion. Piezoelectric harvesters use smart materials to convert mechanical strains into electric power, whereas electrostatic, triboelectric, and electromagnetic harvesters use varying capacitance, frictional contact and electrostatic induction, and magnetic induction, respectively, to generate electric power. Among all the energy sources, mechanical energy is the energy that can be captured from human movement and converted into useful electric power and create a self-powder

system exploring triboelectric and piezoelectric generators, indicates as TENGs and PENGs respectively [41], that are the two most common ways to collect mechanical energy generated by human movements. Electromagnetic systems are not the most suitable for energy harvesting from human movements because they usually involve coils and magnets, which are means of bulky and complicated mechanisms.

In particular, TENGs is based on the triboelectrification effect that appears at the interface when two different contacted dielectrics, inducing an electrostatic charge. When the contact between two materials is terminated, the relative motion of the charged dielectrics will produce a potential difference that could flow through the external circuit. TENG operating modes can be grouped into four essential types based on the structure that are vertical contact- separation mode, contact-lateral sliding mode, single electrode mode, and freestanding triboelectric-layer mode[42], shown in Figure 3.

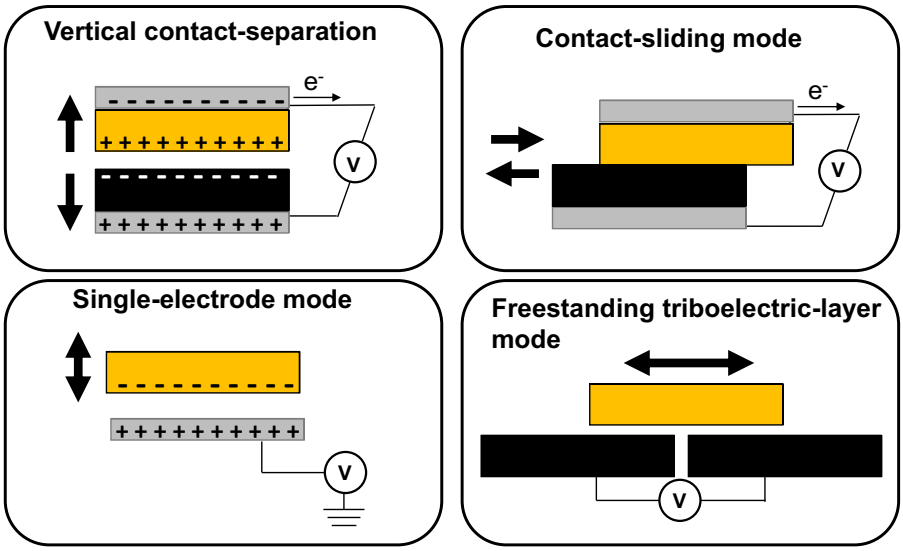

Figure 3: Triboelectric nanogenerator system operating modes.

A wide range of materials and structures has been used in TENGs fabrication in order to enhance the output performance which depends on the material and structural figure of merits. The material figure of merit is related to the surface charge density and the performance of TENG is proportional to its square. In this field the growth of technologies has been inherently associated with the development of innovative nanomaterials by creating micro/ nanostructures in the triboelectric contact area, to increase the surface charge density. The design of the structure and triboelectric materials chosen are very important to obtain TENG with excellent output performance in terms of voltage and current. Thus, by creating the porous structure of

polymeric material is possible to generate charge not only on the surface but also in the inside of the pores [43]. To further improve the outperformance, inductively coupled plasma (ICP) etching and corona discharge methods have been used to modify the surface charge [44]. For example, Zheng et al, have developed a biocompatible and implantable TENG with 'keel structure' which is modified by ICP etching on the surface and finally tested on the pericardium of a pig [45]. While Ouyang et al., have developed a TENG modified by the corona discharge method to harvest energy from heart motion. Both the systems have a significant output enhancement when subject to modification surface [44].

One important feature of TENG is the vast range of materials accessible. Any type of materials, including polymers, metals, and even paper, may be utilised to manufacture triboelectric devices because they are developed based on the fundamental mechanism of surface electrification and electrostatic induction. The general guideline for maximising performance is to choose material pairings with significant differences in electron affinity, in terms of tending to lose or gain electrons. PVDF and its copolymers, PAN (polyacrylonitrile), PVA (poly(vinyl alcohol), PDMS, PU, PLLA, PTFE (polytetrafluoroethylene), PMMA (poly(methyl methacrylate)), polyimide (PI), PA6, silk fibroin, and ethyl cellulose are just some of the polymers used to manufacture wearable TENGs. While, among inorganic materials are found gold (Au), silver (Ag) copper (Cu), aluminum (Al), silicone (Si), titanium (Ti), indium tin oxide (ITO), and titanium dioxide (TiO_2) [46]. An interesting example of TENG is given by Li et al[47]. They combine two important characteristics, nanostructure, and materials, to obtain a lightweight TEN with good output performance and that shows good mechanical durability for potential application for tiny mechanical energy harvesting and sensing. The TENG is based on carbon sponge and polymer friction layers obtained through the electrospinning process. Nylon was chosen for its tendency to lose electrons when contacted with electron attractor materials, which in this case is PET, PVDF or PI. The carbon sponge was bent into an arched structure to offer an efficient contact–separation space, while the friction layer was fixed on internal surface of arc. In this way, the obtained TENG work in contact–separation mode [47]. Other means of harvesting mechanical energy are piezoelectric generators have particularly attracted much attention. Compared with TENGs, piezoelectric energy harvesters are limited by the range of material selection because the performance depends on the piezoelectric features of the piezoelectric smart material. However, they show some advantages including a higher output current, simple structure of the device [39].

The most common transduction mechanisms for mechanical energy harvesting and sensing make use of the direct piezoelectric effect which transforms mechanical energy into electrical

energy. This effect is characterized by linearity and reversibility, and the output electric energy increases as the magnitude of polarization increases [48]. Piezoelectric-based devices typically are based on organic or inorganic material that can be in different morphology such as bulk, thin-film, fiber, and powder. Due to the intrinsic fragility of ceramic inorganic materials and to low piezoelectric coefficient typically of piezoelectric polymer, the nanostructured composite material is employed. In this way, the output performance of PNGs at low mechanical impact was improved by creating smart composite materials [10] [49].

In this context, PVDF and its copolymers with high piezoelectric deformation constants are suitable matrix materials. Nanocomposite based piezopolymer materials offer the potential to develop a new generation of flexible, high-performance energy harvesters for biomedical applications.

Nanocomposite materials containing inorganic and metallic fillers such as nanoparticles, conductive nanosheets and other materials, improves the content of the electroactive phase in the piezoelectric polymer and improves its energy collection capacity.

Improving energy harvesting capabilities could avoid the use of external energy sources for the operation of implantable biomedical devices and portable devices. Jeong et al. have developed a piezoelectric nanocomposite, that can be used for energy harvesting from hand movement, using a matrix and filler piezoelectric. Specifically, the device is based on $BaTiO_3$ nanowire obtained through hydrothermal method, incorporating into a PVDF-TRFE film [50].

Devices based on piezoelectrical PVDF have been explored due to their excellent biocompatibility and processability with microstructures [51]. An example of an energy harvesting system integrated into part of the pacemaker lead is based on porous PVDF-materials. This system did not contact the heart but could efficiently convert the energy of the heart into electrical power without interfering with the cardiovascular function [26].

Researchers have developed numerous microstructure morphology for improving flexibility in inorganic materials. Flexible PZT nanoribbons were produced by Qi et al [52] through Radio Frequency-sputtering process, while Kwon et al. [53] have used a sol-gel deposition method. Subsequently in both cases, the nanoribbons have been transferred onto polymeric substrate to create piezoribbon-based devices. Another process to produce flexible PZT is through sol-gel electrospinning. Chen et al. have deposited aligned PZT nanofibers over an interdigitated electrode on a silicon substrate, and these nanofibers produced a power [54].

Another example that allows obtaining a flexible device is proposed by Tseng et al[55]. They have produced a tactile sensor for measuring human pulses including carotid, brachial, finger,

ankle, radial artery based on PZT thin films deposited by sol-gel process on a flexible stainless-steel substrate.

In conclusion, from the materials perspective, energy harvesting is motivating the discovery of improved or new materials with novel properties for efficient and high-performance energy conversion. In general, materials and design need to be carefully selected for the particular application to maximize performance for energy harvesting. In this field, advances in material science and device fabrication techniques will continue to open opportunities for harvesting energy from vibrational human motion to direct power healthcare-focused devices. In this way, it will also be possible to extend the lifespan of implantable devices.
Many energy harvesting systems which employ mechanical energy sources in the human body are summarized in Figure 4.

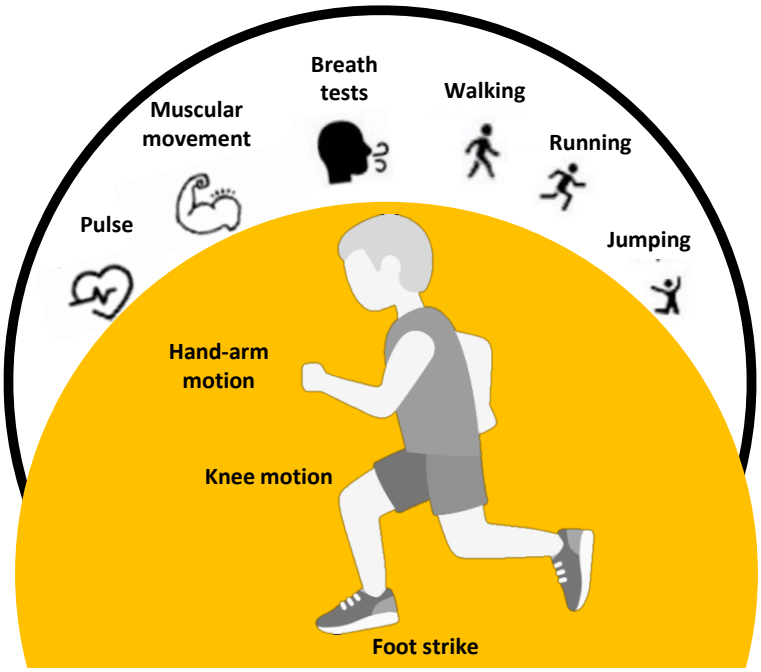

Figure 4: Possible mechanical energy sources in the human body.

1.2.3. Flexible electronics

The development of electronic technology and the improvement of medical treatment are important factors that contributed to vastly improve the quality of life and life expectancy of human beings around the world, leading to an increase in the average age of the world population.

The rapid development of flexible technology and extensible electronics has allowed their application to spread to the field of medicine for both diagnosis and treatment.

This technology can interact with internal organs and skin surface of humans reliably and without interference, and can be used to improve health monitoring, diagnosis and human-computer interfaces. Continuous, long-term, and accurate sensing in such application, are key factors, which, as seen in the previous paragraph, can be achieved via the encapsulation of an active layer (sensor) on a matrix. Such devices have proven to be capable of measuring both physical and physiological signals in different parts of the human body, either internal or external. There is a mechanical mismatch between traditional hard electronic materials which interface with soft human tissues; this mismatch often produces motion artifacts that lead to severe data acquisition errors[16][42].

Additionally, the different nature of materials that constitute electronic devices, generate another source of mismatch in both thermal and mechanical properties. As an example, we might have a device, which is made of a conductive metallic layer (i.e. gold), an active ceramic layer (i.e. piezoelectric ceramic), and a polymeric substrate (i.e. PDMS). This mismatch is proven to favor premature failure of the solid interfaces between this material due to stress localization [56]. Generally, the elastic modulus of substrate and packaging is chosen similar to the target biological tissue. Today, proper design of the device structure and active layer can solve or reduce the mismatch of mechanical properties between different materials. Innovative materials, in terms of molecular flexibility and geometric architectures, and adequate production processes can lead to the success of the device. By optimizing these keys, it is possible to obtain flexible electronic devices, capable of interfacing with parts of the human body such as internal organs or skin, to detect human health information with high accuracy and sensitivity in a reliable way and without interference [57].

The main issue consists in producing a biocompatible material that resists high values of shear and tensile stress but that prevents excessive strain to prevent crack formation and delamination of the more fragile thin functional electronic layers.

Biocompatible synthetic semiflexible polymer fibers obtained through the electrospinning process allows creating electrospun mats with desired mechanical properties, dimensions and orientations of the network architecture. This technique possesses several advantages such as the possibility to change mechanical proprieties of fibres by varying processing parameters [58].

The mechanical properties of electrospun fibers depend on the morphology, diameter, and uniformity of the fibers, processing parameters of electrospinning, and postprocessing treatments [59].

Electrospun nanofibers and mats exhibit inimitable functional properties due to of their nanoscale size, high surface area to volume ratio, and high molecular orientation. The nanofibers can be incorporated into polymer matrix as reinforcing materials to create composites materials with improved mechanical properties [60].

The fibres with a crimped morphology are capable of absorbing more strain than their straight counterparts and consequently they can reduce mechanical loads generated [61]. They can be produced by exploiting the electrospinning process in different ways such as (i) modifying the fibre orientation using a moving collector, (ii) modifying the fiber composition using for example a bicomponent fiber, (iii) subjecting them a post-processing treatment.

For example, Lin et al. produced self-crimping nanofiber using side-by-side bicomponent electrospinning of elastomeric polymer, polyurethane, and a thermoplastic, polyacrylonitrile. The stretching of both polymer components leads to differential shrinkage within the fibres due to their different elasticity [62].

Helical fibers were fabricated utilizing the difference of polymer conductivity, as demonstrated by Royal et.al. First, conductive poly(aniline sulfonic acid) and nonconductive poly(ethylene oxide) were dissolved and electrospun. Due to the partial charge neutralization of charged fibers, followed by the viscoelastic contraction of the fibers, the helical fibers were generated [63]. Surrao et al. demonstrated that electrospun nanofibers could be induced to crimp when they were released from a collector at a temperature higher than the polymer's glass-transition temperature. In particular, they found that the electrospun fibers can be crimped when the operating temperatures are higher than the glass glass-transition temperature of the polymer. Moreover, the crimping effect was determined to be a result of the residual stresses in the fibers due to fiber stretching during the electrospinning process and to the different temperature between the operating temperature and the glass-transition temperature of the polymer [64]. The difference in temperature can be induced through plasticization to allow crimping at lower temperatures or by raising the operating temperature.

Among the diversity of post-processing treatments, as heating, radiation [65] or chemical treatment, also the simple interaction polymer/ plasticizer can be used to obtain crimped fibers in a controllable way as reported Liu et al reported [61]. In this case, the interaction between ethanol and PLLA generates crimping fibers because the presence of ethanol, acting as a plasticizer enlarges the temperature window of the PLLA crystallization to RT [66], help to release the residual stress of polymer chains and reduce system energy.

The mechanical proprieties of composite material could be modified (i) changing the molecular chemistry of material properties (as modification of side chains of the polymer) or/and (ii) imposing a hierarchical structure on the material [57].

A similar approach is followed to adopted by nature that has developed a large number of ingenious solutions relating the shape and microstructure of biological objects to their function combining materials with different thermal and mechanical properties to create materials with new properties.

An example is given by the biological tissue that constitutes human tendons. The junction between tendons (which are soft) and bone (which is hard) shows tuned elastic modulus capable of varying by two orders of magnitude from tendon to bone. This is due to the hierarchical structure of tendon fascicle (Figure 5a) which are generated by parallel fascicles of collagen fibrils (assemblies of parallel molecules); these can be ultimately viewed as a nanostructured composite material in which collagen fibrils are embedded in a proteoglycan-rich matrix. Due to (i) local concentration, (ii) orientation of the inorganic phase and (iii) hierarchical structure of the collagen fibers, this tissue guarantees an efficient stress transfer and avoids local failure between regions of different elastic moduli [56], [67].

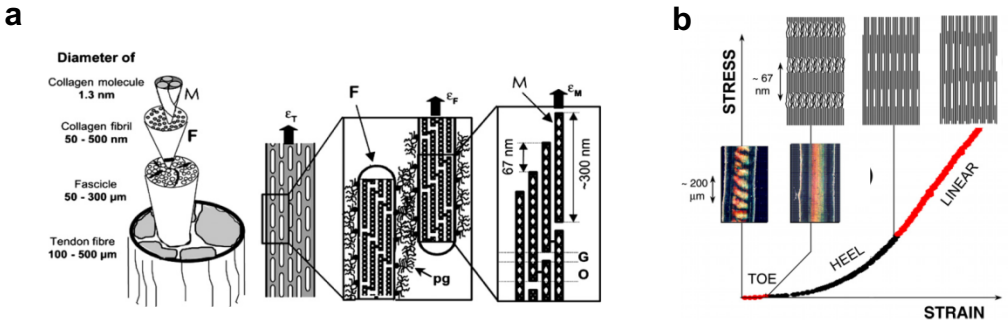

Figure 5: Simplified tendon structure (a) and stress-strain behaviour during tensile deformation (b)[67] .

In this way, nature provides a local tuning of the mechanical properties to achieve a gradual transition between stiffer and softer regions avoiding the high localized stress gradients. In particular, some of the strain will be taken up by proteoglycan matrix and the remaining strain is transmitted to the fibrils. In **Errore. L'origine riferimento non è stata trovata.** b, stress-strain curve shows that the stiffness increases in three distinct regions correlate with the deformations at different structural levels [67]. The response depends strongly on the magnitude of the deformation with the so called 'J-shaped' behaviour. For low strain, the material responds with a low elastic modulus, while at high strain the stress response is greatly increased [68], [69].

To reproduce the mechanism of biological tissue, researchers developed planar networks using different technique to create interconnects in stretchable electronics with a serpentine structure on a supporting low-modulus elastomer matrix. Changing the network geometries is possible including spatially diverse properties and isotropic and anisotropic responses to obtain desired mechanical properties [70][71][68] [72].

An interesting work, in which the inspiration from nature is exploited, is provided by Rogers et al [68]. Their work is based on an elastomeric matrix with a stretchable curved network as a structural reinforcement that can be tuned precisely to fit the non-linear properties of biological tissues.

When the tensile loads are applied to the fibers, they give a low modulus response for relatively small strains with an abrupt transition to a high modulus regime for larger strains, drawing a 'J' in the stress-strain graph. This response is tuned to a wide range of deformations and can avoid an excessive deformation that would lead to failure of the electronic device. Designed this way, this class of composite nanostructured materials is suitable from soft biomedical devices for tissue engineering. [68].

Studart et al. used a nature-inspired strategy to fabricate high-performance rugged flexible devices based on particle-reinforced composites with locally tuned mechanical properties. They demonstrated that it is possible to form stiffer regions close to the composite surface to locally protect stiff electronic devices by using magnetically responsive alumina nanoparticles (platelets) as reinforcing elements for several polymeric matrices, including thermoplastic polyurethane elastomer and cross-linked polyvinyl alcohol [73].

In the same year, they have combined inorganic reinforcing particles, at two different length scales, to produce large-area highly structured polyurethane-based composites with a wide spectrum of properties using the same polymer matrix. This has produced a hierarchical

reinforcement of polyurethane which showed tuneable elastic modulus from 200 to 7000 MPa [74].

In summary, the key challenge, when designing flexible electronic devices, is to be able to develop integrated circuits which has to be incorporated in a matrix whit specific mechanical property, to guarantee high performance and functionality while preserving the mechanical integrity of the system. As an approach, investigating new or composite materials will accelerate progress in flexible electronic focusing on devices that exploit specific physical and chemical properties associated with the targeted application. Thus, thanks to the collaboration between materials sciences, physics, clinical medicine, and engineering, it will be possible to expand the field of applications from mere diagnosis to advanced human-machine interfaces, regenerative medicine and advanced therapies. [75].

1.3. Piezoelectric materials

In 1880, Pierre and Jacques Curie discovered the phenomena of piezoelectricity while carrying out research on quartz, tourmaline, and Rochelle salt crystals. There are two types of piezoelectric effects, direct and inverse, which represent the capability of certain materials to convert mechanical energy into electrical energy and vice-versa. In particular, the direct piezoelectric effect involves the generation of electrical energy when mechanical stress is applied. While, we have an inverse piezoelectric effect, when, due to the application of an electric field, a mechanical displacement occurs in the material [10]. The piezoelectric effect can be described by the following relationships:

Direct effect: $P_i = d_{ijk}\sigma_{jk}$

Invers effect: $\varepsilon_{ij} = d_{kij}E_k$

Where, for the direct effect, P= polarization generated, σ= stress applied and d = piezoelectric constant. Whereas, for the inverse effect, ε = strain generated, E = electric field applied.

Since piezoelectric materials are anisotropic, their electrical, mechanical and electromechanical properties change according to the direction of application of the stresses (electrical/mechanical). For this reason, it is necessary to use subscripts i, j and k, which refer to the different electrical/mechanical and polarization directions in the material coordinate system. Specifically, the possibility to use the materials a sensor is due to the direct piezoelectric effect, while its ability to be used as an actuator is due to inverse piezoelectricity effect.

Regarding the sensor application, the ability of the piezoelectric material to develop an electric field as a response to applied force can be described by the piezoelectric voltage g_{ij} (Vm/N). While for actuator applications, the piezoelectric strain d_{ij} (m/V) can be used to define the ability of piezoelectric material to generate large deformations by applying low electric fields [76]. To achieve an optimal piezoelectric response from a material, it is necessary to perform a process, named "poling". During this process, the molecular dipoles in a material are orientated through the application of a high electric field at a high temperature, followed by cooling maintaining the electric field to preserve the orientation state (Figure 6).

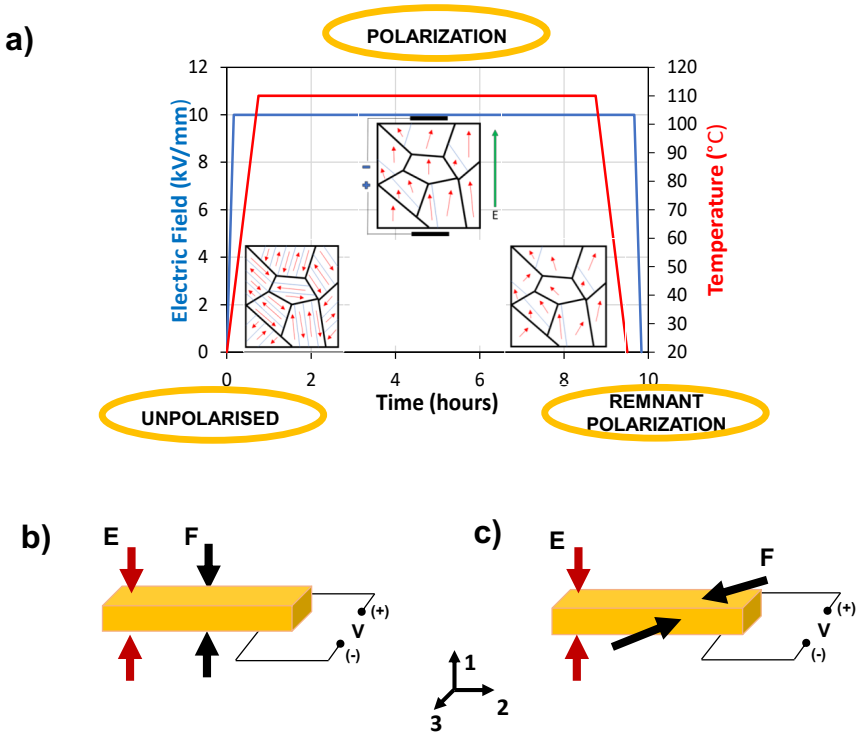

Figure 6: Example of polarization process carried out on crystalline material (a). Operation modes of a piezoelectric material after polarization process in direction 3. In 33 mode the applied force (black arrow) is in the same direction of the electric field (red arrow) on piezoelectric material (b) and 31 mode, in which applied force is perpendicular to the direction of electric field on piezoelectric material(c).

The piezoelectric effect is originated from the loss of the equilibrium state between the positive and negative electric charges in the material. Therefore, in absence of external stress, the material is neutral. In the case of inorganic materials, the piezoelectric effect is generated from the different arrangements of ions in the non-inverse symmetric crystalline structure of certain dielectric materials. While in organic materials, the piezoelectric effect is induced by the polymer's molecular structure and its orientation[77]. In both cases, the internal charge of the materials changes with the linear trend as a function of the applied stress.

The lead zirconate titanate (PZT) is the most used piezoelectric inorganic material. It can be seen in Figure 7, how Ti or Zr ions, will displace inside the PZT crystal unit cell, when an external force is applied. This phenomenon is what generates piezoelectricity in PZT crystals in the perovskite phase. Perovskite is a common structure adopted by many oxides with formula ABO_3 such as $LiNbO_3$, $LiTaO_3$, $BaTiO_3$, $CaTiO_3$ etc.

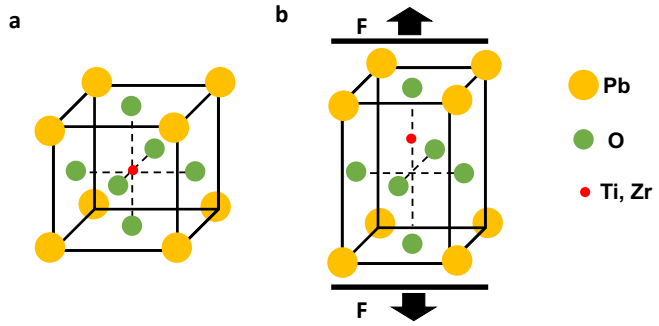

Figure 7: Perovskite structure adopted by PZT before (a) and after (b) applied stress.

Compared with other piezoelectric materials, PZT exhibits greater sensitivity, stability at high temperatures, is chemically inert, and is relatively low cost to manufacture [78]. PZT is a crystalline ceramic with a non-centrosymmetric structure that possesses superior piezoelectric proprieties, compared to other piezoelectric materials like aluminium nitride, zinc oxide,

barium titanate, especially when x = 0.50 to 0.52 i.e. in the region near the morphotropic phase boundary (MPB) as show in Figure 8 [79].

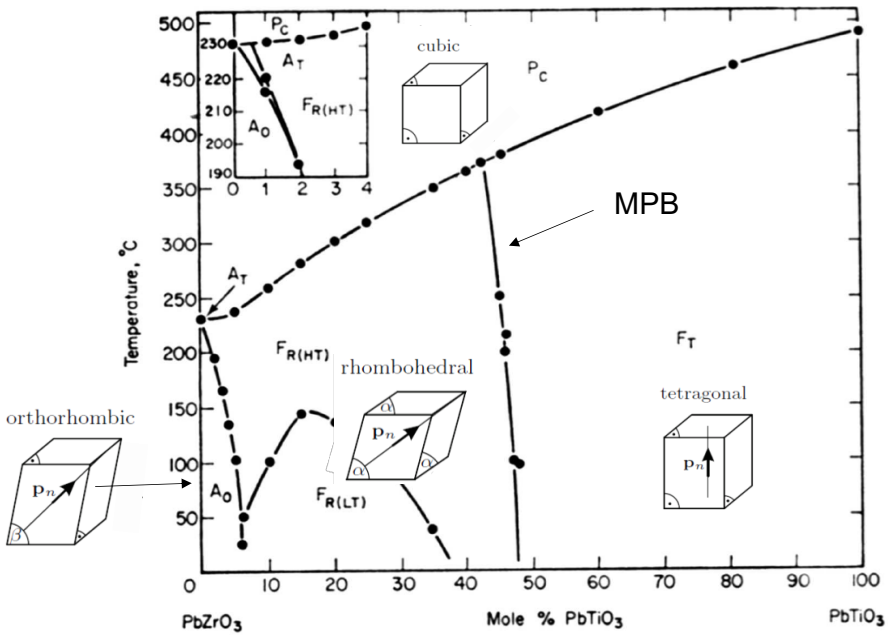

Figure 8:The phase diagram of $PbTiO_3$-$PbZrO_3$ solid solution, according to (B. Jaffe, W.R. Cook, and H. Jaffe, Piezoelectric Ceramics (Academic Press, London, 1971).

This site, that separates the tetragonal symmetry (Ti-rich) from the rhombohedral symmetry (Zr-rich), is of particular interest because allows a large number of possible polarization directions which lead to a peaking of permittivity and piezoelectric coefficient [80].

In the boundary phase, 6 domain states of the tetragonal phase and the 8 possible domain states of the rhombohedral phase are both energetically advantageous, allowing a total of 14 possible domain states. The increased number of available domain states leads a better piezoelectric response [81] [82].

For this reason, PZT has always attracted the attention of the researchers for many applications, where the excellent electromechanical proprieties are required, as a sensor, actuator, energy harvesting and structural health monitoring [83]. Unfortunately, two main problems must be overcome to use PZT in medical devices: the presence of lead and the stiffness and brittleness typical of ceramic as bulk materials. To solve these problems, it is possible to use nanostructured composite materials. Inorganic materials in the form of nanofibers, nanowires, ultra-thin films can exhibit good mechanical properties such as flexibility and their incorporation into a biocompatible matrix allows overcoming the toxicity of lead. Several chemical and physical methods can be used to prepared PZT materials, such as sol-gel process,

Metallo-organic decomposition (MOD), radio frequency sputtering (RFS), and pulse laser deposition (PLD). Among them, the sol-gel process is an optimal way to have a high control on the composition of the system in terms of concentration and stoichiometric ratio [84] trough hydrolysis and condensation reactions of metal alkoxides in an alcoholic media.

The sol-gel process offers the possibility to prepare materials in different configurations as thin films, foams, powder or nanofiber using various processing technologies [82][78]. In recent years, numerous works are focused on PZT nanofibers as, thanks to the fibrous morphology, they offer the possibility of composite device fabrication where flexibility and reinforcement are required.

Other inorganic materials that have good biocompatibility characteristics and good piezoelectric properties are zinc oxide (ZnO), aluminum nitride (AlN), Gallium nitride (GaN) etc [79].

Polymers themselves can exhibit their own piezoelectric behaviour, although they are usually characterized by lower strain coefficients (d_{33}) and voltage coefficients (g_{33}) than inorganic materials. However, their excellent features, including flexibility, low density, biocompatibility, and processability, make them suitable for a wide range of medical applications.

In the case of organic materials, like piezo-polymers, the piezoelectric effect is generated from the oriented molecular dipoles within the molecular structure of polymer chains, accordingly. This is possible by poling process at temperate above the polymer's glass transition or by stretching the macromolecules. Among the piezoelectric organic materials are found poly(L-lactic acid) (PLLA), polyvinylidene fluoride (PVDF), poly(vinylidene fluoride-trifluoroethylene) P(VDF-TrFE), nylon etc. Figure 9 shows the repetitive units of some piezoelectric polymers in order to highlight the presence of polar bonds.

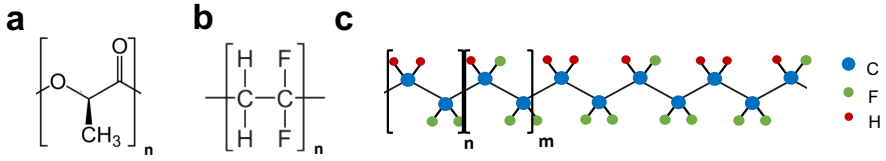

Figure 9: Repeat unit of the chemical structure of PLLA (a) and PVDF (b). Schematic representation of the chain conformation for β-phase of PVDF-TRFE (c).

In particular, the PLLA displays a piezoelectric behaviour when the molecular structure of chains possesses all C=O dipoles in the same direction. This orientation occurs during the electrospinning process [85].

Fluorinated polymers are attractive macromolecules because of their versatility due to their relevant properties mainly linked to the low polarizability and the strong electronegativity of the fluorine atom, to its small van der Waals radius (1.32 Å), and to the strong C-F bond (485 $kJ \cdot mol^{-1}$) [86].
Thanks to this C-F strong bond, fluorinated polymers exhibit high thermal, chemical, aging, and weather resistance, excellent chemical inertness and low dielectric constants. For these reasons, fluorinated polymers have found major developments in modern technologies as microelectronics.
Among fluorinated polymers, polyvinylidene fluoride (PVDF) exhibits physical and electrical interesting properties which main depends upon the chain configurations, crystalline form and defects of chaining [87]. The most important proprieties that PVDF show is the piezoelectric behaviour due to the strong C-F bonds and the spontaneous orientation of dipoles in the crystalline phases. PVDF is a semi crystalline polymer, with 50-70% crystalline phase and show five polymorphs (α, β, γ, δ end ε) possible thank to the slightly larger van der Waals radius of the fluorine atom (1.35 Å) versus that of the hydrogen one (1.20 Å). Among different crystalline phases, the α-phase is the most common, kinetically favourited and characterized by trans-gauche conformation in which the polymeric chain is in nonpolar configuration (TGTG'). While, the β-phase is the most thermodynamically stable form whit piezo-piro and ferroelectric feature due to the zigzag (all-trans) conformation (TTT) of the polymeric chains whit a strong orientation of the dipole in the $-CH_2CF_2-$ [88][89]. Thus, when all C-F dipoles are all parallel (β phase), a high dipole moment is provided and the best piezoelectric response is displayed [90] [91]. In order to obtain the β phase in PVDF polymer, in literature several methods have been explored including stretching of macromolecules (mechanically or through electrospinning), annealing process, poling process and use of copolymers [92] [93].

The use of copolymers is the most efficient way to modify polymer structure as a function of required proprieties, acting on the symmetry of the polymeric chain and modulating both intramolecular and intermolecular forces and so that properties such as thermal (melting point, glass transition temperature) and dielectric (dielectric constant) are correlated [94].

A wide variety of advanced materials can be prepared from copolymers such as PVDF-TrFE, Poly(vinylidene fluoride-co-hexafluoropropylene) (PVDF-HFP) and poly(vinylidene fluoride-co-chlorotrifluoroethylene) (PVDF-CTFE). The grafting of different monomers provides the possibility to tune electrical, mechanical and thermal proprieties. the incorporation of TrFE into PVDF induces the occurrence of a ferroelectric-to-paraelectric (F-P) phase transition (called Curie transition) associate with a crystalline phase change from polar (β) phase to nonpolar (α) phase at below of melting point [95] This gives piezo, pyro-electric proprieties thank to the β phase which shows an all TTTT conformation wherein the polar C-F and C-H bonds possess a dipole moment perpendicular to the carbon backbone, which makes it the most electrically active phase [91]. In PVDF-TrFE copolymer, the crystalline structural change with increasing TrFE content leads a lowering of the Curie temperature (T_c) that increase with amount of TrFE content in the PVDF chain [96]. Indeed, inserting CF_3 groups within the main chain, produce a higher free space between chains thus allowing higher mobility; this increases the piezoelectric propriety when compared with the homopolymer [97]. In recent years, various techniques have been used to control and enhance the formation of the β-phase in PVDF-based polymers, including the electrospinning process. Indeed, during this process, both electrical and mechanical effects allow collection of fibers rich in β-phase content. Indeed, the strong electrostatic uniaxial stretching introduces elongational forces in the direction of the jet, creating molecular orientation which leads to the transition from α-phase to β-phase [88].

2. Materials and Methods

Electrospinning technique and apparatus

The main technique employed in this research to fabricate composite materials is based on the electrospinning process. The top-down manufacturing technique of electrospinning enables to produce polymeric, ceramic and carbonaceous continues fibers with diameters from tens to hundreds of nanometres exploiting electrohydrodynamic (EHD) principle and its does have scalability for mass production [41]. The electrospinning set up is very simply and consists of four components: a high voltage supply, a syringe with a conductive needle, a syringe pump, and a grounded collector (Figure 10).

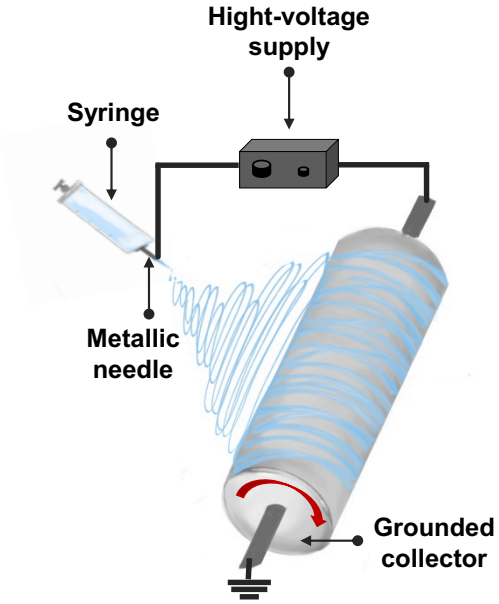

Figure 10: Electrospinning set up.

The solution during the electrospinning process is charged and exposed to electrostatic repulsion between surface charges and Columbic force by an electric potential. When the electrical force exceeds the surface tension, the drop changes its shape generating the so-called Taylor's cone from which a fluid jet is created. During the process, the presence of entanglements, in the case of the polymer jet or interaction between molecules in the sol-gel solution, allows the formation of continuous jet, which is elongated in the grounded collector direction. The solvent evaporates from the jet leaving a dry fibre. The technique can be adaptable by modifying a number of parameters, such as solution parameters (polymer molecular weight, concentration, viscosity, conductivity, surface tension), process parameters (applied voltage, flow rate, distance between needle and collector) and environmental parameters (humidity, temperature) [41]. The above-mentioned variables play a significant role

on the final morphology and microstructure of non-woven mat. For instance, the electrical potential difference (ΔV), has an effect on the diameter of the fibers, which in turn influences pore size[98]. Generally, the increase in ΔV decreases fiber diameter [99]. By reducing the fiber diameter, the specific surface area (defined as the ratio of the area of a solid and its volume) grows proportionally influencing several properties as chemical reactivity, the capacity of absorb or release molecules, the bonding with a surrounding matrix etc..[100]. In case of the composite materials, the enormous interfacial area between nanofiber and polymer matric promotes efficient load transfer from polymer matrix to nanofiber fillers, acting as reinforcement. Moreover, the architectures of non-woven mat can be modulated in special configuration employing special collector, such as rotational cylinder collector or using an auxiliary electrode to collect aligned nanofibers with a variety of angles.

To produce non-wowen mat used in these projects of research to fabricate composite materials, the following electrospinning apparatus was employed.
The electrospinning (ES) apparatus, made in house, was composed of a SL 50 P 10/CE/230 high voltage power supplier (Spellman, New York, USA), a KDS-200 syringe pump (KDScientific Inc., Massachusetts, USA,), a plastic syringe containing the polymer solution, a stainless-steel blunt-ended needle (Hamilton, Bonaduz, Switzerland) connected with the power supply electrode and a grounded cylindrical aluminium collector. The polymer solution was dispensed through a Teflon tube to the needle that was orthogonally placed on the rotating cylindrical collector (which was tightly wrapped with paper to facilitate fibre mat collection). The ES apparatus was placed in a glove box (Iteco Eng., Ravenna, Italy, 100 x 75 x 100 cm) equipped with a temperature and humidity control system.

2.1. PZT nanofibers preparation

Materials

The reagents used in this Thesis to produce the PZT precursors' solution were:
lead (II) acetate trihydrate ($Pb(CH_3COO)_2 \cdot 3\ H_2O$); zirconium (IV) n-propoxide ($Zr(OCH_2CH_2CH_3)_4$ 70 wt.% solution in 1-propanol); titanium (IV) isopropoxide ($Ti[OCH(CH_3)_2]_4$ 97%); All reagents were purchased from Sigma Aldrich.
The solvents used in this Thesis were: 2-methoxyethanol (2-MOE anhydrous, 99,8%); dimethylformamide (DMF) ≥ 99,8%; acetone ≥ 99,5%; dichloromethane (DCM) ≥ 99,9%;

absolute ethanol (EtOH) 99.8%; isopropanol (IPA) ≥ 99,5%; Cyclohexane anhydrous 99.5% were purchased from Sigma Aldrich.
Glacial acetic acid (AcOH) was acquired from Carlo Erba.
The polymers used in this Thesis were: polyvinyl acetate (PVAc, MW= 500.000 Da); polyvinylpyrrolidone (PVP, MW= 360.000 Da) were purchased from Sigma Aldrich.

PZT Synthesis

Several modifications in sol-gel processes have been made since 1986 until today focussed on the development of PZT solutions that satisfy processing requirements such as, high concentration metal precursors, chemical stability under environment conditions and thermal decomposition with low evaporation [101]. The most common way to obtain a stable PZT precursor solution is to stabilize alkoxides made of zirconium n-propoxide and titanium iso-propoxide with add a salt of Lead in molar ration of 1.1: 0.52: 0.48. Acid acetic is used as a chemical modifier and chelating agent because promotes a ligand change between the alcohol groups of the alkoxide and its acetate groups reducing the moisture sensibility of the alkoxides slowing the condensation reactions [102].
Through this procedure is possible to ensure a homogeneous mixing at the molecular level of all metal cations reducing the diffusion path range during the thermal process that leads to PZT crystallization. Indeed, in order to have the conversion from amorphous gel to solid crystalline oxide is necessary that the gel is subjected to a drying process and subsequently, a heat treatment during which the loss of organic components and lead transformation, from acetate to oxide, occurs. Another benefit of the sol-gel process comes from the possibility of employing the stable solution to prepare nanofiber using sol-gel electrospinning technologies to fabricate flexible devices.
PZT nanofibers have already been successfully obtained through sol-gel electrospinning using polyvinylpyrrolidone or polyvinyl acetate as a carrier polymer to adjust the viscosity PZT precursor solution [103][104][105][106]. Many researchers have studied the influence of the polymer carrier content and the effect of the ageing time on the viscosity of the PZT sol-gel solution [104] and therefore on the morphology of the PZT fibers. Other Authors have focused their attention on the study on the mechanism of the formation of the PZT perovskite phase from the pyrochlore phase. Usually, in order to identify the metastable intermediate phase, the PZT nanofibers are analysed by XRD, both as spun and after thermal treatment from 400°C to 700°C. The formation of the pyrochlore phase is identified around at 400°C, which begins to

convert into perovskite at 550°C and subsequently in pure perovskite phase at 700°C [102]. Wang et al. studied the formation mechanism of the perovskite phase of the PZT nanofiber, with and without pyrolysis procedure before calcination process. They found that the pyrolysis procedure has the good effect on perovskite phase formation, and this is attributed to the control on pyrochlore phase nanocrystals formation and sufficient removal of residual organics[107][106].
Although the transformation from pyrochlora phase to perovskite has been extensively studied by varying time and temperature, the same has not been done by varying the concentration of lead in the PZT precursor solution.

Therefore, in this PhD (i) PZT nanofibers have been produced by modifying sol-gel synthesis based on chelating acetic acid as reported below. (ii) To identify the ideal carrier polymer in the sol-gel electrospinning process which ensures the maintenance of the PZT fibrillar morphology, two polymer carrier with different thermal proprieties were selected and tested. (iii) To preserve the ratio of PZT crystalline nanofiber, several PZT precursor solution whit different concentration of lead were synthetized studying structural evolution and crystallization kinetics. Moreover, the effect of the morphologies, powder and nanofiber, on lead oxide volatility has been highlighted during the heat treatment.

Synthesis of PZT precursor solution

The entire synthetic process reported below was carried out under a fume hood and was followed to produce a 50 ml of PTZ precursors' solution. Figure 11 a and b show the apparatus and general flow chart using to synthetize the stable PZT precursor solutions. In the procedure, metal alkoxides $Zr(OCH_2CH_2CH_3)_4$ and $Ti[OCH(CH_3)_2]_4$ were mixed and dissolved in acetic acid (7 ml). Meanwhile, $Pb(CH_3COO)_2 \bullet 3\ H_2O$ was dissolve in acetic acid (14 mL) and to expel the hydration water from the system, the solution was stirred at a temperature of 100°C for 30 minutes. Thus, the lead system was left to cool to room temperature (RT). Prior to form a homogeneous solution made of lead and metal alkoxide, 2-methoxyethanol (15 mL) was added. The whole system was heated at 80°C and left stirring for 1 hour. Afterwards, another portion of methoxyethanol (14 mL) was added and the solution was left stirring under reflux all night at 80°C. The next morning the solution was left to cool to room temperature and then vacuum-filtered.

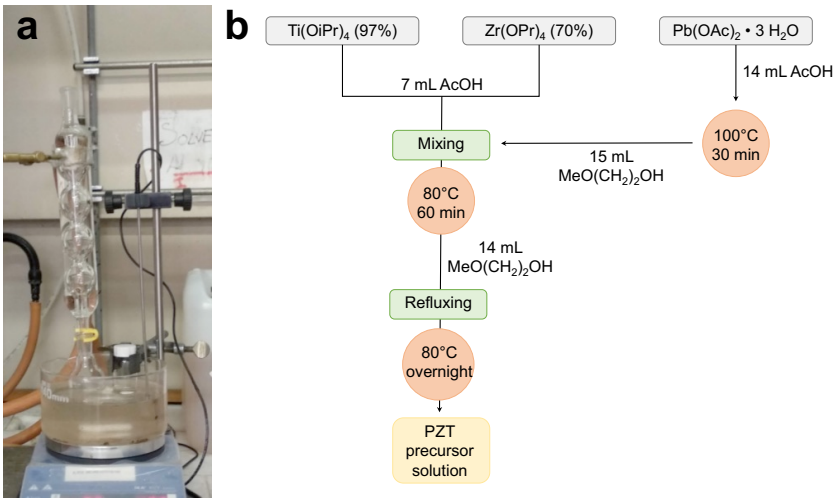

Figure 11: Apparatus (a) and flow chart of the synthesis of PZT precursor solution (b).

The specific composition of prepared PZT precursor solution were report in the Table 1:

Table 1: Composition of prepared PZT precursor solutions.

Solution	$Pb(OAc)_2 \cdot 3\ H_2O$ (mol)	$Zr(OPr)_4$ 70%w/w (mol)	$Ti(OiPr)_4$ 98% w/w (mol)
PZT(108/52/48)	0.0324	0.0156	0.0144
PZT (116/52/48)	0.0351	0.0156	0.0144
PZT (124/52/48)	0.0372	0.0156	0.0144

PZT nanofiber by sol-gel electrospinning

The optimal way to synthesise ceramic nanofibers is through sol-gel electrospinning technique. In the case of PZT nanofibers, in particular, the process starts from the precursor's solution that must be enough stable to be subjected to the electrospinning process, i.e. the process of gelification must be avoided before electrospinning.

To achieve the right viscosity with the precursors' solution, the latter was mixed with a carrier polymer, and the carrier polymer-PZT precursor's solution was electrospun.

To prepare the polymer carrier/PZT solution, two different polymer carrier PVAc and PVP were investigate. In a both cases, polymer carriers were dissolved in the precursors' solution of PZT (prepared as described 2.2) at a concentration of 10% w/v. A representative solution was prepared with 500 mg of polymer carrier was dissolved in 5 mL of PZT solution. The solution was stirred at room temperature for around 24 hours and then electrospun by the electrospinning (ES) apparatus, described in paragraph *Electrospinning technique and apparatus*.

The electrospun conditions were reported in the Table 2.

Table 2: Optimized electrospinning conditions of polymer carrier/synthesized PZT solution.

Polymer	Applied voltage (kV)	Flow rate (µl/min)	Working distance (cm)	Collector speed (rpm)
PVAc	16	8	16	70
PVP	10	16	10	70

PZT powder

To produce PZT powder, precursor solutions were poured in a glass petri dish and kept at RT for 72h under a fume hood to allow the PZT powder precursor formation. Then, in order to obtain ceramic PZT powders, the precursor's gels were scratch from petri, grinded into a fine powder using a mortar and pestle.

Thermal treatment and Calcination

The obtained pristine PVAc/PZT nanofibers and powder were subjected to a sequence of heat treatments involved heating ramp of 10°C/min:

i) stored for 12 h at 115 °C in air;

ii) stored for 12 h at 210 °C in air;

Subsequently, electrospun mats were calcined in air at 700°C for different time specifically after 5, 10, 15, 20, 30 and 60 minutes and quenched. While PZT powders were calcined in air at 700°C for 1h and then quenched.

The obtained pristine PVP/PZT nanofibers and powder were subjected to a sequence of heat treatments involved heating ramp of 10°C/min:

i) stored for 12 h at 250 °C in air;

Subsequently, electrospun mats were calcined in air at 700°C for 1h and then quenched.

2.2. PVDF-TrFE nanofibers preparation

Materials

The material used in this Thesis to produce the piezoelectric nanofibrous mat was copolymer polyvinylidene fluoride-trifluoroethylene (PVdF-TrFE, 80/20 mol%, Mw= 600 kDa) was provided by Solvay S.p.A. Milan, Italy.

The solvents used in this Thesis were dimethylformamide (DMF) ≥ 99,8% and acetone ≥ 99,5% purchased from Sigma Aldrich.

PVdF-TrFE nanofibers

The piezoelectric nanofibrous mat was produced via electrospinning starting from a polymeric solution, prepared by dissolving 7 wt % of copolymer PVdF-TrFE in DMF: acetone (23:70 wt %) The electrospinning process was carried out using the electrospinning (ES) apparatus, (described in paragraph *Electrospinning technique and apparatus)* by applying 15 kV at the high voltage needle and collecting the nanofibers randomly on a grounded rotating drum at 0.2 m/s tangential speed placed at 15 cm. The process was carried out for 2 hours at 0.8 ml/h as flow rate.

After production, the nanofibrous layer was poled at 130°C for 5 minutes in a bath of vegetal oil by applying 25 kV/mm. The electric field was then kept on until the oil cooled down to room temperature. The vegetal oil for the polarization process was used to fill the porous structure of the membrane during the process and increase the electric field value on the nanofibers by avoiding electrical discharges (electrical breakdown equal to 70 kV/mm). Then, the nanofibrous layer has been soaked in a cyclohexane bath for 1 hour in order to completely remove the oil.

2.3. Curled PLLA preparation

Materials

The polymer used in this Thesis to produce electrospun mat was poly L-lactic acid (PLLA, Lacea H.100-E, Mw = 8.4 x 10^{-4} g/mol, PDI = 1.7) was acquired by Mitsui Chemicals.

The solvents used in this Thesis were dimethylformamide (DMF) ≥ 99,8%; dichloromethane (DCM) ≥ 99,9%, Absolute Ethanol (EtOH) (99.8%) purchased from Sigma Aldrich.

PLLA curled nanofibers

The manufacturing process of the curled nanofibers is shown in the Figure 12.

To produce the PLLA nanofiber, the electrospinning apparatus, homemade was use described in paragraph *Electrospinning technique and apparatus. P*LLA pellets were dissolved in a mixed solvent, DCM: DMF = 70:30 v/v at a concentration of 15% w/v and electrospun using the following conditions: applied voltage = 17 kV, needle to collector distance = 20 cm, collector rotational speed= 6000 rpm, solution flow rate = 23 µl/min, at room temperature (RT) and relative humidity RH = 40– 50%. To generate curled nanofibers were exploited the interaction between the polymer and plasticizer. PLLA nanofibrous was cut in strips of the same dimension with fibers aligned along the long axis of the strips. Before soaking in the EtOH each

strip was fixed onto a made-home device with an initial length of 2 cm (L_i). In order to generate nanofiber with a controllable degree of crimping, the polymeric shrinkage was exploited blocking the mat a different distance (L_f) to obtain different shrinkage values of the polymer chain during the EtOH treatment. In particular, the strip was fixed at the device and were immersed in EtOH bath at RT for 20 minutes, (i) to allow the maximum relaxation of the polymer chain i.e. 30% shrinkage, (ii) to avoid relaxation of the polymer chain, i.e. 0 % shrinkage and (iii) to allow a 50 % relaxation of the polymer chain, i.e. 15% shrinkage. These samples were labelled as "free", "bounded" and "50% bounded".

The degree of shrinkage was determined using the following equation and was used to determine the degree of shrinkage using the following equation:

$$\%\, Shrinkage = \frac{Li - Lo}{Li} \cdot 100 \qquad (1)$$

Finally, the strips were placed on a Plexiglass panel and cut with a punch of 0.5 cm^2 of width using a pressure press.

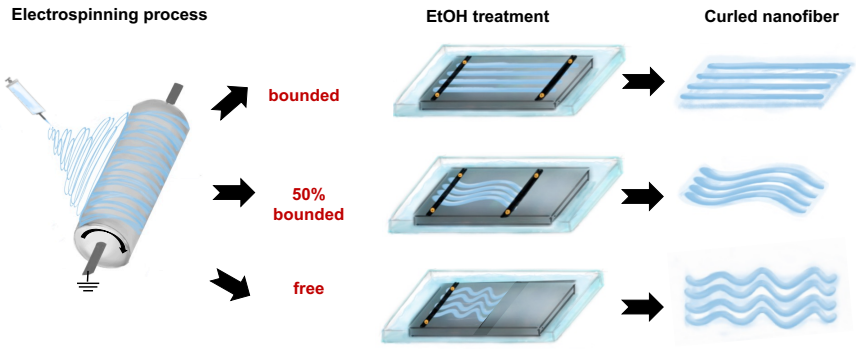

Figure 12: Schematic illustration of the procedure for the fabrication of nanofibers with controllable curvature. The aligned nanofibers network was produced by electrospinning process, then the mats were blocked by a custom device at three different length values to define the shrinking possibility during the soak in EtOH bath. Finally, the curled PLLA nanofibers were obtained.

2.4. PZT powder in GFRP composites

Materials

In order to create functional composite materials based on PZT powder interleaved in glass fiber reinforced plastic prepreg and interspersed with metal electrodes to collect the piezoelectric signal were fabricated. The materials used were:

- Glass Fiber Reinforced Polymer prepreg (GFRP, E-glass 8H Satin 300 g/m^2 - epoxy matrix, VV300S - DT121H-34) was acquired from DeltaPreg;
- Commercial sensor 7BB-35-3L0 made with Piezotite® P-7B piezoelectric material was acquired from Murata;
- Brass foil of thickness 0.1 mm;

PZT powder-based composites

The composite materials were fabricated using PZT powder obtained from the commercial sensor as illustrated in Figure 13. The piezoelectric element was embedded in the composite in two different forms: the commercial sensor (BULK) as provided by the manufacturer and the PZT powder (PWD) obtained by grinding the PZT disk which was extracted from the commercial sensor.

In laminate, the BULK piezoelectric sensor was embedded in the laminate as such and its electrodes (lower brass sheet and upper silver coating) and cables were used to collect the signal. In PWD laminate, the PZT disk was extracted from the pristine sensor by means of a thermal treatment of 1 hour at 350 °C In this way, it was possible to easily detach the PZT disk from the commercial electrodes - by burning the glue - and remove the industrial polarization by exceeding its Curie temperature (T_c) of 300 °C. Then, the PZT powder was obtained by grinding the disk for 20 seconds with an electrical mill (IKA A 10 basic).

The powder was then distributed and interleaved between composite plies. Moreover, in PWD laminate two brass sheets were interleaved in the composite and used as electrodes to collect the piezoelectric signal. Subsequently, the sensing laminates are composed of woven layers of GFRP prepreg (50 × 50 × 0.245 mm) interleaved in the midplane with the piezoelectric element types, powder and bulk. PWD laminate is interspersed with thin circular sheets of brass (⌀ 20 × 0.1 mm for the upper electrode and ⌀ 30 × 0.1 mm for the bottom one) to collect the piezoelectric signal; while BULK laminate does not have the brass electrodes because the ones of the commercial sensor were adopted. Before stacking, the brass sheets were grinded with sandpaper to improve the adhesion with the epoxy resin of the prepreg layers. Then, signal cables, coated with a Teflon jacket to withstand the high temperatures of the composite curing cycle, were soldered on the brass sheets.

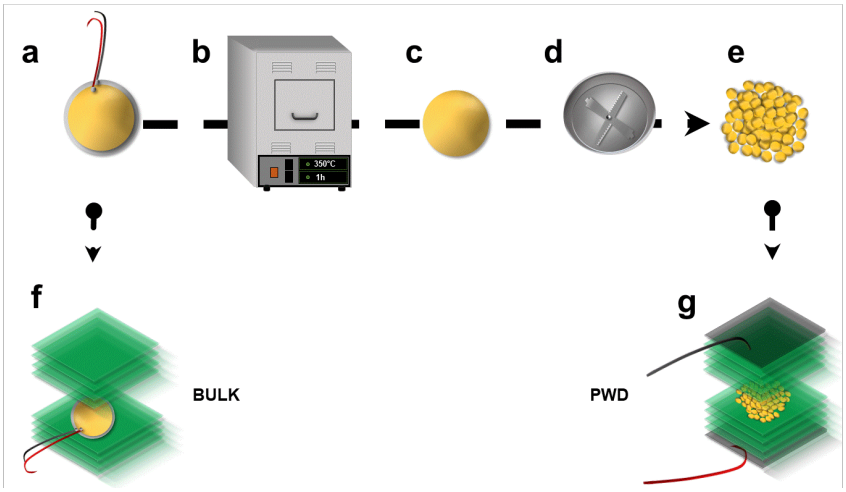

Figure 13: Scheme of manufacturing of the piezoelectric composite laminates. The commercial sensor (a) was treated thermally to remove the industrial polarization and (b) and to remove the electrodes. The obtained PZT disk (c) was ground (d) to obtain PZT powder (e); Pristine sensor (BULK) (f) and powder PZT (PWD) laminate (g) were embedded in the midplane of the laminate.

After stacking, all laminates were cured in autoclave with vacuum bag technique, following the custom 3-steps curing cycle to facilitate the impregnation of the PZT powder, evacuating air bubbles and increasing the glass transition temperature (T_g) of the epoxy resin. In particular the three steps curing involved with application of pressure of 6 bar and with 2 °C/min heating and cooling ramps, using a custom 3 steps cure cycles, as follow reported:

- Stored a 30 min isotherm at 50 °C;
- Stored a 20 min isotherm at100 °C;
- Stored a 60 min isotherm at 150 °C.

In particular, the first step decreases the viscosity of the epoxy resin without significantly triggering the cross-linking. The second step starts in gradual mode the cross-linking of the epoxy matrix. The third step (iii) completes the cross-linking of the epoxy resin and brings the glass transition temperature (T_g) [108].

To investigate the effect of the PZT morphology and the PZT/GFRP volume ratios on the piezoelectric and mechanical properties of the hosting composite laminate, specimens with different stacking sequence configurations, maintaining constant the total number of GFRP equal to 8 plies, were fabricated as summarized in Figure 14. For each laminate, only one sample was produced, due to the manufacturing and testing complexity.

As a reference for the mechanical behaviour, a pristine non-sensing laminate with 10 GFRP plies, named REF-G10, was manufactured (Figure 14a). A BULK conventional sensing

laminate with 8 GFRP plies and the commercial sensor interleaved as such in the midplane was fabricated (Figure 14b). While an experimental design matrix 3x3 on PWD laminate was performed (Figure 14c). In particular, the combination of three different PZT powder areal densities (600, 1200 and 2400 g/m^2) interleaved in the midplane with three different number of GFRP plies (2, 4 and 8) within the electrodes was investigated and relative configurations were reported in Table 3. Then, to achieve piezoelectric behaviour, the PZT embedded in the laminates were polled by applying a DC electric field of 4 kV/mm across the two electrodes at 100 °C for 24 hours. In the end, the system was cooled down to room temperature at 2°C/min, maintaining the electric field applied to stabilize the dipoles alignment.

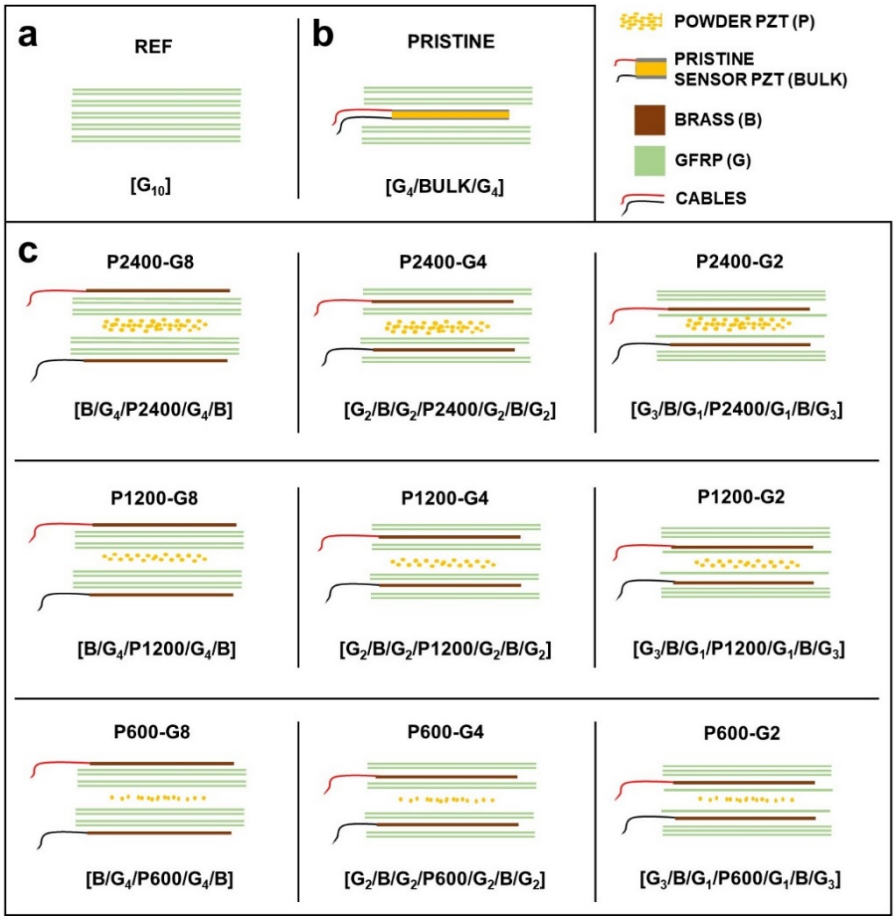

Figure 14: Laminates stacking sequences configurations: (a) reference non-sensing laminate, (b) laminate with embedded commercial sensor, (c) laminate with different amounts of PZT powder areal weight and GFRP plies between the electrodes.

Table 3: Specimens produced and relative configurations: density PZT (g/m^2), number of GRFP plies within electrodes, distance between electrode ((⌀ 20 × 0.1 mm for the upper electrode and ⌀ 30 × 0.1 mm for the bottom one) and volumetric fraction of PZT (v^P).

specimen	PZT (g/m^2)	n° GFRP within elect.	d (mm) within elect	v^P
P2400-G8	2400	8	2.42	0.14
P2400-G4	2400	4	1.44	0.24
P2400-G2	2400	2	1.08	0.39
P1200-G8	1200	8	2.17	0.07
P1200-G4	1200	4	1.29	0.14
P1200-G2	1200	2	0.88	0.24
P600-G8	600	8	2.06	0.04
P600-G4	600	4	1.11	0.07
P600-G2	600	2	0.72	0.14

2.5. PVDF-TrFE nanofibers in epoxy resin composites

Materials

In order to create functional composite materials based on PVDF-TrFE nanofibers embedded in a flexible epoxy resin and interleaved between custom conductive flexible electrodes, made of flexible epoxy resin functionalized with carbon nanoparticles, were fabricated.

The materials used in this Thesis to produce the PVDF-TrFE composite material were:

- PVdF-TrFE electrospun mat.
- Isopropanol (IPA) ≥ 99,5%; Cyclohexane anhydrous 99.5% were purchased from Sigma Aldrich.
- Epoxy resin (Itapox 108); blocked isocyanate polyurethane prepolymer (Synthane 2095); curing agent (Itamine CA119) kindly were provided by Ddchem S.l.r.
- Carbon Fiber Reinforced Polymer prepeg (CFRP, 200 g/m^2 twill fabric with 6K T800HB fibers MTM49- 3/CF1218-42%RW) was supplied by Solvay Cytec Industries Inc.

- Glass Fiber Reinforced Polymer prepreg (GFRP, E-glass 8H Satin 300 g/m^2 - epoxy matrix, VV300S - DT121H-34) was acquired from DeltaPreg.
- Carbon nanoparticles (Printex XE2B, BET surface area= 1000 m^2/g, average particles size= 30 nm) were purchased from Orion Engineered Carbons.

PVdF-TrFE electrospun-based composite

The scheme procedure to fabricate the piezoelectric sensor-based composite was represented in Figure 15.

To produce a PVDF-TrFE composite, a mixture of epoxy resin/blocked isocyanate polyurethane prepolymer = 70:30 wt % and curing agent (10:3 weight ratio) was prepared and poured on the nanofibrous membrane placed on Teflon support with a 100 μm thickness mask. The low viscosity of the mixture allowed a good penetration within the pores of the nanofibrous membrane. Then, the excess mixture was removed from the surface of the layer by means of a blade and the curing process was performed at 50°C for 2 hours. The innovative electrodes were realized by dispersing conductive carbon black nanoparticles in a polymer mixture (10:90 weight ratio) and adding 300 wt% of isopropanol to adjust the viscosity of the carbon dispersion. Then, the prepared carbon dispersion was left to magnetically stirred for 120 hours at RT.

Such a solution was deposited on the surface of the piezoelectric layer controlling the layer thickness (100 μm) by means of a mask and then was cured for 2 hours at 50°C. The same process was repeated for the opposite surface electrode. Furthermore, signal cables coated with a Teflon jacket were placed within the electrode layers prior to the curing process. The total thickness of the sensor is around 300 μm. Furthermore, reducing the signal-to-noise ratio, shield electrodes were added to the structure of the sensor with the same manufacturing process used for the signal electrodes.

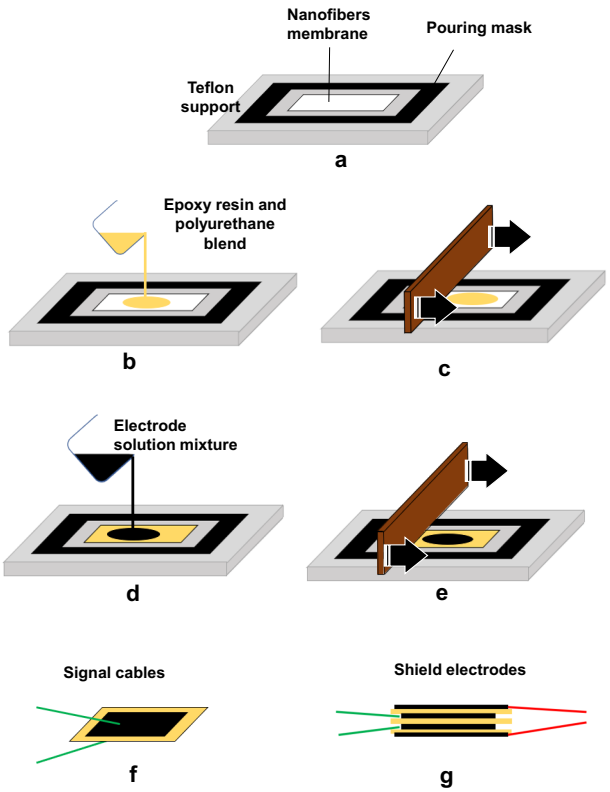

Figure 15: Schematic representation of the manufacturing process of the piezoelectric sensor: the 100 µm thick nanofibrous layer is placed on a Teflon support inside a 100 µm thick mask (a). The epoxy resin and polyurethane blend is poured on the nanofibers, penetrating in the porous membrane (b). A homogeneous 100 µm thickness of the layer is achieved by means of a blade to remove the excess material (c). After the curing process, the electrode solution mixture with Carbon Black nanopowder is poured on the surface of the piezoelectric layer (d) and its 100 µm thickness is made uniform (e). Steps (d) and (e) are repeated on the opposite surface and the signal cables are cured within the electrodes (f). Shield electrodes are added with the same process described (g).

The piezoelectric PVDF-TrFE sensor was integrated with a CFRP precured laminate, with a quasi-isotropic stacking sequence ($[0/\pm45/90]_s$ and 100 x 50 x 3 mm). A layer of GFRP prepreg (80 × 90 x ~0.22 mm) was stacked on the CFRP cured laminate. Then the piezoelectric sensor was placed on it and finally covered with another GFRP prepreg ply. Before stacking, the surface of the CFRP base was treated and grinded with sandpaper to improve the adhesion with the resin of GFRP layer. The curing process was then carried out in vacuum bag for 12 hours at 80 °C.

2.6. PLLA nanofiber in PDMS

Materials

The materials used in this Thesis to produce the PLLA composite material were:

PLLA electrospun mat;
Polyacrylic acid (PAA, MW= 450.000 Da), polydimethylsiloxane (PDMS, Sylgard® Silicone 184) and curing agent were purchased form Sigma Aldrich.

Curled nanofiber-based composite

In order to obtain the elastomeric composite materials made of nanofibers network embedded into elastomeric matrix and facilitate its production, a microscope glass slide was coated with water-soluble layer of PAA. PAA was dissolved in distilled water at 10 % wt and then was poured on a glass slide to coat the surface, then spin-coated for 20 s at 400 rpm and then the glass was placed on a heater plate at 80°C. PDMS was mixed with 10% (w/w) curing agent for 7 min and then it was placed in a vacuum chamber to remove air inside. Therefore, the 3-D composite were after were putted the PLLA strips on the microscope glass slide and PDMS was poured on the PLLA strips. Finally, to avoid excess of PDMS, the spin-coating process in single step at 800 rpm for 3 min was carry out. The obtained 3-D composite material was placed in oven at 70°C for 1h to cure the PDMS. At the end, to remove the composite material from the glass and to avoid tensile stretching of the structure, water was poured to solubilize the PAA substrate.

2.7. Characterization methods

Differential Scanning Calorimetry (DSC)

To study the thermal transitions of the polymer carrier, Differential Scanning Calorimetry (DSC) was carried out in nitrogen atmosphere by using a Q100 DSC apparatus (TA Instruments) equipped with a Refrigerated Cooling System (RCS90). Samples were placed in aluminium pans and subject to heating scans at 20°C/min from -90°C to a temperature higher than glass transition temperature (T_g) for completely amorphous polymer, while for semicrystalline polymer the temperature was increased higher than melting point (T_m). Quenching cooling or controlled cooling at 10 °C/min were applied between heating scans. T_g values were taken at half-height of the glass transition heat capacity step while crystallization temperature (Tc) and T_m were taken at the maximum of exothermic and endothermic peaks, respectively. The degree of crystallinity (χ_c) was calculated using the following equation:

$$\chi c = \frac{\Delta H_m}{\Delta H_m^0} \cdot 100 \qquad (2)$$

Where ΔH_m is the experimental melting enthalpy obtained from DSC scan and ΔH_m^0 is the melting enthalpy of 100% crystalline polymer.

Thermogravimetric analyses (TGA)

Thermogravimetric analyses (TGA) were carried out using a TGA Q500 thermogravimetric analyser (TA Instruments). Analyses were performed on 10-15 mg samples, from RT to 700 °C, at a heating rate of 10°C/min, under air flow.

Scanning Electron Microscopy (SEM)

The morphology and microstructure of the samples were investigate by Scanning Electron Microscopy (SEM), using the microscope Auriga Base (Carl Zeiss, Germany), equipped with an EDX modulus, at an accelerating voltage of 20 kV. Samples were fixed on an aluminium stub with a conducting bi-adhesive tape and were sputter coated with gold prior to analysis. Images were analysed with Image J software and the distribution of nanofiber diameters was determined by measuring about 150 fibers. The results were provided as the average diameter ± standard deviation.

Wide Angle X-Ray Diffraction (WAXS)

WAXS measurements were carried out at RT with X'Pert PRO diffractometer (PANanaltical, Almelo, the Netherland) equipped with an XCelerator detector. Cu anode was used as X-ray source (K radiation at a λ = 0.15406 nm, 40 kV, 40 mA) and ¼ divergence slit was used to collect data in range 2θ= 2 – 60° with a step size of 0.03° and a time of 60 s per step. The amorphous and crystalline phase were calculated by fitting method using Fityk program. The degree of crystallinity (χ_c) was calculated as the ratio of the crystalline peak areas to the total area under the scattering curve.

Transmission Electron Microscope (TEM)

Nanoscale structural and compositional characterizations were performed on an FEI Tecnai F20 high resolution transmission electron microscope (HRTEM), equipped with a Schottky emitter operating at 200 kV. The nanofiber were electrospun on the top of a carbon film coated Mo TEM grids, in order to minimize thermal dilatation occurring during thermal treatments. Thermal treatment at different temperatures was performed expect for the calcination process.

The PZT nanofibers, after calcination process, were dispersed in isopropyl alcohol and was then deposited on carbon film coated Cu TEM grids and dried at 150°C to be observed.

Atomic Force Microscope (AFM)

AFM measurements were performed, by prof. Tobias Cramer at the Department of Physics of the University of Bologna, on a Park NX10 system, Korea. Non contact mode AFM has been used for mapping the topography of both the single PLLA nanofiber and relative composite material. Contact mode AFM has been used for nanoindentation experiments to obtain the microscopic elastic moduli.

Dynamic Mechanical Analyser (DMA)

Mechanical tests were carried out using a DMA Q800 Dynamic Mechanical Analyser (TA instruments). Analyses were performed on strip of 3D composite material made of PLLA curled nanofiber embedded in PDMS matrix at RT. The clamp used is the so-called *tension-film clamp*, in which the sample is held from the edges between a fixed and a movable clips.

Two types of tests have been performed on the samples:

- Stress-strain tests, in which the sample is tensioned at 4% of strain rate for a number of four cycles deforming the sample along the main length from 0 to 4 %. The elastic modulus is obtained by fitting the linear relation between stress and strain, classically known as Hooke's law
- Multi-strain tests, in which the sample is pre-tensioned to reach a specific strain and then made to oscillate at different amplitudes at a defined frequency. During the amplitude sweep, the complex elastic modulus ($E = E' + iE''$) is acquired by considering the stress response during the oscillation. In E, the real part (E') depicts the elastic component that obeys the Hooke's law aforementioned, and it is called storage modulus. Instead, the imaginary part (E'') represents the loss of elasticity due to viscous relaxations and heat dissipation during the stretching. So, the results of multi-strain tests show the elastic and viscous component of the material at different pre-tension, or preload, by performing a stress-strain cycle deforming the sample at a specific frequency with different oscillation amplitudes. In these tests, the frequency was set at 1 Hz, the preloads range from 0.2 to 2.4 N increased with steps of 0.2 N, and the amplitudes range from 1 to 10 μm increased with steps of 1 μm.

Piezoelectric measurements

- The piezoelectric responses of the PZT powder laminates were evaluated with a compressive cyclic load by means of a hydraulic testing machine Instron 8033, equipped with a 25 kN load cell. Morphological The specimens were compressed between a flat support and a cylindrical indenter with a diameter of 10 mm made of plastic, to insulate the specimens electrically. A compressive force oscillating between 0.5 kN and 1 kN at 25 Hz was applied. A cyclic frequency of 25 Hz was chosen to be above the 3 dB cut-off frequency of the equivalent RC circuit, allowing a non-attenuated and frequency independent piezoelectric signal. Indeed, with a minimum equivalent capacitance ($C = C_s + C_c$) of 14.2 pF and a resistance R_a of 10 GΩ, the estimated cut-off frequency is equal to 1.1 Hz. The force measured by the commercial load cell and the piezoelectric signal were acquired simultaneously at a frequency of 2 kHz.

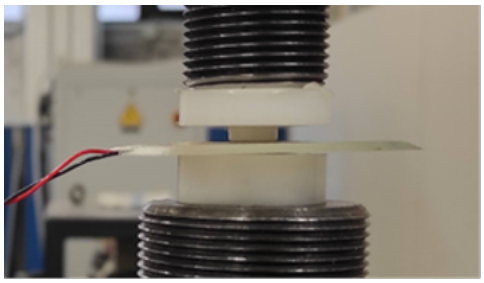

Figure 16: Cyclic force indentation setup

- The piezoelectric measure of PVDF-TrFE electrospun mats were measured trough the d_{33} PiezoMeter System, Piezotest, Singapore, www.piezotest.com
- The piezoelectric response of the PVDF-TrFE composites (in plate form) was evaluated at different frequency range by means of tension/compression machine ElectroPuls E1000 (Instron™ Norwood (MA), USA), equipped with a 2kN capacity Instron TM static load cell 2527-129 . The specimens were compressed between a flat support and a cylindrical indenter with a diameter of 10 mm made of plastic, to insulate it electrically. The acquisition circuit of the piezoelectric signal comprises an amplifier AD795JRZ mounted on a Single S08 Precision Amplifier Evaluation Board and the shields electrodes were connected to the ground. The amplifier was set in a buffer mode, so no signal amplifications were performed.

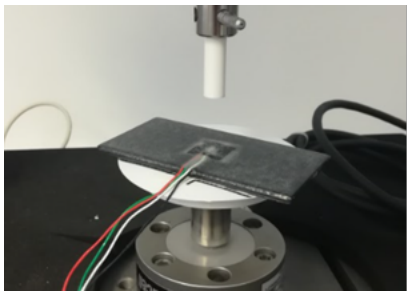

Figure 17:Cyclic force indentation setup.

Electrical measurements

- The conductivities of the single phases (GFRP and PZT) were measured by means of a pico-amperometer (Keysight B2981A).
- The dielectric constants of the single phases were measured by means of the dielectric analyzer (Novocontrol alpha dielectric analyzer B2.2) in the frequency range of $10^{-2} \div 10^{4}$ Hz.
- The impedances of the sensing laminates were measured in the 40 Hz ÷ 400 kHz range by means of the precision impedance analyzer Agilent 4294A. The capacitances were determined by interpolating the curve impedance vs frequency with the linear equation of the RC circuit.

Low Velocity Impact tests (LVI)

Low Velocity Impact tests (LVI) were performed to investigate the effect of interleaving the piezoelectric element in different morphologies and PZT/GFRP weight ratios on the impact resistance of the hosting laminate. Tests were performed according to ASTM D7136 on a low velocity impact equipment with a 1.3 kg impactor equipped with a PCB 208C05 load cell and a 12.7 mm hemispherical steel tip. Due to the small dimensions of the specimen and to maximize the shear stress, a support plate with a custom 20 mm diameter cylindrical hole was adopted. Specimens were impacted with an energy of 3 J and a velocity of around 2.2 m/s. Micrograph analysis of the laminates cross section at the impact point was performed to evaluate the damage.

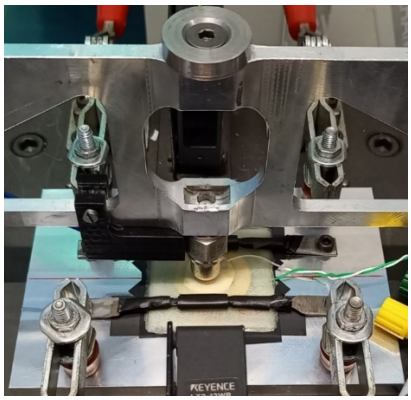

Figure 18: Low velocity impact setup.

Fatigue test

Accelerated cyclic fatigue tests were performed on the PVDF-TrFE composites (in plate form) by applying a sinusoid dal load oscillating between 1000 N and 400 N at 10 Hz frequency for 10^6 cycles by using the same setup for piezoelectric measurements (tension/compression machine ElectroPuls E1000 equipped with a 2kN capacity Instron TM static load cell 2527-129).

3. Results and discussion

The present Chapter is divided into three main sections:

i. PZT based piezoelectric devices
ii. PVDF-TRFE based piezoelectric devices
iii. Polymeric nanofibers for flexible electronics

The first two sections illustrate piezoelectric components based on ceramic and polymer nanostructured materials embedded in a polymer matrix to be used in prosthetic devices. The production and characterization of the piezoelectric elements were carried out at the Chemistry Department of University of Bologna, whereas the development and integration in the sole of a prosthetic foot as functional components was carried out at the Mechanical Engineering and Electrical Engineering Departments, University of Bologna. Finally, the prosthetic foot was tested thanks to the collaboration with the Faculty of Science and Engineering (University of Groningen).

The third section reports the development of polymeric nanofibrous materials capable to modify the mechanical properties of an elastomeric matrix by controlling the geometry of the incorporated nanofibrous network. The present research was carried out in collaboration with Prof. T. Cramer of the Physics and Astronomy Department.

3.1. PZT-based piezoelectric devices

3.1.1. PZT nanofibers production and characterization

The approach used in this dissertation to produce PZT nanofibers exploited the sol-gel electrospinning process and is divided in two main steps:

i) The first step is to prepare the PZT precursors solution that must be enough stable to be subjected to the electrospinning process, i.e. the process of gelification must be avoided before electrospinning.
After this step, the obtained as-spun nanofibers were thermally treated to allow the crystalline growth of PZT nanofibers dimensionally stable.

During this step, the large and rapid weight loss from the sample during heating could lead to a disintegration of PZT nanofibers. To study the effect of the polymer carrier on dimensional stability, two polymer carriers with different thermal features were employed.

ii) Once selected the optimal way to synthesis PZT nanofiber, detailed characterizations were carried out on them.

Synthesis of PZT solution

The procedure started with the synthesis of the PZT precursors' solution. $Zr(OPr)_4$, $Ti(OiPr)_4$ and $Pb(OAc)_2 \cdot 3H_2O$ were solubilized in a mixture of 2-MEO and Acetic Acid to obtain a stable solution as described in paragraph *PZT Synthesis* and reported schematically in Figure 11.

The method based on the chelation of the precursor, involves the exchange of the reactive alkoxide groups with the less reactive ligands of the acetic acid, acetate groups [109]. In particular, the first reaction is the nucleophilic substitution of acetic acid with one isopropoxide group of Ti isopropoxide and with two propoxide groups of Zr propoxide [101], [110]. The chelation reaction is reported below:

$$AcOH+M(OR)_x \rightarrow (AcO)M(OR)_{x-1}+ROH \quad (1)$$

Where R= iPr or Pr and M= Zr o Ti.

This process, where the lead acetate is dissolved in acetic acid followed by the addition of a zirconium alkoxide precursor and the titanium alkoxide precursor chelated by the acetic acid, create a PZT precursors solution that is stable when is diluted with 2-MEO and acetic acid is present in excess. Indeed, when Lead acetate interacts whit 2-MEO it forms a very stable acetate-methoxyethoxy lead complex [111] that, also contributes to turn this final solution into a very stable hydrophobic sol. After the exchange of alkoxide groups with acetate groups, free alcohol is released (iPrOH or PrOH) which reacts with the just formed acetates, resulting in the formation of alcohols and esters (2), which can be found in solutions

$$(AcO)M(OR)_3 + ROH \rightarrow (HO)M(OR)_3 + AcOR \quad (2)$$

$$(AcO)M(OR)_3 + (HO)M(OR)_3 \rightarrow (AcO)(OR)_2M\text{-}O\text{-}M(OR)_3 + HOR \quad (3)$$

The alcohol also reacts with the excess acetic acid to give ester and water, which triggers hydrolysis-reactions which lead to further formation of M-O-M bonds:

$$AcOH + ROH \leftrightarrow AcOR + H_2O \quad (4)$$

$$(AcO)M(OR)_3 + H_2O \rightarrow (AcO)M(OR)_2(OH) + HOR \quad (5)$$

$$(AcO)M(OR)_3 + (AcO)M(OR)_2(OH) \rightarrow (AcO)(OR)_2M\text{-}O\text{-}M\text{-}(OR)_2(AcO) + HOR \quad (6)$$

These reactions tend to continue until all the acetic acid has reacted with the isopropanol. The excess of acetic acid guarantees that the pH values of the PZT precursor solution, be well below the isoelectric points commonly accepted in the literature for the PZT system (pH= 7.87 or 7.42 in order that all particles are positively charged to avoid the aggregation[112] [113]. The pH of the PZT precursor solutions in this Thesis is about 5.4. the solution does not show sedimentation or precipitation and no appreciable change in pH values was detected. Similar behaviour was found by Suárez-Gómez on solution stocked for 1 years [113].

The PZT precursor solution, soon after preparation, was investigated by TGA analysis to evaluate concentration of ceramic PZT in the solution. TGA curve was acquired from RT to 700°C at 10°C/min and under air atmosphere and is shown in Figure 19.

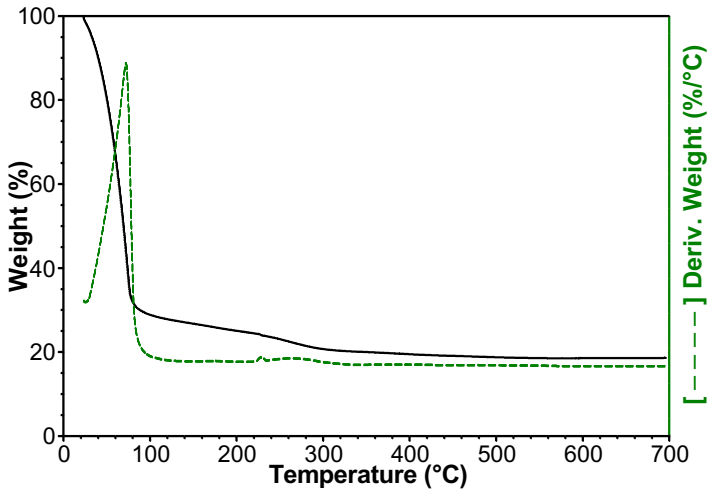

Figure 19: Thermogravimetric (black line) and derivative curve (green dotted line) of PZT precursor solution.

Table 4: Temperature of maximum rate of weight loss (T_{max}) and weight change (%) for each degradation step of the PZT precursor solution.

Range temperature (°C)	Δm (%)	T_{max} (°C)	Residue at 700°C (%)
RT- 150	73	72	-
150-350	7	-	-
350-550	2	-	-
550-700	-	-	18

The composition of PZT precursor solution is reported in Table 5

Table 5: Composition of PZT precursor solution.

PZT (116/52/48)					
QUANTITIES	REAGENTS			SOLVENTS	
	$Pb(OAc)_2 \cdot 3\ H_2O$	$Zr(OPr)_4$ 70% w/w	$Ti(OiPr)_4$ 98% w/w	2-MEO	AcOH
mol	0.0351	0.0156	0.0144	0.36	0.36
%	17.9	9.8	5.7	37	29.6
g	13.318	7.306	4.217	27.55	22.05

The TGA curve of PZT precursors solution shows three weight loss steps, which are reported in Table 4. The variations of the PZT system composition that occur during heating at a constant rate are reported in in Table 5.

The TGA analysis of a liquid solution has a certain error on the measure of weight due to the fast evaporation of volatile species present in the solution, which shows the temperature of maximum rate (T_{max}) of weight loss at 72°C. Moreover, the fast evaporation of the solvent, neutralizes the positively charged particles, favouring the aggregation until an amorphous inorganic network is formed from $Pb(OAc)_2$, ZrO_2, TiO_2. During the formation of the gel, other volatile species such as water and esters are produced which could be contributing whit weight loss in this step.

However, the first weight loss is comparable with the sum of the weight of the solvent and of secondary products derived from the sol-gel reaction. The species expected with relative theoretical weight loss and boiling points are 2-MEO (37%, 125°C), acetic acid (29.6%, 118°C), isopropanol (3.9%, 82°C), propanol (6.8%, 97°C). The theoretical weight loss is calculated based on the quantities of reagents and solvent added during the preparation of the solution and reported in Table 5.

The theoretical weight loss is about equal to 77% of the initial weight, while the observed weight loss in TGA is 73%. However, the shape of the curve near RT indicates that the evaporation of solvents is already taking place. In addition, during the synthesis procedure, inevitably a mass loss of the solvents occurs, justifying a lower weight loss observed than to the theoretical one. The difference between experimental and theoretical weight loss is about 5.5%.

Increasing temperature, between 150 and 350 °C, is possible to observe a slight weight loss of 7% and then a further loss of 2% within a temperature of 550 °C. In these ranges of temperature, is impossible to calculate T_{max} because the weight loss appears almost constant due to the pronounced first weight loss. The residue at 700°C is 18% of the initial sample indicating the concentration of synthesized PZT precursors solution. This value is very similar to the theoretical residue of 17% for PZT.

The precursors solution was dried for 72h and, after that, it was thermally treated in order to analyse the phase evolution from amorphous PZT sol-gel network to the expected final crystalline structure, following thermal procedure reported in paragraph *PZT powder*.

TGA analysis on the untreated gel and following each of heat treatment is shown in Figure 20a and relevant data are reported in Table 6 and Table 7.

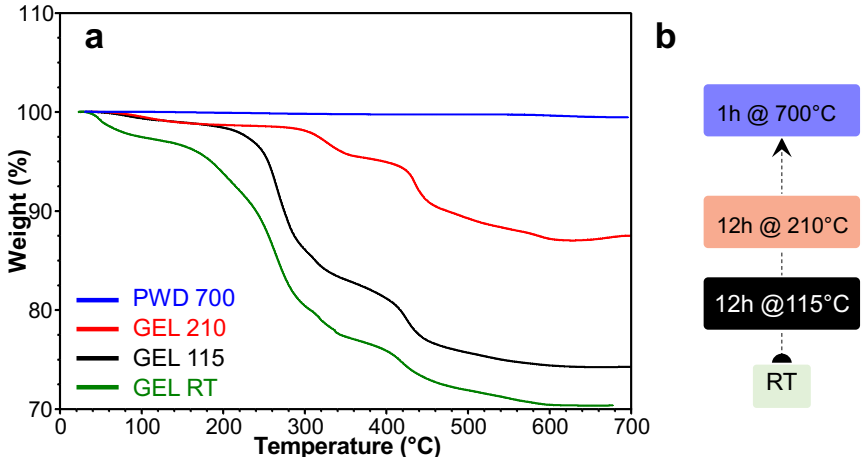

Figure 20: TGA curves of the PZT sol-gel network (a) treated at different temperatures until to calcination process (b). (10°C/min from RT to 700°C, in air)

TGA curve of dried GEL at RT, shows as expected, the highest solvent residues compared to other treatments, corresponding to first weight loss of 3%, due to the presence of residual solvents within the sol-gel network that are not immediately removed from the temperature gradient (10°C/min) of the TGA but which need more time to be removed.

For this reason, considerations on the PZT system composition were done starting from TGA curve of GEL after thermal treatment at 115 ° C for 12 hours. The TGA curve of GEL after treatment, shows three main losses: (i) equal to 1% from RT to 150°C, (ii) equal to 15% from 150°C to 350°C and (iii) 7% from 350°C to 700°C.

The first weight loss is attributed to volatilization of the solvents, i.e. residue of 2-MEO which evidently had not totally left the system or attributable to the moisture absorbed during the sample preparation. After complete evaporation of these species, the powder should be composed entirely of the amorphous TiO_2 and ZrO_2 gel and, as reported in the work of Chang et al., [102] lead acetate. This compound is characterized by a complex transformation from lead acetate to lead carbonate and finally, lead oxide. The reactions are shown below:

$$Pb(OOCCH_3)_2 \rightarrow PbCO_3 + CH_3COCH_3 \quad (7)$$

$$PbCO_3 \rightarrow PbO + CO_2 \quad (8)$$

In order to confirm the mechanism behind PZT formation, the composition of the system in the three temperature ranges reported above, was hypothesized also on the basis of the available literature. The composition, as well as the theoretical weight loss (Δm^{Th}) values at each temperature interval are outlined in Table 7.

The weight loss percentage theoretically calculated from the molecular masses of the species reflects the weight loss percentage values observed from the TGA curve. Weight loss of the GEL between 150°C and 350°C is mostly attributed to the transformation of $Pb(OAc)_2$ in $PbCO_3$ and, similarly, the weight loss from 350 to 700°C is due to conversion of $PbCO_3$ in PbO, reported in Table 7.

As is possible to see, the total theoretical weight loss due to the conversion of $Pb(OAc)_2$ to PbO in the temperature range from 150-700°C is 25%, equal to that observed by TGA analysis in the same range of temperature.

Slight differences of weight loss in each step are due to the multiple reactions of decomposition of lead acetate in a short range of temperature, as shown in the following [102]:

$$Pb(OOCCH_3)_2 \rightarrow Pb(OOCCH_3)_2 \bullet PbO \quad \text{I) } 220°\text{- } 270\ °C \quad (9)$$

$$\rightarrow Pb(OOCCH_3)_2 \bullet 2PbO \quad \text{II) } 270°\text{- } 310\ °C \quad (10)$$

$$\rightarrow PbO_{1-x}(CO_3)_x \quad \text{III) } 310°\text{ - } 350°C \quad (11)$$

$$\rightarrow PbO \quad \text{IV) } 350°\text{ - } 415°C \quad (12)$$

Given this result, it can be confirmed that the GEL, after thermal treatment at 115 ° C for 12 hours, is composed of TiO_2, ZrO_2, $Pb(OAc)_2$.

Also, the TGA curve of GEL after thermal treatment at 210°C for 12h, shows always three-step of weight loss in the same range of temperature, as reported in Table 6.
The total weight loss, from 150°C to 700°C is about 11%, perfectly consistent with the theoretical weight loss percentage reported in Table 7.
Obviously, the TGA curve of the sample treated at 700 for 1 h, does not show any weight loss.

Table 6: Temperature of maximum rate of weight loss (T_{max}) and weight change (%) for each degradation step of the PZT system during different heat treatments.

Range temperature (°C)	Δm (%)	T_{max} (°C)	Residue at 700°C (%)
	GEL RT		
RT- 150 °C	3	-	-
150-350 °C	20	264	-
350-700 °C	7	418	-
			70
	GEL after 115°C 12h		
RT- 150 °C	1	264	-
150-350 °C	15	425	-
350-700 °C	10	-	-
			74
	GEL after 210°C 12h		
RT- 150 °C	1	-	-
150-350 °C	3	325	-
350-700 °C	8	435	-
			88
	POWDER after 700°C 1h		
RT- 700°C	-	-	100

Table 7: Composition of the PZT system from sol-gel network to ceramic powder during each step of TGA analysis, according to [102].

Temperature range (°C)	Composition	Δm^{Th} (%)
RT-150	$Pb(OAc)_2$, ZrO_2, TiO_2	n.c.
150-350	$PbCO_3$, ZrO_2, TiO_2	$14^{(a)}$
350-700	PbO, ZrO_2, TiO_2	$11^{(b)}$
Total (150-700)		25

To confirm the composition of POWDER after thermal treatment and calcination process, XRD spectra was acquired and shown in Figure 21.

According to the literature study [114], the XRD spectra show typically peaks at 2θ 21.8°, 31.0°, 38.2°, 44.5°, 50.0° and 55.2°which individuates a PZT with composition located at Morphotropic Phase Boundary (MPB) where tetragonal and rhombohedral phase coexist. However, a non-ferroelectric second phase in the XRD spectra was present and exactly matches with the literature data [115] for the α-PbO (tetragonal phase) and β-PbO (orthorhombic) peaks, due to the presence of excess of leaf acetate in the synthetized solution.

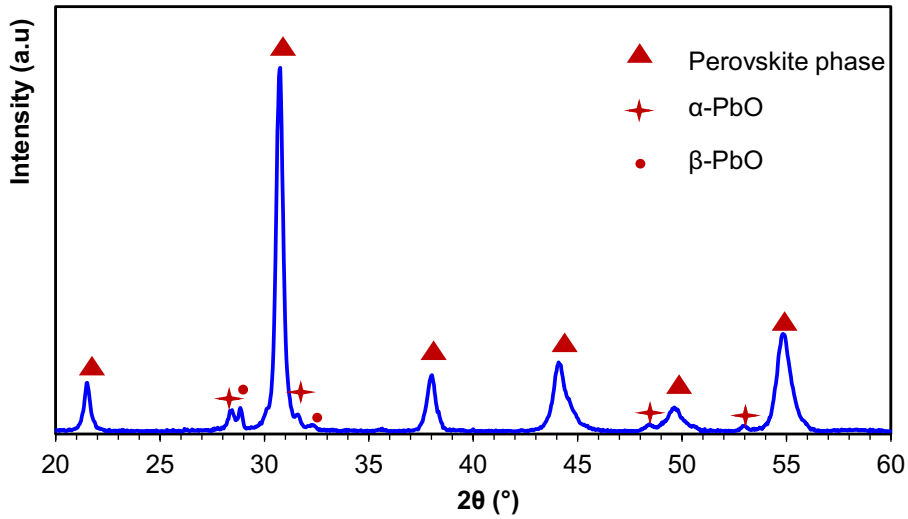

Figure 21: XRD spectra of PZT powder after thermal and calcination process.

Electrospinning process of polymer carrier/PZT precursors nanofibers

After the characterization of the PZT precursor solution, the polymer carrier was added to the precursors solution in order to adjust the viscosity of solution and have an electrospinnable solution. The polymer carrier must have precise features: (i) to possess the desired thermal properties, (ii) be soluble in precursor solution and (iii) be spinnable by electrospinning giving continuous fibers. For this reason, Polyvinyl acetate (PVAc) and Polyvinyl pyrrolidone (PVP) were selected as two possible polymer carriers. Usually, the PVP is most common polymer carrier used to obtain PZT nanofiber [104], [105],[106], [116], [117], [118], [119].

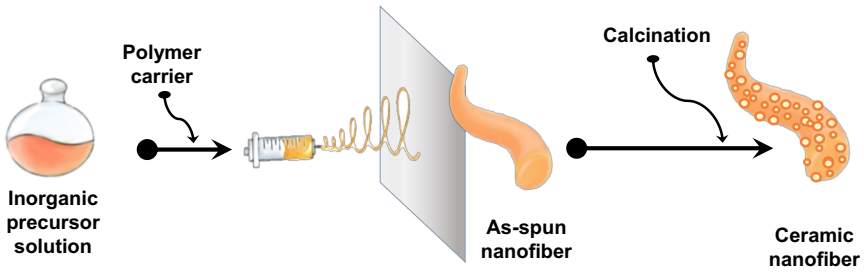

Figure 22: Typically process for fabrication of ceramic nanofiber

Figure 22 shows a typical process to obtain ceramic nanofibers starting from system inorganic precursor/polymer carrier solution through sol-gel electrospinning. As shown in Figure 22, after the spinning process, the as-spun nanofibers will be subjected to the calcination process to allow the oxide formation.

Therefore, in order to know the thermal transitions and the thermal degradation processes to which the carrier polymer will be subjected, DSC and TGA have been performed on PVAc and PVP electrospun mat (10% w/v in a mixture of 2-MEO:AcOH = 1:1 mol).

Table 8: Calorimetric data of the investigated polymers carrier.

Polymer	T_g(°C)	ΔCp [J/(g°C)]
[(a)]PVAc	[(a)]45	[(a)]0.48
[(b)]PVP	[(b)]180	[(b)]0.32

(a) Second scan after quenching from 20° to 160°C, heating at 20°C/min

(b) Second scan after quenching from 20°C to 250°C, heating at 20°C/min

Table 8 provides calorimetric data obtained from second heating scan of PVAc and PVP electrospun mats. Given the absence of backbone stereoregularity, a crystalline phase is not expected for both polymers. The glass transition temperature (T_g) occurs in different range for PVAc and PVP, reflecting a different chain's flexibility.

The TGA analysis was carried out in order to identify the degradation temperature of the polymer carrier. Results are reported in Figure 23 and Table 9. The TGA curve of PVAc electrospun mat shows a small initial weight loss attributed to the water and/or solvent evaporation. The thermal degradation occurs in three steps, although is difficult to separate second and third degradation steps. The main step of degradation occurs at 334 °C with weight loss equal to 70%, compatible with deacetylation, while between 400 and 600 °C, the evaporation of aromatic residue occurs [120][121]. For the PVP polymer, the thermal

degradation starts at similar temperature than for PVAc, that is about 300°C but the temperature of maximum rate of degradation is centred at 427 °C. In both cases, the polymer does not show residue at 700 °C.

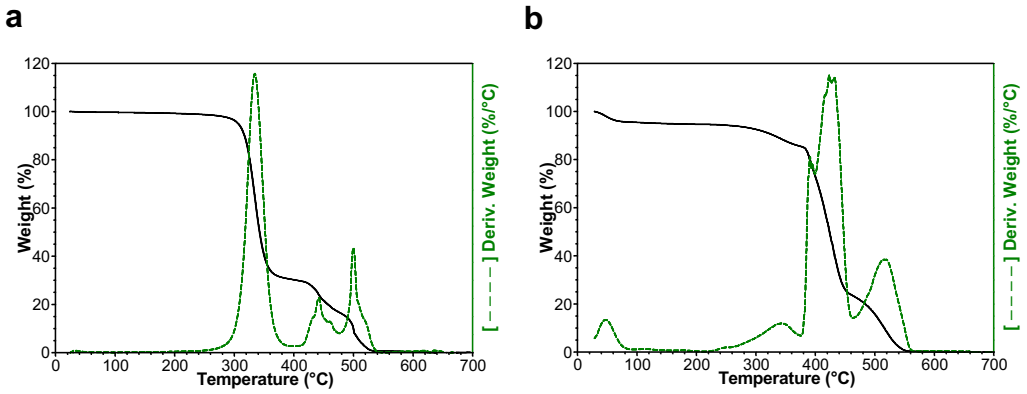

Figure 23: TGA curves (black, solid line) and derivate curves (green, dotted line) of PVAc (a) and PVP (b electrospun mat. (10°C/min from RT to 700°C, in air).

Table 9: Temperature of maximum rate of weight loss (T_{max}) and weight change (Δm) for each degradation step of PVAc and PVP electrospun mat.

Range temperature (°C)	Δm (%)	T_{max} (°C)	Residue at 700°C (%)
	PVAc electrospun mat		
RT- 100 °C	~ 0.4	-	-
100-400 °C	69.3	334	-
400-475 °C	14.6	440	-
475-560 °C	15.1	500	-
560-700 °C	~ 0.5	-	-
			0.1
	PVP electrospun mat		
RT- 100 °C	4.4	-	-
100-460 °C	72	427	-
460-600 °C	23.3	515	-
600-700°C	0.2	-	-
	-	-	0

To synthesized PZT nanofibers, the polymer carrier and PZT precursor solution were mixed. The pristine nanofibers composed by polymer carrier and GEL were obtained though optimized electrospinning following the condition reported in Table 10.

Applying a high voltage between the needle syringe tip and the grounded collector, the charged jet of the solution is elongated. During this process, the solvent is evaporated and the precursor/polymer are collected [122].

Figure 24 shows the SEM images of collected fibers, which are characterized by continuous fibers with a diameter distribution of 580 ± 110 nm and 1100 ± 300 nm for PVAc/PZT and PVP/PZT respectively.

Table 10: Optimized electrospinning conditions of polymer carrier/synthesized PZT solution.

Polymer	Concentration % (w/v)	Applied voltage (kV)	Flow rate (µl/min)	Working distance (cm)	Collector speed (rpm)
PVAc	10	16	8	16	70
PVP	10	10	16	10	70

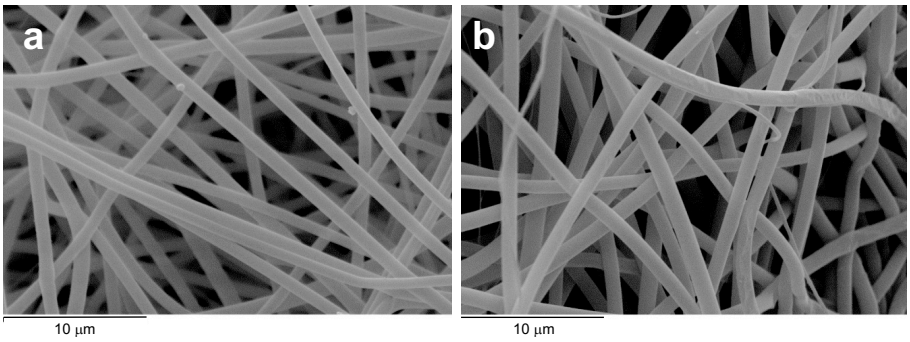

Figure 24: SEM micrographs PVAc/PZT (a) and PVP/PZT (b) electrospun mat.

The as-spun fibers can be transformed to oxide nanofibers by subsequent thermal treatment in air atmosphere, in order to remove the polymer matrix and to induce crystalline growth due to the oxidation of the inorganic precursors[122][122].

Thermal treatment of polymer carrier/PZT precursors nanofibers

To understand the behaviour of as spun nanofibers during the thermal treatment, TGA analysis was conducted. The obtained TGA curves are show in Figure 25.

Thermal degradation of as spun PVAc/PZT (Figure 25a) occurs in a single weight loss step in a temperature range between 200-300 °C with temperature of maximum degradation rate (T_{max}) at 280 °C. The initial weight loss between room temperature (RT) and 200 °C is attributed to volatilization of residue solvents from the electrospinning process.

A similar thermal degradation behaviour occurs for pristine PVP/PZT, but in this case the T_{max} is at 270 °C (Figure 25b). Therefore, for both materials, the residue at 700°C is attributed to PZT nanofibers that is about 49%.

In the range of 200- 350°C, the polymer carrier is completely removed and the lead transformation occurs. In this range temperature, is interesting to observe that the TGA curves deviate from the normal trace (Figure 25b). This rapid temperature change observed is due to the increase in temperature seen by the thermocouple caused for the combustion reaction.

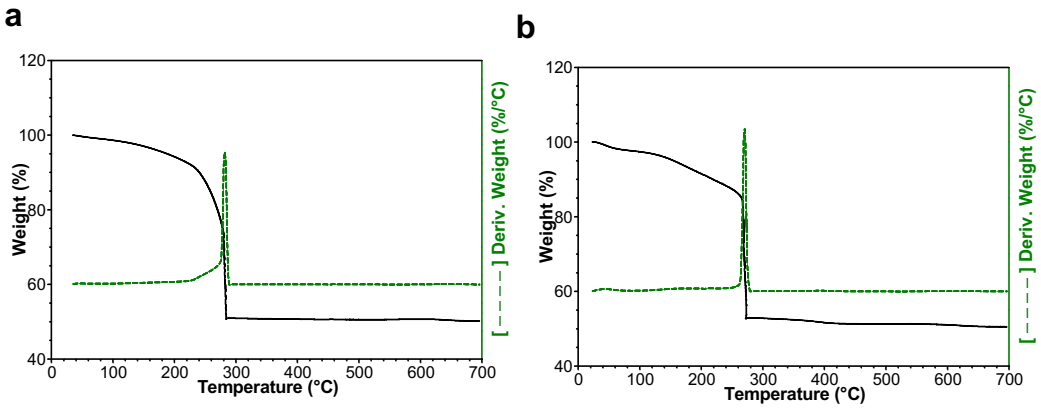

Figure 25: TGA curves (black, solid line) and derivate curves (green, dotted line) of the pristine electrospun ma, PVAc/PZT (a) and PVP/PZT (b); (10°C/min from RT to 700°C, in air).

The large and rapid weight loss from the sample during heating can lead to abrupt release of gas from the fibers resulting with their disintegration and leading to poor compositional homogeneity in PZT, decreasing also, the piezoelectric properties. The shrinkage behaviour of the electrospun mat is another factor to consider to allow a gradual relaxation and uniform thermal degradation during heat treatments [105].

Therefore, to avoid the main issues aforementioned, on the basis of the TGA results and of the Tg of the polymer carrier, the thermal treatments on polymer carrier-PZT nanofibers were optimized as follow: (i) keeping the mats in isothermal about to 70°C above the polymer Tg, (ii) keeping the mats in isothermal to the temperature to which show weight loss about to 7%.

The scheme of the thermal treatments and diameter size evolution, during thermal process of the pristine nanofiber for PVAc/PZT and PVPV/PZT are illustrated in Figure 26.

The obtained pristine PVAc/PZT nanofibers were stored at 115°C for 12 h to remove residual stress due to the electrospinning process. Next, the temperature was increased to 210°C for 12

h to allow a slow degradation of the polymer. Subsequently, they were calcined for 1h at 700°C to remove the residual polymer and to obtain calcined PZT nanofiber.

Instead, the obtained pristine PVP/PZT nanofibrous mats were stored at 250°C for 12h in air, where both stress relaxation and polymer degradation occur and then further calcined for 1h at 700°C to remove the residual polymer. Each isothermal step was reached with a ramp of 10°C/min and carried out in a muffle under in air atmosphere.

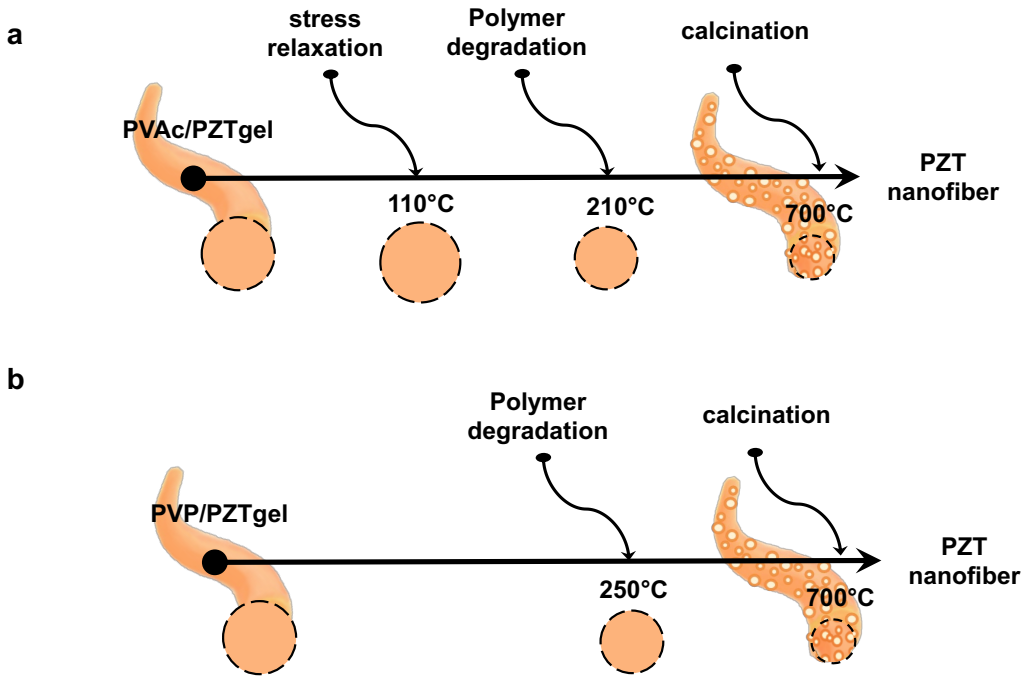

Figure 26: Scheme of the thermal treatments and diameter size evolution of the pristine nanofiber for PVAc/PZT (a) and PVP/PZT (b).

After each thermal treatment, TGA analysis, shrinkage measure and SEM image were carried out to confirm what was expected. Thermogravimetric analysis of the nanofibrous mats treated after different thermal treatments was used to characterize the composition polymer carrier/PZT nanofiber and was reported in Figure 27.

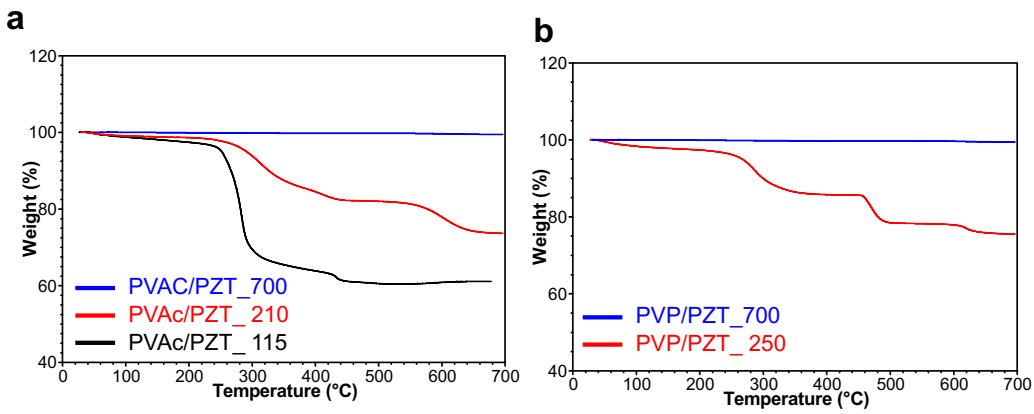

Figure 27: TGA curves of the nanofiber after different thermal treatments. PVAc/PZT (a) and PVP/PZT (b); (10°C/min from RT to 700°C, in air).

Table 11: Temperature of maximum rate of weight loss (Tmax) and weight change (%) for each degradation step of the polymer carrier/PZT nanofiber during different heat treatments.

Range temperature (°C)	Δm (%)	T_{max} (°C)	Residue at 700°C (%)	Range temperature (°C)	Δm (%)	T_{max} (°C)	Residue at 700°C (%)
PVAc/PZT after 115°C 12h							
RT- 150 °C	2	-	-				
150-350 °C	33	283	-				
350-700 °C	4	432	-				
			61				
PVAc/PZT after 210°C 12h				*PVP/PZT after 250°C 12h*			
RT- 150 °C	1	-	-	RT- 150 °C	2	-	-
150-380 °C	13	313	-	150-350 °C	11	287	-
380-450 °C	3	409		350-550 °C	8	470	
450-700 °C	9	600	-	450-700 °C	3	619	-
			74				76
PVAc/PZT after 700°C 1h				*PVP/PZT after 700°C 1h*			
RT- 700°C	-	-	100	RT- 700°C	-	-	100

The value of TGA curve in Figure 27a are reported in Table 11.

Observing the black curve relative to PVAc / PZT nanofibers after 115 ° C, a slight weight loss due to the removal of absorbed moisture can be observed.

The first main degradation step (33%) occurs between 150 and 350 ° C, and it is more gradual compared to as-spun fibers, demonstrating that during the treatment, the volatile products are removed as confirmed also by a higher residue at 700 ° C (61%). Moreover, analysing TGA

curve at 115 ° C, is possible to quantify the presence of a 18% (w/w) of PVAc in the PVAc/PZT nanofiber.
Such content was estimated based on the residue at 700 °C (PbO, TiO_2, ZrO_2 demonstrated earlier in Figure 21), from which it was calculated the stoichiometric quantity of the species present before the thermal treatment ($Pb(OAc)_2$, TiO_2 and ZrO_2) determining the polymer content by difference between experimentally initial weight and the theoretical weight .
After the treatment at 210 °C, the TGA curve shows a gradual weight loss between 150 and 450 ° C equal to 16% following by a continuous second weight loss until to 700°C equal to 9%.
These weight losses are attributed to the conversion of $PbCO_3$ to PbO as reported in Table 5.
In order to verify the complete conversion of $Pb(OAc)_2$ into PbO during the calcination steps, the calcined mat at 700 ° C was subjected to TGA which showed no weight loss.

Regarding PVP/PZT nanofibrous mat, the TGA curve in Figure 27b of mats heated at 250°C presents three main weight loss steps neglecting the initial weight loss attributed to water absorbed on the sample during the preparation for the analysis. First step of degradation is between 150- 350°C with a weight loss of 12 % and subsequently, loss 8% and 3% in the second and third steps, respectively between 350-550 °C and 550- 700°C.
These values, comparing the weight losses with Table 5 relative to the PZT gel transformations, suggest that PVP is no longer found in the fibres after storing the mats at 250°C, on the contrary, it may indicate that part (about 2%) of the transformation from carbonate to oxide has already begun during the isothermal treatment at 250 °C, indicating a composition of system composed by $PbCO_3$, PbO, TiO_2 and ZrO_2. These is agreement with the multiple reactions of decomposition of lead specie, as shown by Chang et al. [102].

In order to confirm the composition of the PZT nanofibers after thermal treatment and calcination process, X-ray diffraction was acquired and shown in Figure 28

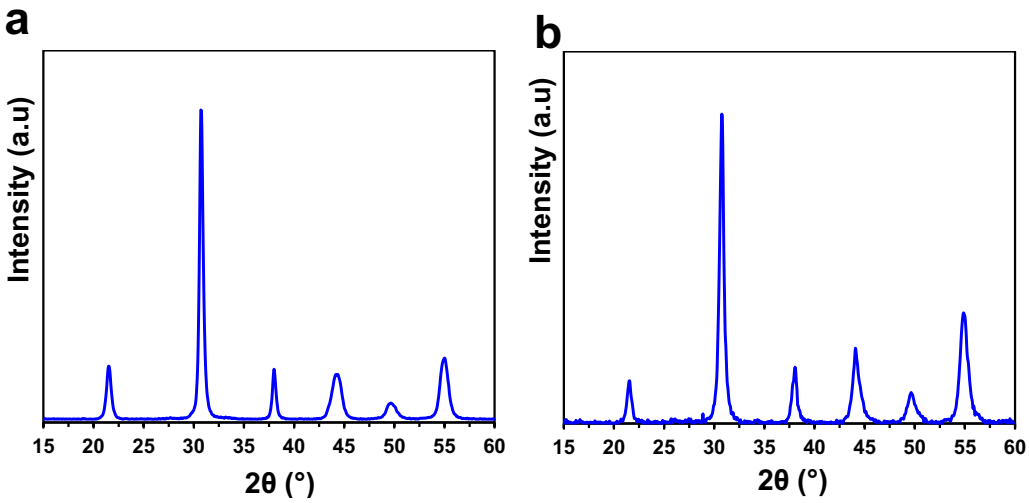

Figure 28: XRD spectra of PZT nanofiber after thermal and calcination process. a) PVAc/PZT and b) PVP/PZT nanofiber.

According to the literature study [114], the XRD spectra show typically peaks at 2θ 21.8°, 31.0°, 38.2°, 44.5°, 50.0° and 55.2° which individuates a ceramic PZT. This result is in agreement with the composition analysis performed by TGA for both electrospun mats.

Also, the energy-dispersive X-ray spectrometry (EDS) were conducted on calcined PZT nanofiber obtained using PVAc as polymer carrier. From collected EDS data, shown in Table 12, it is confirmed the homogeneous distribution of Pb, Zr and Ti. Moreover, the atomic ratio of Zr e Ti was approximately 1:1, which was consistent with theoretical stoichiometric molar ratio of Zr and Ti of the synthesised solution (116/52/48) reported in Table 5.

Table 12. Collected EDS data for PZT nanofiber.

	Calcined PZT		
	Atomic% Pb	Atomic% Zr	Atomic% Ti
Spectrum 1	17.06	9.37	7.96
Spectrum 2	17.70	9.36	8.69
Spectrum 3	17.06	9.32	7.96
Means ± dev.st	17.2 ± 0.4	9.35 ± 0.03	8.2 ± 0.4

Shrinkage behaviour of polymer carrier/PZT precursors nanofiber

During the thermal treatment two types of shrinkage occur microscopic and macroscopic.

The phenomenon of macroscopic shrinkage of the electrospun mat before and after each step of thermal treatment was measured from images as reported in Figure 29.

In Table 13 the relevant data of % shrinkage are listed, calculated as:

$$\%\, Shrinkage = \frac{Pi - Pf}{Pi} \cdot 100$$

Where:

- Pi is perimeter of the samples at RT;
- Pf is perimeter of the samples after thermal treatment.

The results, shown in Figure 29 and Table 13, indicate that the pristine electrospun mats undergo shrinkage and deformation during thermal treatment. In particular, Figure 29a-d shows representative macroscopic images of the PVAc/PZT mats at different steps of thermal treatment to produce the PZT nanofiber. The final PZT nanofibers obtained using PVAc as a polymer carrier are shown in Figure 29d, where the mat appears flat, even if with reduced dimensions.

On the contrary, mats using PVP as a carrier polymer were highly deformed and not usable, as shown in the representative image of Figure 29 g.

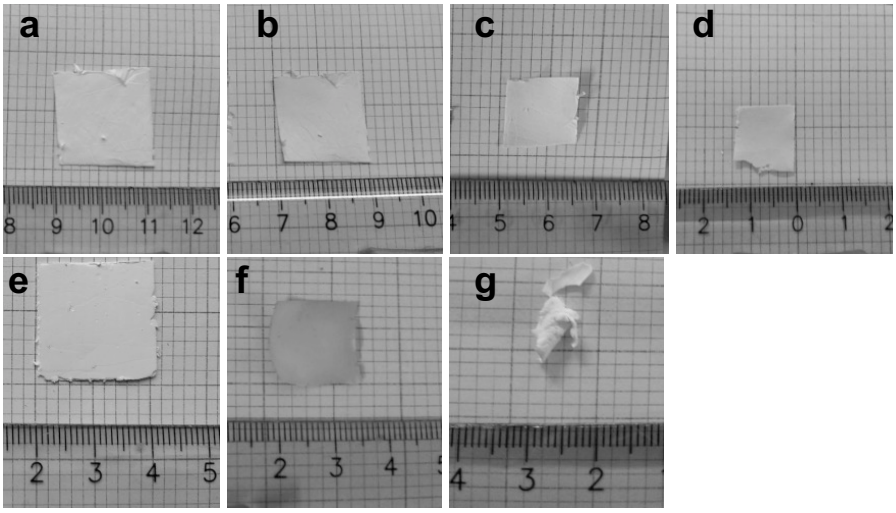

Figure 29: Macroscopic images of the nanofiber at different thermal treatments in air. PVAc/PZT nanofibers: Pristine (a), after stored 12h at 115 °C (b), after 12 h at 210 °C (c) and after 1h of calcination at 700°C (d). PVP/PZT nanofibers: Pristine (e), after 12 h at 250 °C (f) and after 1h of calcination at 700°C (g). Each isothermal step was reached with a ramp of 10°C/min and carried out in a muffle under in air atmosphere.

Table 13: *Shrinkage of the electrospun mats at each step of the thermal process. (Value expressed as mean of three samples).*

Sample	% Shrinkage		
	RT-115°C	RT-210°C	RT-700°C
PVAc/PZT	15 ± 3	23 ± 2	38 ± 5
		RT-250°C	RT-700°C
PVP/PZT	-	34 ± 4	n.d

To have information about the effect that thermal treatment and consequent shrinkage caused on the morphology of the nanofibers, SEM images were acquired. Figure 30 shows SEM images of PVAc/PZT and PVP/PZT nanofibers at different steps of the thermal treatments, while in Table 14 are reported the relative mean diameter of the fibers calculated on about 150 fibers using ImagaJ software.

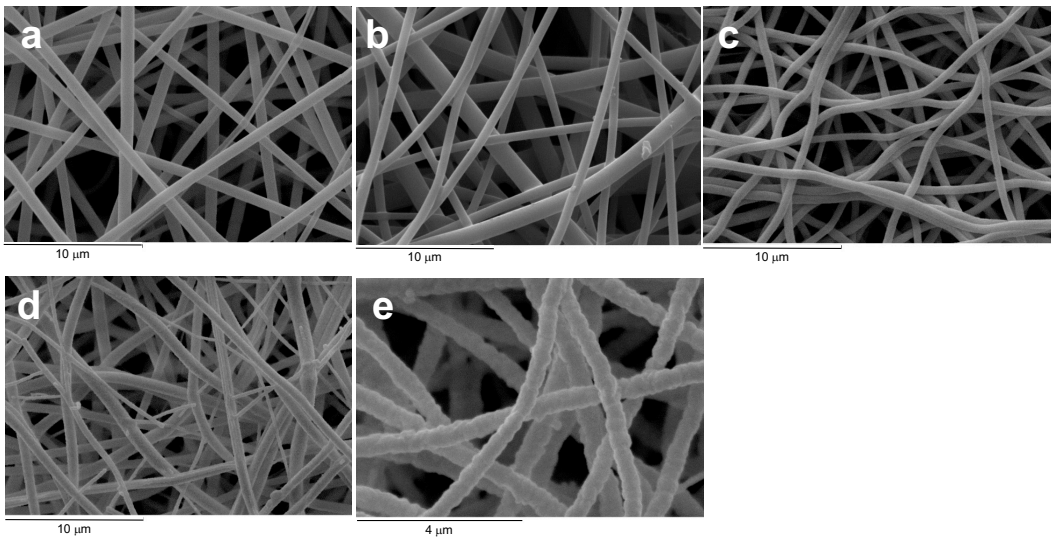

Figure 30: SEM images of the nanofiber at different thermal treatment in air. PVAc/PZT nanofibers: After stored overnight in an oven at 115 °C (a), after 12 h in an oven at 250 °C (b) and after 1h 40 min of calcination at 700°C (c). PVP/PZT nanofibers: After 24 h in an oven at 250 °C (d) and after 1h 40 min of calcination at 700°C (e).

Table 14: Mean diameter of the fiber at each thermal treatment.

Sample	Diameter (nm)			
	RT	115 °C	210°C	700°C
PVAc/PZT	580 ± 110	650 ± 120	500 ± 100	330 ± 60
	RT		250°C	700°C
PVP/PZT	1090 ± 280		610 ± 240	480 ± 220

The calcined PZT nanofibers obtained with PVAc polymer carrier, shown in Figure 30c, have dense structure, with ceramic grains tightly bonded with each other along the axial direction creating nanofiber of fused grains. Figure 30e shows SEM image of calcined nanofibers using PVP such as polymer carrier, have grains forming interstitial pores.
As can be noted from the Table 14, as-spun PVAc/PZT fibers have an average diameter of 580 nm, while after thermal treatment carried out at 115 ° C, the average diameter increases to 650 nm due to the stress relaxation of the polymer chains. This phenomenon, called shrinkage, reduces the length of the nanofibers increasing the size of the diameter. After thermal treatment conducted at 210°C, the average diameter of the fibers is reduced to 500 nm and then it is further to 330 nm after calcination step, due to the degradation of organic component and densification inorganic phase. The diameter of the nanofibers obtained from PVP/PZT constantly decreases, from 1090 to 480 nm. However, an increase in the diameter due to the entropic relaxation of the macromolecules is not noted when the temperature exceeds glass transition temperature because the degradation of the organic component is taking place, as confirmed by TGA analyses.

This result suggests that using a polymer with a T_g at temperature considerably lower than the T_{max} of the polymer in the presence of the precursor PZT, makes the relaxation and polymer degradation process more gradual. A slow degradation of the carrier polymer, achieved thanks to pre-treatments described, is necessary to allow an oxide particles densification leading to fibers with low porosity.
For these reasons, in this Thesis, PVAc was used as carrier polymer to synthesize PZT nanofibers.

Crystalline structure of PZT nanofiber

The structural evolution and the crystallization kinetics of the PZT nanofiber obtained using PVAc as polymer carrier, were investigate thought XRD analysis to determine the stoichiometric composition of precursor solution to preserve the optimal piezoelectric composition of the PZT nanofibers during the process.
Usually, the structure evolution of PZT nanofibers from non-ferroelectric phase (pyrochlore structure) to ferroelectric phase (perovskite structure) have been analysed by XRD starting from as spun and after thermal treatment from 400°C to 700°C [123]. It is widely confirmed that the perovskite phase formation occurs by overcoming the activation barrier of 0.45 eV (transition phase pyrochlore-perovskite) which process requires temperatures above 650 ° C [106], [107].

From studies conducted on powders and films it was concluded that lead oxide positively influences the kinetics of perovskite formation acting as seed of crystallization [124]. Usually, to avoid the loss of PbO during the calcination step due to its low pressure vapour [125], the lead salt was added in excess in the starting precursor system and/or working under PbO-saturated atmosphere [126]. These issues can be amplified in the sintering of nanofibers, due to a higher surface to volume ratio compared with films or bulk, compromising the composition of the PZT.

Thus, starting from three different PZT precursor solutions in terms of amounts of lead , powder and nanofibers were produced. Nanofibers with different amount of lead were subject to the same thermal treatment to demonstrate the lead effect on the perovskite transformation. While, powders and nanofibers with the same composition were analysed to show the effect of the morphology on the lead oxide volatility.

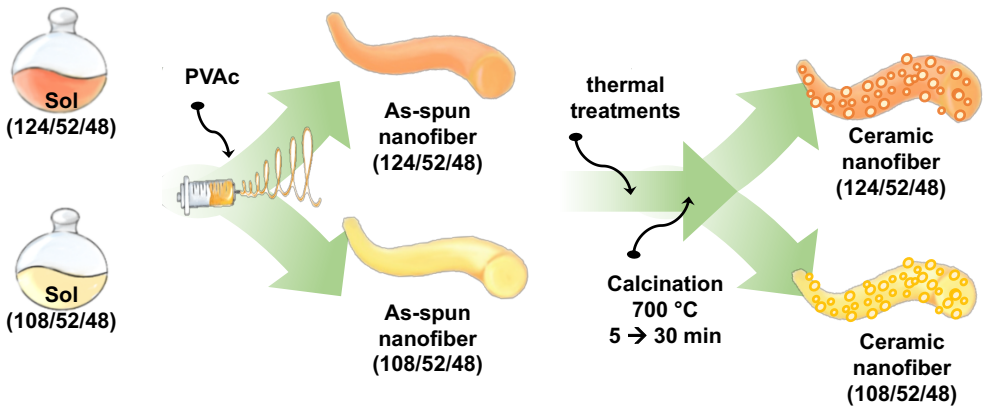

Figure 31: Schematic illustration of the procedure for the fabrication of PZT nanofibers starting from PZT precursor solution with different amounts of lead. Solutions obtained were mixed with a PVAc polymer carrier and then electrospun in order to obtain the PZT nanofiber precursor. Then, nanofibers were subjected at the same thermal treatments, 115°C for 12 h and then at 210°C for 12h, before the calcination process at 700°C for 5, 10, 15, 20 and 30 minutes.

As shown in Figure 31, following the mentioned procedure described in paragraph *PZT Synthesis* , Table 1 and reported schematically in Figure 11, two solutions of PZT whit different concentrations of lead acetate (8 and 24 mol% excess) were prepared in order to produce nanofiber of PZT. The formation of organic–inorganic nanofiber network was obtained controlling solvent evaporation during sol-gel electrospinning and where the presence of polymer carrier, plays a significant role acting both as a tackifier and as template allowing the electric field application and promoting the gelation process [127].

In the thermal treatments, the as-spun nanofibers were placed in the oven at a temperature above the glass transition of polymer to allow chain relaxation and at the same time, to permit the complete evaporation of the solvents. Subsequently, a series of transformations take place when the temperature was increased leading to organic decomposition as reported in *Thermal treatment of polymer carrier/PZT precursors nanofiber.*

After these steps, to follow the crystalline phase evolution as a function of the molar excess of lead, the nanofibers obtained using the PZT precursor solution with composition 108/52/48 and 124/52/48, were synthesized under the same condition. In particular, the as-spun nanofibers were thermally treated in the oven at 115°C for 12 h and then at 210°C for 12h, before the calcination was process carried out at 700°C for 5, 10, 15, 20 and 30 minutes into muffle. Each isothermal step was reached with a ramp of 10°C/min and carried out under in air atmosphere. After calcination process, the PZT nanofiber were rapidly quenched and the crystal structure was analysed. Acquired XRD were shown in Figure 32.

The dynamic regression of the pyrochlore phase of nanofiber (108/52/48) is shown in Figure 32a. As can be seen, increasing the calcination time, the perovskite phase becomes dominant, as evidenced by the intensity of the increasing peaks and at the same time by the intensity of the decreasing peaks of the pyrochlore phase. However, the pyrochlore phase remains present like if the amount of lead, that should diffuse into the pyrochlore phase to form a pure perovskite phase was insufficient [128]. Usually, the intermediate phase exists in a limited temperature range between 400° and 540°C, but this phase, is much more stable in the PZT system when the lead oxide concentration decreases due to desorption below a critical limit [129].

Therefore, the same treatment was carried out on nanofiber (124/52/48) to determine the impact of lead content, at the same condition of temperature and time calcination, on the crystalline structure. In this present case, shown in Figure 32b, just after 5 minutes at 700°C, the pure perovskite phase was formed. This result is consistent with (i) the remarkably low energy relative to the PZT in pure perovskite formation due to the lead effect. Chang et al. based on the activation energy values for pyrochlore-to-perovskite transformation of the PZT powder, had deduced that the PbO serves as the seeding sites for the PZT formation. (ii) For the nucleation and growth of the perovskite phase, a certain minimum amount of lead is required to promote the crystallization of the PZT perovskite from the amorphous phase and partially, to avoid the intermediate pyrochlore phase[128].

Here we used a large excess of lead, of 24% molar excess in the precursor solution, differently from what has been done in other works where usually, it was added 10% of lead in excess to

synthesize the PZT nanofiber and to compensate for the lead loss during the process [104], [105], [130].

However, being the PZT material in the form of nanofibers, the loss of PbO can be influenced by the high surface-to-volume ratio of nanostructures.

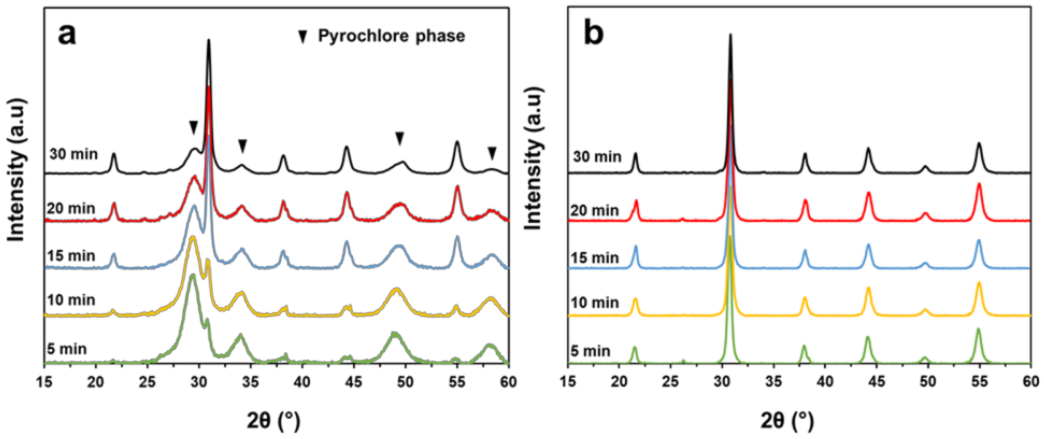

Figure 32: XRD spectra of the PZT nanofibers calcinated at 700 °C for a different time. Comparison of the perovskite phase formation on PZT nanofiber obtained using two different concentrations of Lead in the PZT precursor solution: sol(108/52/48) (a) and sol(124/52/48) (b).

To confirm this hypothesis, PZT nanofibers and PZT powders were produced and analysed starting from three different solutions in terms of lead concentration whit composition: 108/52/48, 116/52/48 and 124/52/48 followed the procedure reported in *PZT Synthesis*, Table 1 and reported schematically in Figure 11.

The procedure to obtain PZT powders is shown in Figure 33. PZT precursor solutions were poured in a glass petri dish to allow the gelification, then were scratched, ground into a fine powder and finally, transferred in a crucible.

In order to investigate the morphology effect on the lead oxide volatility, the as-spun nanofibers and GEL powder were subjected to the same thermal treatment.

In particular, the as-spun nanofibers and GEL powder, were thermally treated in the oven at 115°C for 12 h and then at 210°C for 12h, before the calcination was process carried out at 700°C for 1 hour into muffle. Each isothermal step was reached with a ramp of 10°C/min and carried out under in air atmosphere. After calcination process, the samples were rapidly quenched and the crystal structure was analysed. Acquired XRD were shown in Figure 34.

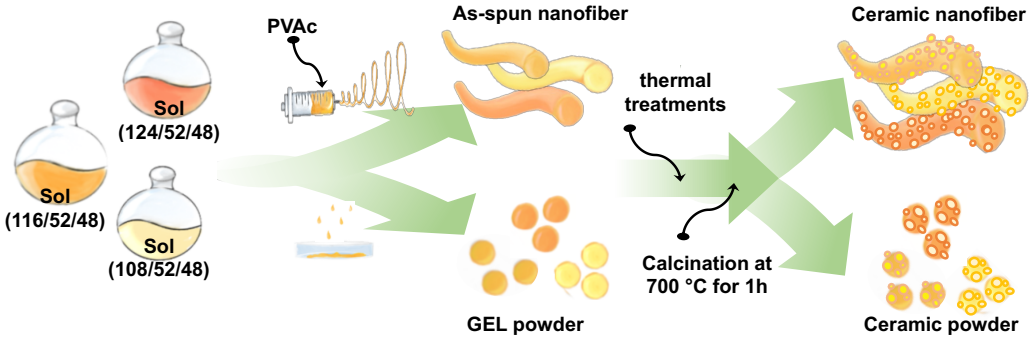

Figure 33: Schematic illustration of the procedure for the fabrication of ceramic PZT using three different solutions: sol(108/52/48), sol(116/52/48) and sol(124/52/48) to obtain PZT nanofiber and PZT powder whit different lead compositions. Solutions obtained were mixed with a PVAc polymer carrier and then electrospun in order to obtain as-spun nanofiber, while to obtain Gel powder the obtained solutions were poured in Petri dishes and kept at RT for 72 h. Then, their were subjected at the same thermal treatments, 115°C for 12 h and then at 210°C for 12h, before the calcination process at 700°C for 1 hour.

Figure 34a-b displays the XRD spectra of the PZT powders at various concentrations of lead. As shown XRD spectra a non-ferroelectric second phase in the calcined powder was present for all samples analysed and exactly matches with the literature data for the PbO peaks.

The lead oxide appears in the powder but not in the corresponding nanofiber as seen in Figure 34c-d. Powder and nanofibers have been obtained from the same precursor solution and treated whit the same thermal treatment, therefore, the only possible reason to explain the different XRD spectra is due to the morphology.

In other words, the presence of a strong excess of lead in the precursor solution used to produce PZT nanofibers favours the formation of the pure perovskite phase and does not cause a loss of ferroelectric properties due to the presence of a second non-ferroelectric phase, which either the pyrochlore intermedia or the lead oxide residue. For these reasons, we chose to use sol(124/52/48) for PZT nanofiber production.

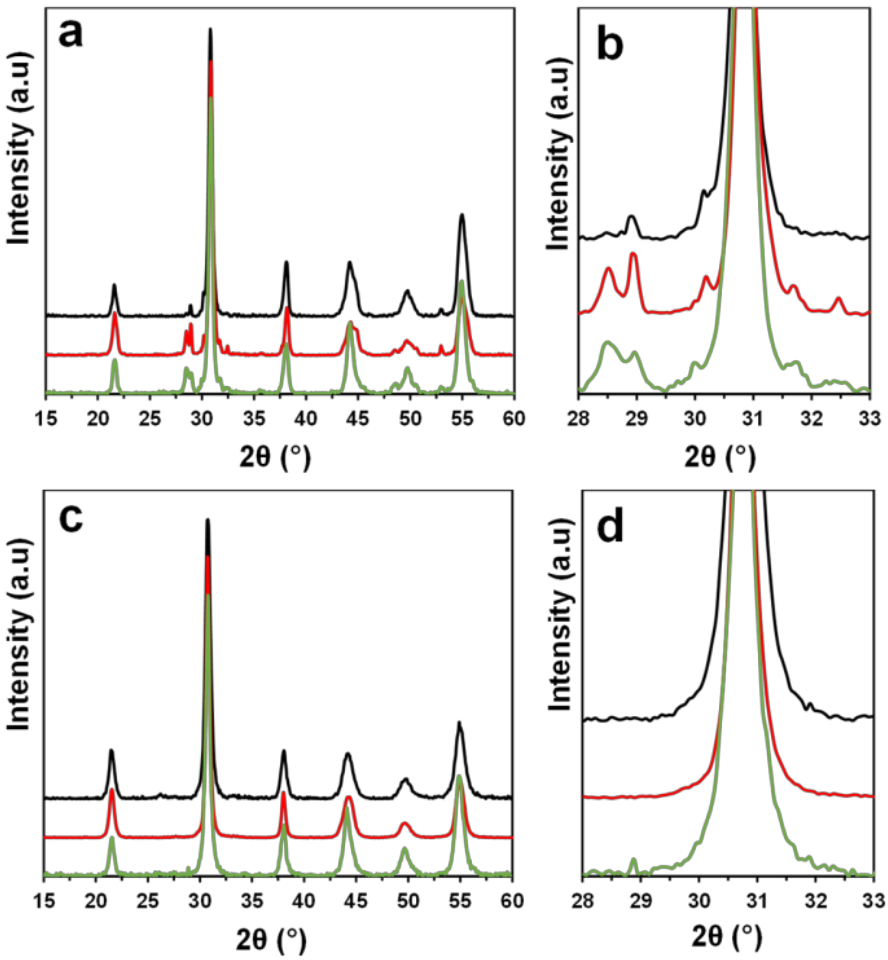

Figure 34: XRD spectra of the PZT powders (a-b) and nanofibers (c-d) obtained from PZT precursor solutions with different lead concentrations: sol(108/52/48) (black line), sol(116/52/48) (red line) and sol(124/52/48) (green line).

To follow detail morphological and crystal structure of the PZT nanofibers during synthesis, TEM and HRTEM analysis were performed after each thermal treatment and shown in Figure 35.

The nanofibers were electrospun on the top of a carbon film coated Mo TEM grids, in order to minimize thermal dilatation occurring during thermal treatments. Thermal treatment at different temperatures was performed except for the calcination process. The PZT nanofibers, after calcination process, were dispersed in isopropyl alcohol and were then deposited on carbon film coated Cu TEM grids and dried at 150°C. The TEM images of the nanofibers as spun and then thermally treated (Figure 35: a-c) show a smooth surface, except for the calcined PZT nanofibers (Figure 35 d) characterized by sintered nanoparticles. All samples show regular nanofiber shape.

In Figure 35 e-g the high magnification image and electron diffraction pattern (insert image) display amorphous structure for the nanofiber. Only the calcined nanofibers (Figure 35h) show crystalline features. The lattice place spacing measured from the HRTEM image is equal to 2.8 Å corresponding to the (101) plane of perovskite PZT with composition Pb ($Zr_{0.52}Ti_{0.48}$) O_3.

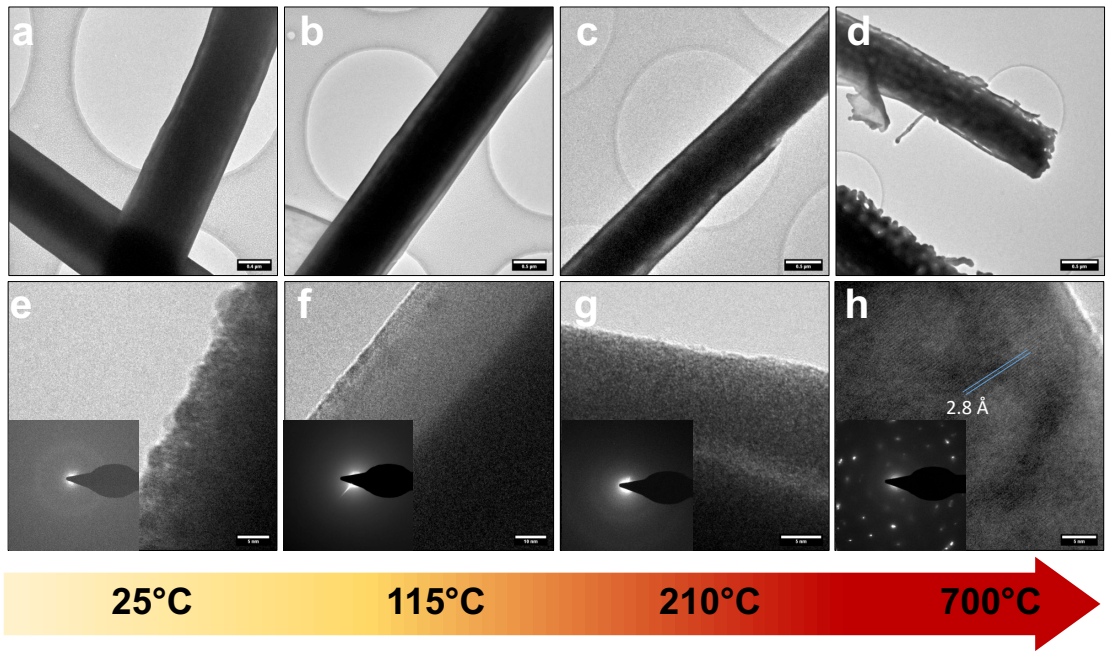

Figure 35: TEM micrograph (a-d), HRTEM and SAED pattern (in the insert)(e-h) of the PZT nanofiber at different steps of thermal treatment.

In summary, perovskite PZT nanofibers have been successfully fabricated by sol–gel based electrospinning. The composition of the PZT solution precursor was optimised to guarantee the stoichiometric composition of PZT nanofiber at $Pb(Zr_{0.52}\ Ti_{0.48})O_3$. Using TGA analysis was possible to optimize the thermal treatment and understand the composition of the PZT system at each step of the process. Moreover, through accurate study carried out on polymer carrier and polymer carrier /PZT it was possible to select PVAc which allows to obtain PZT nanofibers dimensionally stable with densely packed grains.

3.1.2. PZT powder-based composites

To realize and optimize the design of self-sensing composite laminate materials exploitable in MyLeg project, but also in the robotic applications (e.g., rehabilitation/assistive robotics), PZT powder was chosen for its availability, simple production and possibility to obtain it in large amount quantity.

As previously introduced in the Preface, the doctoral thesis has been conducted in the context of MyLeg H2020 project in with the aim to develop composite transfemoral with embedded piezoelectric elements for sensor in the sole.

In this way it is possible to increase the perception of the ground conditions during the walking by the sensor placed on the sole of the prosthesis to sense the contact/no-contact events.
Furthermore, the main advantage of piezoelectric sensors is that they do not need an external power supply as it is possible to convert the energy of human movements into voltage.
In particular, during the gait cycle, the integration of piezoelectric material under the sole of the prosthetic foot represents a good possibility of energy conversion, exploiting human weight.

According to the above considerations, a smart laminate was designed and prepared whit a non-invasive method for the piezoelectric functionalization of the composite laminate in collaboration with research group of Prof. Andrea Zucchelli (Department of Industrial Engineering and Prof. Davide Fabiani (Department of Electrical, Electronic, and Information Engineering), University of Bologna.
The approach to produce smart laminate is divided in two main steps:

i) In order to study mechanical and electrical proprieties in terms of impact resistance of the hosting laminate and sensor performance, the first step is to produce the composite laminate by interleaving PZT micrometric powder between Glass Fiber Reinforced Polymer (GFRP) plies in different PZT/GRFP volume ratio and morphologies, as described in paragraph ‘
ii) *Morphological characterization of the* PZT powder *’*.
iii) Then, the electrical, piezoelectrical, mechanical proprieties were carried out and a piezoelectric model was developed to correlate the volumetric fraction of the two phases and the polarization process of the laminates with the electromechanical responses to impact and to predict the piezoelectric voltage coefficient (g_{33}).

Morphological characterization of the PZT powder

Figure 36 shows the SEM micrographs of the PZT powder obtained after grinding the piezoelectric element. obtained after grindind. The distribution of particles dimension show two peaks, one with an average size of 24.6 ± 10.9 μm and another of 2.06 ± 0.26 μm.

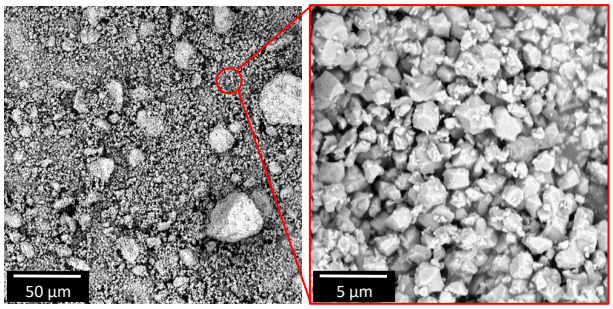

Figure 36: SEM micrographs of PZT powder.

Electrical characterization of single phase: PZT and GFRP

The piezoelectric behavior of the composite and the electrical properties of its single constituents were experimentally measured in order to understand the effect of their volumetric fraction (ν) on the electromechanical response of each sample configuration in with engineering department.

The measurements of the electrical properties of the single phases (PZT and GFRP) and smart composite laminate configurations were conducted, thanks the collaboration of engineering departments, in order to validate the proposed polarization and piezoelectric process model. Finally, the impact resistance of each smart composite configurations were compared. The measure of electrical proprieties relative to the single component were conduct by Giacomo Selleri.

To know the dielectric constant and conductivity of the single phase, piezoelectric element and GFRP, at the working and polarization temperature, were measured at 20°C and 100°C and reported

Table 15.

Table 15: Dielectric constant (ε) and conductivity (σ)of the single phases PZT and GFRP at different temperature.

	ε @ 20°C (F/m 10^{-12})	ε @ 100°C (F/m 10^{-12})	σ @ 20°C (S/m 10^{-15})	σ @ 100°C (S/m 10^{-15})
PZT	15937	20364	223	2600
GFRP	58	60	4	143

In particular, the permittivity values were determined at regime state in the frequency domain, reached at 10^4 Hz while the conductivity values are determined at regime state, which was reached after 8 hours. Comparing PZT and GFRP permittivity values, a difference of three order of magnitude can be observed for both temperatures. The conductivities difference between the two phases at 20°C is two orders of magnitude, which drops to one order of magnitude at 100°C. This conductivity gap reduction between the two phases at 100 °C, is crucial for the polarization process.

In Figure 37 the experimentally measured d_{33}^P piezoelectric strain coefficients of piezoelectric element are plotted for different electric fields magnitudes applied during the poling process at 100 °C for 24 hours (represented by black dots). The d_{33}^P was measured, with the same procedure used for the smart composite laminate, with a compressive cyclic load (specific reported in paragraph *Piezoelectric measurements)*

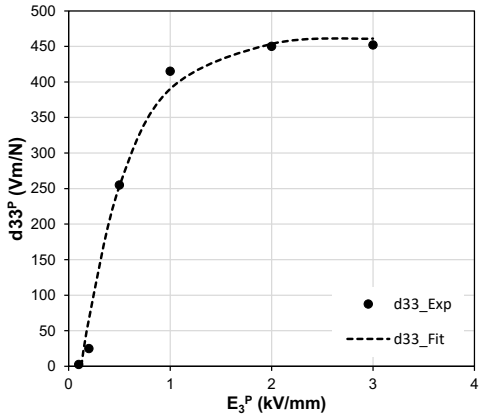

Figure 37: PZT piezoelectric strain coefficient d_{33}^P vs poling electric field E_3^P for 24 hours at a temperature of 100 °C.

Experimental data were then interpolated with the exponential function described in equation (1), by using the nonlinear least square method:

$$d_{33}^P = a * \left(1 - e^{bE_{3ss}^P}\right) - c \tag{1}$$

where the fitting coefficients a, b and c are equal to 614, 2.19 and 143, respectively. The interpolating equation is represented in the graph by the dotted line and has a coefficient of determination (R^2) equal to 0.985. As it can be observed, the d_{33}^P rapidly increases with the electric field and then stabilizes at a value of 450 Vm/N after 2 kV/mm.

Piezoelectric characterization of PZT composite

Compressive cyclic loads, as described in paragraph *'Piezoelectric measurements'*, were used to evaluate the piezoelectric sensitivity of each specimen of the PZT laminates produces. In Figure 38 the piezoelectric responses for samples P1200-G8, P1200-G4 and P1200-G2 were reported to show in general, the piezoelectric behaviour of composites as a function of the number of GFRP plies and PZT amount. Variations in the magnitude are registered, showing a peak-to-peak piezoelectric output increase as the number of GFRP plies within the electrodes decreases.

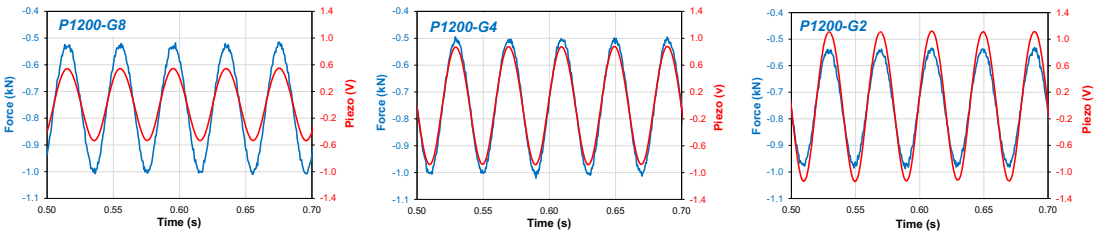

Figure 38: Piezoelectric response of the PZT laminate (red curve) compared to the contact force measured by the indenter load cell (blue curve) for powder sensor with 1200 g/m^2 and different plies of GFRP within the electrodes (8-4-2, respectively).

The sensitivity as a function of the number of GFRP plies for all configurations of laminate was shown in Figure 39 and reported in Table 16.

The sensitivity of each laminate is calculated as the ratio of the peak-to-peak value of the piezoelectric output to the applied force. A sensitivity value of 2.31 V/kN was measured for the pristine sensor embedded in the composite laminate (BULK, yellow point). Generally, it can be observed that changing morphologies of the piezoelectric material integrated in the laminate composite, from bulk to powder, the sensitivity enhances, especially for 1200 g/m^2 and 2400 g/m^2 PZT powder areal densities (yellow point vs green and red curves). Moreover, by decreasing the number of GFRP plies interleaved between the electrodes, the sensitivity is considerably improved. Indeed, it can be reasonably assumed that a thickening of the layer with a low dielectric constant acting as an insulating layer, results in a charge flow reduction towards the electrodes. Lastly, for PZT powder laminates an exponential increase of the sensitivity as a function of the powder-to-resin weight ratio can be observed.

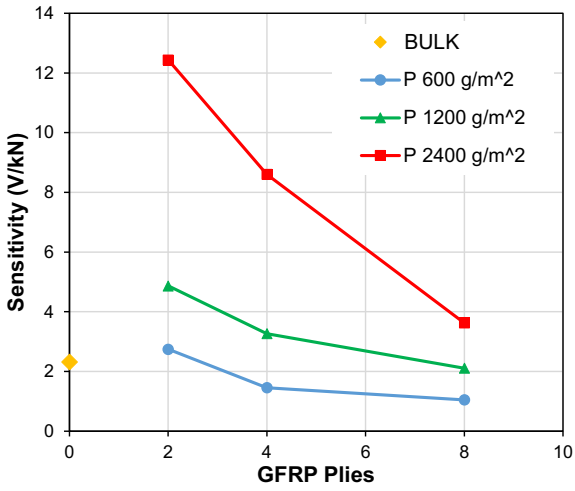

Figure 39: Sensitivity vs number of GFRP plies for pristine sensor (BULK) and powder laminates with different areal density of PZT powder: P 600 g/m^2, P 1200 g/m^2, P 2400 g/m^2.

Knowing the generated piezoelectric voltage as a function of the applied force (sensitivity), it is possible to evaluate the piezoelectric properties of the composite laminate using two different coefficients, according to its applications.

In the case of an actuator, the composite material can be described by the piezoelectric strain d_{33}^{C} (m/V) coefficient, while, for sensing applications, the composite material can be defined by the g_{33}^{C} (Vm/N) piezoelectric voltage coefficient, according to [76], [131].

The superscript C refers to the composite.

Knowing the equivalent circuit parameters of the sensor and the amplifier described in Figure 40 and the voltage generated by the applied force, it is possible to calculate the piezoelectric strain coefficient of the composite laminate d_{33}^{C}.

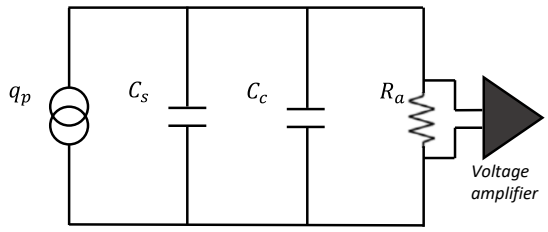

Figure 40: Equivalent circuit of the piezoelectric laminate. The composite laminate can be modeled as a charge generator (q_p) connected in parallel with its resistance and capacitance (R_s and C_s respectively), where R_s is generally high enough to be omitted [132]*. The electrical charges generated by the piezoelectric element are collected by the two electrodes and flow through the cables (C_c) to the amplifier resistance R_a, generating a potential. The measured cables capacitance was equal to 5 pF while the amplifier resistance is 10 GΩ.*

Indeed, for the specific case of a sinusoidal load, according [132] the signal magnitude $|V|$ and phase shift φ for a piezoelectric sensor can be expressed as follow:

$$|V| = \frac{d_{33}^{C} F}{\sqrt{1+\left(\frac{1}{\omega\tau}\right)^{2} C}} \quad \tan\varphi = \frac{1}{\omega\tau} \tag{2}$$

where $\tau = R_a C$ is the time constant.

For high $\omega\tau$ values, as in this case, equation (2) can be simplified as $|V| = F\, d_{33}^{C}/C$ and the d_{33}^{C} value can be simply calculated, while the capacitance values for each composite configuration were measured by prof. Testoni. Generally, it is noticeable a drastic decrease of the composite capacitance as the amount of GFRP plies increase and then when the distance between the electrodes increases, in accordance with the sensitivity trend due to the high dielectric coefficient of the GFRP.

Finally, the g_{33}^{C} coefficient can be calculated as the ratio between the d_{33}^{C} and the dielectric constant of the composite material ($g_{33}^{C} = d_{33}^{C}/\varepsilon_3^{C}$). By measuring the capacitance C, the electrodes surface S and their distance d (reported in **Errore. L'origine riferimento non è stata trovata.**) for each composite laminate, the dielectric constant is derived as $\varepsilon_3^{C} = Cd/S$. This procedure can be replicated for the calculation of the PZT phase piezoelectric coefficients (d_{33}^{P} and g_{33}^{P}). The superscript P refers to the PZT phase in the composite laminate.

The experimental value measured and calculated for each powder laminate configuration were reported in Table 16.

Table 16: Experimental value of sensitivity, capacitance, piezoelectric strain (d_{33}^{C}), dielectric constant (ε_3^{C}) and piezoelectric voltage coefficient (g_{33}^{C}) of the powder laminates. The superscript C refers to composite.

	Sensitivity (mV/N)	Capacitance (ρF 10^{-12})	d_{33}^{C} (m/V10^{12})	ε_3^{C} (F/m10^{-12})	g_{33}^{C} (Vm/N10^{-3})
P2400-G8	3.62	14.5	0.053	73	0.72
P2400-G4	8.60	27.5	0.237	103	2.29
P2400-G2	12.44	44.7	0.556	136	4.07
P1200-G8	2.21	14.4	0.032	65	0.49
P1200-G4	3.35	23.8	0.080	77	1.03
P1200-G2	4.87	44.3	0.216	110	1.96
P600-G8	1.05	16.1	0.017	73	0.23
P600-G4	1.46	24.2	0.035	68	0.52
P600-G2	2.74	45	0.123	92	1.35

Mechanical characterization of PZT composite

The effect of embedding piezoelectric PZT with different morphologies and quantities on the impact resistance of the hosting material was evaluated by low velocity impact and described in detail in section *Low Velocity Impact tests (LVI)*.

In Figure 41 the impact contact force vs displacement responses for the different laminate types are plotted. Moreover, in the bar graph of Figure 42 the relative absorbed energies (integrated area of the force vs displacement curves) are summarized.

As it can be observed in Figure 41a, the curve of the laminate with the embedded pristine sensor (BULK) presents multiple load drops, correlated to the fragile breakages of the ceramic disk. However, the absorbed energy is slightly lower than the reference laminate (REF-G10), because the fragile breakage of the PZT ceramic disk absorbs a low amount of energy. Concerning the PZT powder interleaved laminates, represented in Figure 41b-d, the force vs displacement curves do not show significant load drops linked to fragile breakages. The absorbed energy of the powder laminates is generally slightly higher than the reference one. Likely, the ductile brass electrodes plasticize during impact, especially if positioned outside where the bending stress is higher, causing an increase in the absorbed energy.

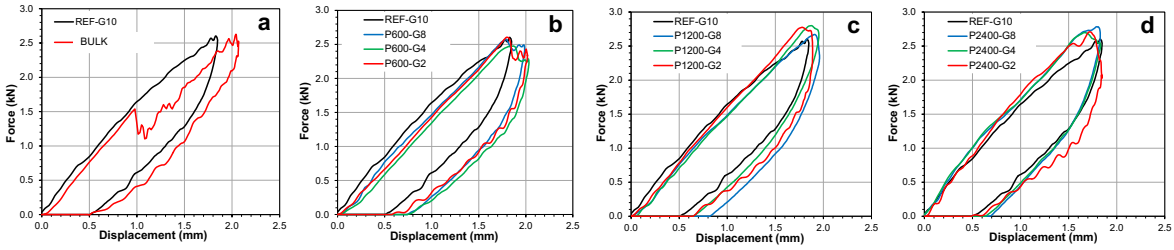

Figure 41: Low velocity impact test at 3 J: impact contact force vs displacement response.

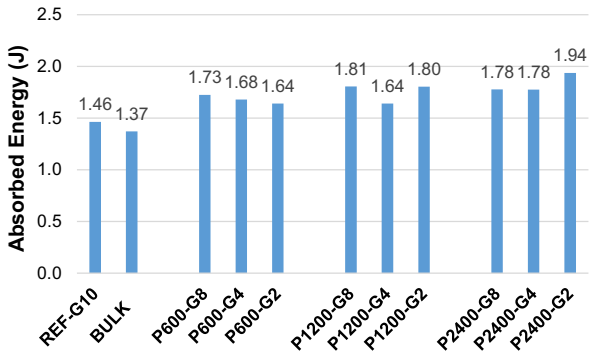

Figure 42: Low velocity impact test at 3 J: absorbed energy.

To directly assess the impact behaviour of the hosting material in the laminates the cross section technique was performed at the impact point. Therefore, after the destructive impact, the cross section was polished and then observed thought to optical microscope in order to investigate the fracture details. Figure 43 shows the cross sections of some impacted laminates chosen to show the correlation between fracture and different configuration. Only half of the micrograph is reported because the damage along the plane is symmetric with respect to the impact axis.

Reference laminate, made of ten GFRP plies, shows a few small 45°-oriented matrix cracks which propagates as negligible delaminations between the GFRP layers at the midplane. Conversely, for the pristine sensor (BULK) embedded in the composite, the lower brass electrode is completely debonded from the PZT disk and the adjacent GFRP ply. Moreover, the PZT disk shows multiple 45°-oriented cracks. Indeed, the bulky and fragile ceramic disk integrated into the laminate cracks and triggers delamination due to the stiffness mismatch between the PZT and GFRP layers.

In the powder laminate P1200-G8 debonding of external electrodes occurs, while this does not happen when the electrodes are interleaved inside the laminate (e.g. P1200-G4 and P1200-G2), where the bending stress is lower. P1200-G8 specimen does not show cracks in correspondence of the midplane where the PZT powder was interleaved, while in the P1200-G4 a 45° crack is slightly visible. By contrast, laminate P1200-G2 presents a remarkable 45° crack propagating in a reverse pine tree pattern induced by the high Hertzian contact stress.

Then the crack continues to propagate as delamination between the GFRP plies. The lower impact resistance of the P1200-G2 laminate can be ascribed to the high amount of PZT powder respect to the epoxy resin of the GFRP prepreg. Indeed, all the specimens with 600 g/m^2 PZT powder does not show matrix crack through the PZT layer (in Figure 43 specimen P600-G4 is shown as a representative example), while all the specimens with 2400 g/m^2 PZT powder show remarkable cracks propagating through the PZT layer (see as example P2400-G4).

Generally, the micrometric powder dispersion does not affect the impact resistance of the hosting composite laminate, while the embedded fragile PZT commercial sensor dramatically triggers the delamination.

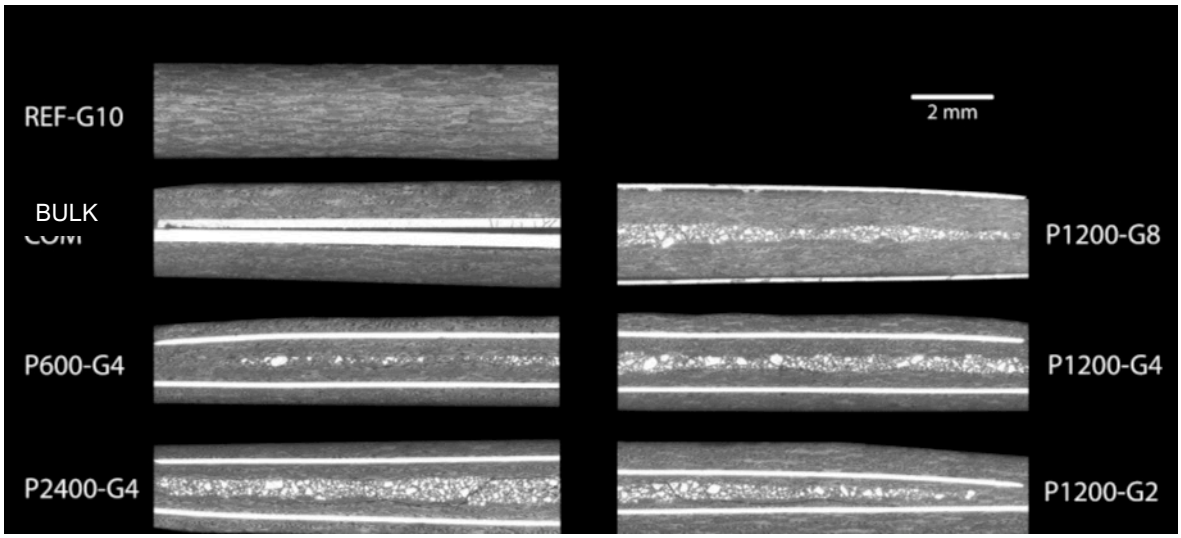

Figure 43: Micrograph analysis of the cross-section most significant laminates at the impact point.

Polarization and piezoelectric model of PZT composite

To understand the piezoelectric behavior of the self-sensing laminate and efficiently design it, it is necessary to consider the electrical and mechanical interactions between the two phases. By observing the cross-section of the self-sensing laminate (micrography of Figure 44a) and neglecting the transversal coupling, the piezoelectric composite can be modelled as a simple one-dimensional series connection of the two phases Figure 44).

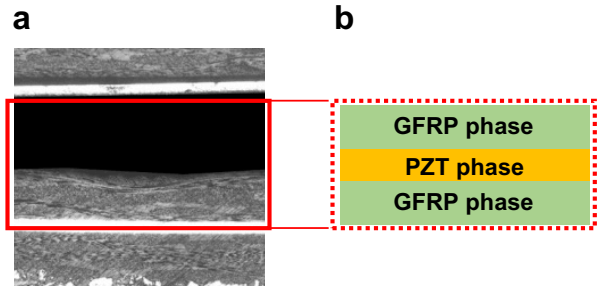

Figure 44: Micrograph (fig. a) and equivalent series model (fig. b) of the self-sensing laminate.

As previously reported, all the manufactured piezoelectric composite laminates were polarized with an electric field of 4 kV/mm. However, unlike bulk PZT materials where the electric field

is applied homogenously, in the case of piezoelectric composite materials the electric field will distribute unevenly between the PZT powder and GFRP phase [133].
Modelling the piezoelectric laminate (Figure 45) as a multi-layered system where the GFRP plies and the PZT layer are connected in series, each phase can be represented as a resistance (R^P, R^G) in parallel with a capacitance (C^P, C^G) [134] was elaborated thanks the collaboration whit PhD student Selleri.

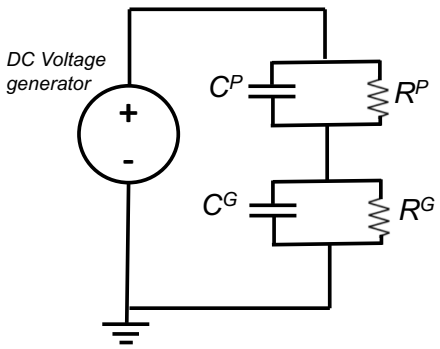

Figure 45: Polarization lumped model of the piezoelectric composite, where the PZT (P subscript) and GFRP (G subscript) phases are modelled as a capacitance and a resistor in parallel.

By applying the Kirchhoff's laws to the equivalent circuit, the effective electric field applied on the piezoelectric phase can be calculated as follow:

$$E_3^P(t) = E_{3_{SS}}^P + (E_{3\_TR}^P - E_{3\_SS}^P)e^{-t/\tau} \tag{3}$$

$$E_{3\_SS}^P = \frac{\frac{E_3^C}{\sigma^P}}{\frac{\nu^P}{\sigma^P}+\frac{1-\nu^P}{\sigma^G}}, \quad E_{3\_TR}^P = \frac{E_3^C\,\varepsilon^G}{\frac{\nu^P}{\varepsilon^G}+\frac{1-\nu^P}{\varepsilon^P}} \tag{4}$$

$$\tau = \tau^G * \tau^P \frac{\frac{1}{\varepsilon^P}+\frac{1-\nu^P}{\nu^P\varepsilon^G}}{\frac{1}{\sigma^P}+\frac{1-\nu^P}{\nu^P\sigma^G}} \tag{5}$$

where:

- E_3^C is the electric field applied to the composite laminate (4 kV/mm);
- $E_{3\_SS}^P$ and $E_{3\_TR}^P$ are the steady state and transient state electric field applied on the PZT phase, respectively;
- ε, σ and ν are the dielectric constant, conductivity and volumetric fraction, respectively;
- τ is the time constant representing the time needed to reach the 63% of the regime value, according to equation 3.

The superscripts$P$, G and C refer to the PZT phases, GFRP phases and composite laminate, respectively.

As shown in the graph of Figure 46, when the DC voltage generator is switched on, a first transient domain distributes the electric field ($E_{3\_TR}^{P}$) on the phases accordingly to their permittivity (ε^{G} and ε^{P}). Then, after a period τ, the steady state is reached and the electric field distribution ($E_{3\_SS}^{P}$) on the two phases is governed by the electrical conductivity (σ^{G} and σ^{P}) of the materials [135].

The electric field value reached in the steady state regime and the transient period τ for the PZT and GFRP composite depends on the volumetric fraction of the two phases (ν^{P}, ν^{G}). In particular, by increasing ν^{P}, the electric field applied on the PZT phase increases and the time constant τ is reduced.

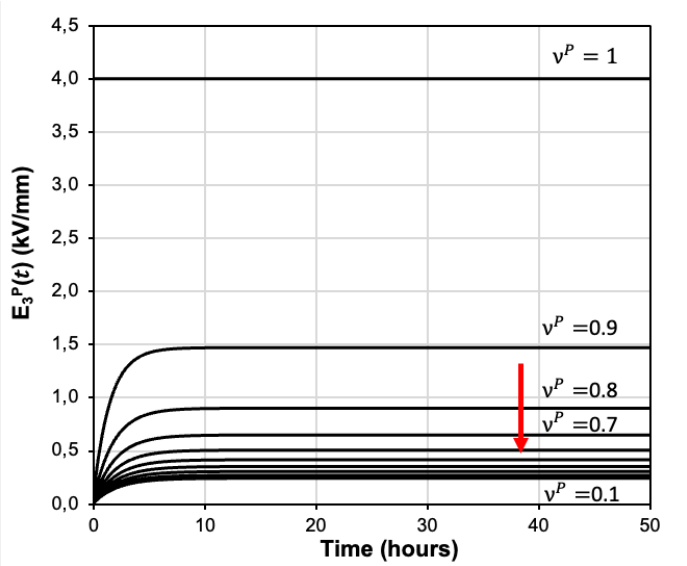

Figure 46 Electric field applied on the PZT phase (E_3^P) of the composite as function of its volumetric fraction (ν^P) and time.

A poling time of 24 hours was chosen in order to reach the steady state regime of the electric field distribution on the PZT phase and therefore equation 3 can be simplified as $E_3^P = E_{3\_SS}^P$, according to the asymptotic behavior observed in the graph of Figure 46. Then the piezoelectric strain coefficient of the PZT phase (d_{33}^P), obtained during polarization of the self-sensing laminate, can be estimated by substituting E_3^P into equation 2. The g_{33}^P can be derived as the ratio of d_{33}^P to ε^P. The so calculated E_3^P and g_{33}^P are reported in Table 17 for each laminate configuration.

After the series connection polarization model developed to estimate the g_{33}^{P} of the piezoelectric phase, which depends on the effective electric field applied on it during the poling process, a series connection piezoelectric model was proposed to estimate the behavior of the laminate as a sensor and an actuator and validated with the previous experimental results.

Indeed, when the piezoelectric composite is mechanically loaded, the electric charges generated by the PZT piezoelectric phase flow towards the electrodes passing through the GFRP plies. The presence of the dielectric GFRP phase influences the piezoelectric response of the self-sensing laminate, as previously observed in the sensitivity graph. Therefore, the piezoelectric behavior of the laminate can be described as a simple one-dimensional series connection model of the two phases that compose the composite laminate. Then, according to [76] and [131], by applying the electric and mechanical boundary conditions to the direct and indirect piezoelectric constitutive equations, the composite piezoelectric strain (d_{33}^{C}) and voltage (g_{33}^{C}) coefficients equations can be obtained for the series connection model:

$$d_{33}^{C} = \frac{\nu^{P} d_{33}^{P} \varepsilon^{G} + \nu^{G} d_{33}^{G} \varepsilon^{P}}{\nu^{P} \varepsilon^{G} + \nu^{G} \varepsilon^{P}} \tag{6}$$

$$g_{33}^{C} = \nu^{P} g_{33}^{P} + \nu^{G} g_{33}^{G} \tag{7}$$

where d_{33}^{P} and d_{33}^{G} are the piezoelectric strain coefficients of the PZT and GFRP phases, while g_{33}^{P} and g_{33}^{G} are the piezoelectric voltage coefficients of the PZT and GFRP phases. Equations 6 and 7 can be simplified considering that the piezoelectric strain and voltage coefficient of the GFRP phases are null.

Therefore, by substituting into equation 6 the piezoelectric strain coefficient of the PZT phase d_{33}^{P} determined according to the polarization model and the dielectric properties of the single phases, it is possible to calculate the piezoelectric strain coefficient of the composite d_{33}^{C}. In the same way, repeating the procedure on equation 7, the piezoelectric voltage coefficient of the composite g_{33}^{C} can be obtained and reported in Table 17.

Table 17: Model value of electric field distribution on the PZT phase (E_3^P), piezoelectric voltage coefficient (g_{33}^P) of the PZT phase and piezoelectric voltage coefficient (g_{33}^C) of the composite laminate. The superscripts P and C refer to PZT phase and composite laminate, respectively.

	E_3^P (kV/mm)	g_{33}^P (Vm/N10^{-3})	g_{33}^C (Vm/N10^{-3})
P2400-G8	0.87	6.9	0.95
P2400-G4	0.96	8.3	2.04
P2400-G2	1.13	11.0	4.31
P1200-G8	0.82	6.1	0.45
P1200-G4	0.87	6.9	0.95
P1200-G2	0.96	8.3	2.04
P600-G8	0.80	5.6	0.22
P600-G4	0.82	6.1	0.45
P600-G2	0.87	6.9	0.95

The so calculated trend of g_{33}^C as a function of the volumetric fraction of the piezoelectric phase (ν^P) is reported in Figure 47 (blue curve) and compared with the experimental data for P600, P1200 and P2400 laminates configurations (blue dots). A parabolic-like trend can be observed for the model which predicts the experimental g_{33}^C values with a coefficient of determination $R^2 = 0.967$.

On the other hand, it can be observed that the piezoelectric strain coefficient of the composite d_{33}^C rapidly decreases for small amounts of the GFRP phase. Indeed, for ν^P= 0.9 the d_{33}^C of the composite drops to 3% of the d_{33}^P value of the pure PZT. The aforementioned remarks suggest that the composite laminate can be properly used for sensing applications with a wide range of PZT volumetric fractions (ν^P), whereas high and unfeasible ν^P values are necessary for actuator applications.

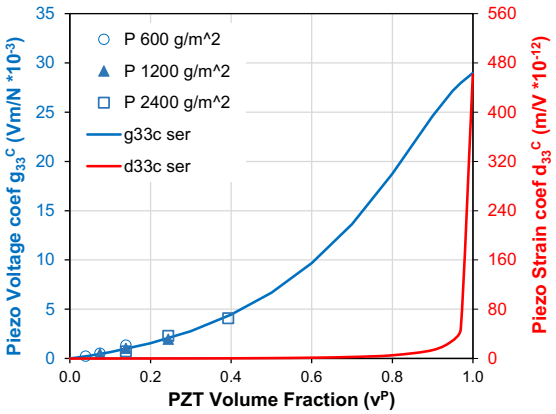

Figure 47: Composite piezoelectric voltage coefficient g_{33}^{C} (blue curve) and strain coefficent d_{33}^{C} (red curve) vs PZT volume fraction v^{P}, estimated by the model. Blue dots represent the g_{33}^{C} experimental data measured for P600, P1200 and P2400 laminates.

The model fit the experimental results with a coefficient of determination of 0.97. The model could be adapted in general for the design of composite piezoelectric smart materials with embedded piezoelectric phases, in terms of different materials (i.e. PVDF) and morphology (i.e. PZT nanofibers).

The best compromise between the impact resistance and the sensitivity is found in the P1200-G4 PZT powder laminate configuration, which shows impact damage comparable to the reference laminate (REF-G10) and a sensitivity 45% higher than the embedded pristine sensor (BULK).

3.2. PVDF-TRFE-based piezoelectric devices

3.2.1. PVDF-TrFE nanofiber

Physico-chemical proprieties of PVDF-TrFE electrospun mat was performed in order to investigate the piezoelectric crystal phase. Indeed, in recent years various techniques have been used to control and enhance the formation of the β-phase in PVDF-based polymers, including the electrospinning process. During this process, both electrical and mechanical effects allow the collection of fibers rich in β-phase content. The strong electrostatic uniaxial stretching introduces elongational forces in the direction of the jet, creating molecular orientation which leads to the transition from α-phase to β-phase, while the porosity of the nanofibrous membrane prevents the delamination risk and increases the impact strength of the composite material when embedded in the hosting matrix.

Physico-chemical characterization of PVdF-TrFE nanofiber

The production of electrospun mat are reported in paragraph *PVdF-TrFE nanofibers.*

The obtained electrospun PVDF-TrFE nanofibrous mat showed randomly oriented, bead-free fibers with average diameter of 420 ± 120 nm (Figure 48 a). The measured thickness of the mat was 100 ± 10 µm (Figure 48 b) its areal weight was 20 g/m^2.

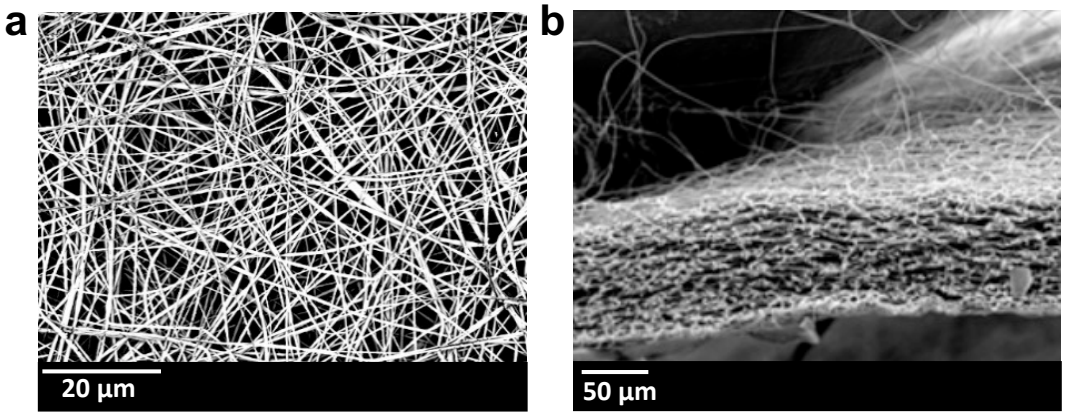

Figure 48: SEM micrographs of electrospun mat of PVDF-TrFE surface a) and cross section b).

In order to investigate the influence of the electrospinning process on the crystalline phase, the nanofibrous mat and powder of PVDF-TrFE were analyzed by DSC and XRD.

DSC is a thermo-analytic technique often used to study the thermal transitions of the polymer. Powder and electrospun mat were analysed from -90 to 250 °C in N_2 atmosphere. Figure 49 shows the DSC first heating curve for the powder and the electrospun mat useful to study the process history of the sample. A broad endothermic peak can be seen, from about 25°C to 160°C, where can be identified three thermal processes associated which each peak. The first endothermic peak represents a pre-melting of few secondary crystals which was attributed to the short head-to-tail sequences or head-to-head and tail-to-tail defects [136]. This occurs around 48 °C and 53 °C for electrospun mat and powder, respectively. The second endothermic peak can be seen such as the Curie transition which is a crystalline phase transition corresponding to the ferroelectric-to-paraelectric phase transition [137]. The F-P transition occurs at 111 °C for the powder while for the electrospun mat, the endothermic peak relating to this transition is centred at 117°C, reflecting better stability of the ferroelectric state acquired through the electrospinning process due to the strong elongation of the polymer/solution jet[138]. Finally, the crystalline phase melts at 143 °C with a ΔH_m of 27.3 J/g and at 140 °C with a ΔH_m of 21.5 J/g for the electrospun mat and the powder, respectively.

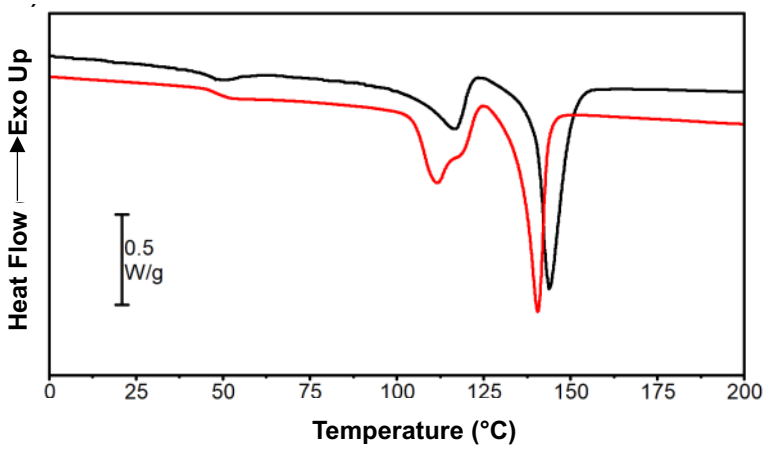

Figure 49:DSC first heating curves (20°C/min) of electrospun PVDF-TrFE mat (black line) and powder (red line).

The crystalline phase of the nanofibrous mat and powder of PVDF-TrFE were analyzed by XRD and the diffractograms of the two samples are shown in Figure 50. A prominent peak at $2\theta = 19.8°$ is observed, representing the (200) Bragg reflections, which is typically assigned to the β crystal phase of PVDF-TrFE, and indicates that the ferroelectric phase is the dominant phase in the copolymer[139] .

A shoulder centered around 18° was evident for the powder sample, attributed to a higher amount of amorphous material in the powder with respect to the nanofibrous mat, as confirmed by the degree of crystallinity, 48% for the powder and 58% for the electrospun fibers. This result indicates that the paraelectric phase of the copolymer is reduced going from powder to electrospun fibers, as indicated by the arrow in Figure 50.

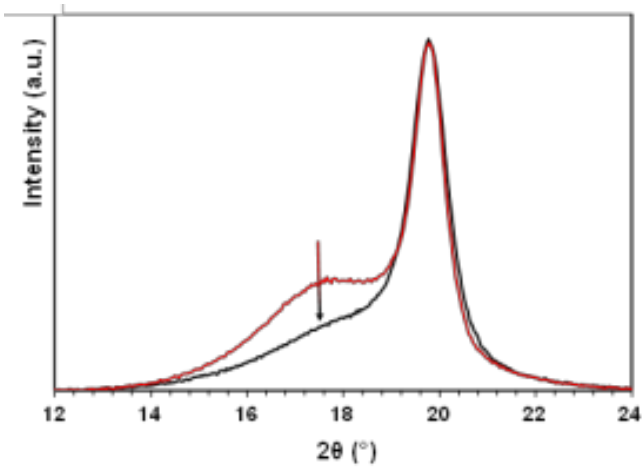

Figure 50: XRD spectra of the electrospun membrane (black line) and powder before electrospinning (red line).

After production of electrospun membrane, to achieve piezoelectric behaviour, the polarization process is required to align the ferroelectric domains of the nanofibers by applying an external electric field [140]. The electric field applied between the electrode on the nanofiber was 25 kV/mm and polarization temperature was set at 130°C (above the T_c) in order to facilitate dipole orientation in the electric field direction. More details information are reported in paragraph *PVdF-TrFE nanofibers*.

The piezoelectric response of the membrane was measured by means of piezometer. The d_{33} value measured was zero before the polarization and 13 pC/N after the process.

3.2.2. PVdF-TrFE nanofibers-based composites

PVDF-TrFE sensor laminate was designed and prepared in collaboration with research group of Prof. Andrea Zucchelli (Department of Industrial Engineering and Prof. Davide Fabiani (Department of Electrical, Electronic, and Information Engineering), University of Bologna. The purpose of this work is to interleave piezoelectric nanofibers of PVdF-TrFE between the plies of a composite laminate in order to create a self-sensing composite material. Thanks to the flexibility of the piezo-nanofibers it is possible to embed them also in curvilinear geometries, such as the sole of the transfemoral prosthesis for MyLeg project.

The self-sensing composite material was developed to detect the ground reaction force in transfemoral prosthetic leg during the gait cycle. The approach to produce a self-sensing laminate based on PVDF-TrFE nanofibers is described in the follow.

Production and characterization of PVDF-TrFE sensor

The first step was to produce, characterize and polarize the PVDF-TrFE membrane, described in the previous paragraph *PVDF-TrFE nanofiber* . Subsequently, the piezoelectric membrane was integrated in a blend of epoxy resin and blocked isocyanate polyurethane prepolymer with the purpose to interleave the piezoelectric sensor in the composite laminate. Moreover, the blend of epoxy resin and polyurethane increases the elasticity of the matrix guaranteeing adaptability also in curvilinear geometries. Also, the electrodes were developed in order to guarantee continuities in the composite laminate and avoid mechanical delamination by dispersing conductive carbon black nanoparticles in the same blend polymer. Furthermore, shield electrodes were added to the piezoelectric sensor with the scope to reduce the signal-to-noise ratio could get worse because of external phenomena, such as triboelectricity effects.

The schematic procedure to fabricate the piezoelectric sensor were illustrated and described in detail in paragraph *PVdF-TrFE electrospun-based composite.*

Integration of PVDF-TrFE sensor in prosthetic foot

With the aim to produce a self-sensing material that is capable to detect also quasi-static loads, proper tuning of the RC value is required, for instance by increasing R_load or C_load, as shown in the circuit of Figure 51. Indeed, a stable sensitivity value (signal voltage/applied force ratio) all over the frequency range will guarantee a linear behavior (signal voltage versus applied force) for a proper sensing mechanism also in case of low frequency loads, such as the Gait cycle. To optimize the RC value of the circuit, before the integration of the sensor in the prosthetic foot, a proof of concept made of a CFRP plate with the same stacking sequence of the prosthetic foot with piezoelectric sensor integrated was developed as shown in Figure 52a.

In particular, the electrical engineering groups of the University di Bologna developed the piezoelectric model, carried out electromechanical characterization and fatigue tests on the piezoelectric CRFP plate. The laminate showed a sensitivity value of 0.14 ± 0.01 mV/N, constant over a wide frequency range (from 0.5 Hz to 20 Hz), making the piezoelectric CRFP plate suitable to work as a self-sensing device for low frequency applications. The measured linearity of the sensor showed coefficient of determination R^2 equal to 0.999. The sensor sensitivity was stable during the whole 10^6 cycles life cycle fatigue test.

The equivalent electric circuit of the self-sensing laminate connected to a voltage amplifier was represented in Figure 51, where the piezoelectric element can be modelled as a charge generator (q_p) connected in parallel to the capacity (C_p) and the resistance (R_p) of the piezoelectric material. The resistances associated to the carbon black-based electrodes are also taken into account in the circuital representation (R_{el}). The resistance R_{load} and the capacity C_{load} are added to adjust the RC constant of the circuit with the aim to properly fit the piezoelectric output with the ground reaction force curve.

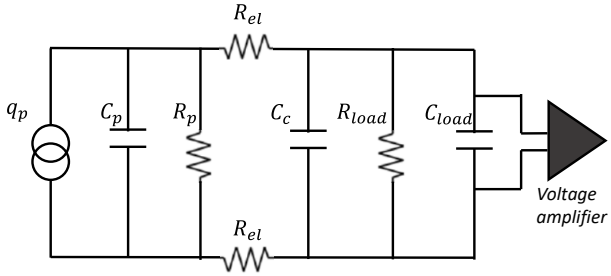

Figure 51: Equivalent circuit of the piezoelectric sensor connected to a voltage amplifier.

Once the self-sensing laminate behaviour was widely investigated on piezoelectric CRFP plate, as a proof of concept the piezoelectric sensor was integrated in the sole of a prosthetic foot realized for Myleg project made of a Carbon Fiber Reinforced Polymer (CFRP) precured laminate.

The piezoelectric sensor was integrated with a Carbon Fiber Reinforced Polymer precured laminate on the sole of the prosthetic foot. A layer of Glass Fiber Reinforced Polymer prepreg was stacked on the CFRP precured laminate. Then the piezoelectric sensor was placed on it and finally covered with another GFRP prepreg. The presence of the GFRP layer below the piezoelectric sensor electrically insulates it from the CFRP conductive base of the prosthetic foot; while the GFRP layer covering the sensor protects it from triboelectric effects and electromechanical noises that would negatively affect the piezoelectric signal. The stacking sequence was shown in Figure 52a.
In particular, two sensors were placed in the toe and one sensor was placed in the heel of the prosthetic foot sole as shown in Figure 52b.

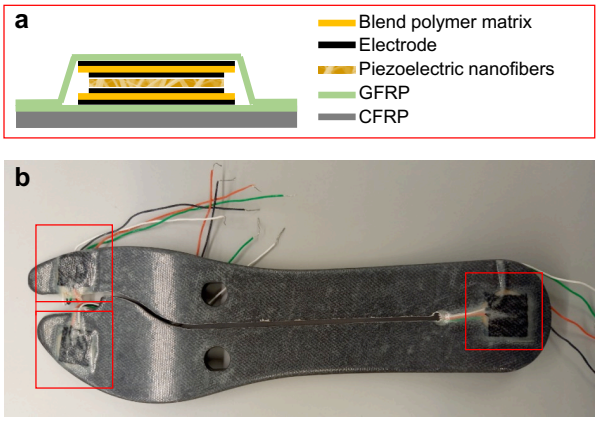

Figure 52: Stacking sequence of the piezoelectric sensor (a) integrated in a prosthetic sole (b).

The result of the integration process of the piezoelectric sensor in the laminate composite material was observed by means of optical micrograph and Scanning Electron Microscopy (SEM) analyses of the cross section. In Figure 53a, the stacking sequence can be observed, with the [$CFRP_1$/$GFRP_1$/sensor/$GFRP_1$] sequence. After polishing, the surface was soaked in an acetone in order to dissolve the PVdF-TrFE nanofibers. In this way, the removed nanofibers can be seen as holes in the SEM cross section magnification of Figure 53b.

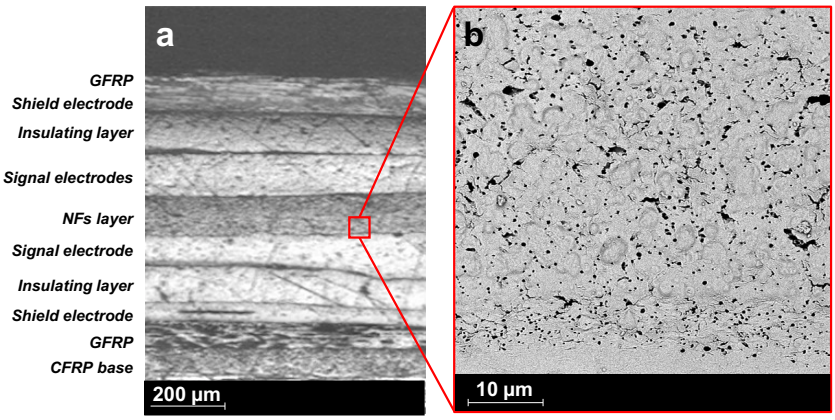

Figure 53: Micrograph image of the cross section of the composite material(a); SEM image of the cross section of the nanofibrous layer after etching in acetone bath (b).

The same circuit configuration (Figure 51) was used to acquire the piezoelectric response. The sole was subsequently connected on the ankle-foot prosthesis as shown in Figure 54a. In order to mimic the Gait cycle period, the compression tests were performed by applying a load on the heel oscillating between 200 N and 800 N at 1 Hz frequency. The piezoelectric signal follows the ground reaction force as shown in Figure 54a, with a sensitivity value of 0.11 mV/N.

As shown in Figure 54b and Figure 54c, addition tests were carried out using the same setup which included putting on the prosthetic foot, the footshell, and subsequently the shoe to simulate everyday clothing. As expected, the piezoelectric signal amplitude is lowered by 75% as a result of the footshell but no additional decreases are recorded when the shoe is added.

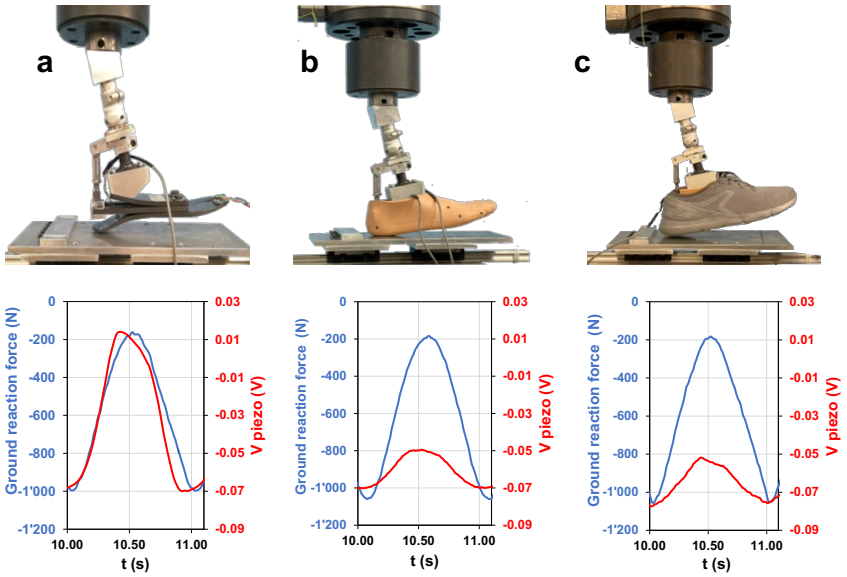

Figure 54: Piezoelectric response of the sensor integrated in the heel of the prosthetic sole (a); with footshell (b) and shoe (c) mounted on it.

In conclusion, the integration of a nanofibrous flexible piezoelectric sensor in a composite laminate material was successfully conducted. To avoid mechanical failure, the nanofibrous mat was implanted in an epoxy resin and polyurethane blend compatible with the resin of the laminate's GFRP. Furthermore, the use of carbon black-based electrodes eliminates any material discontinuities and improves the system's mechanical stability. Even though piezoelectric materials are often employed for dynamic loads, the piezoelectric sensor may correctly detect quasi-static loads by appropriately calibrating the electrical acquisition circuit. Furthermore, the piezoelectric sensor's flexible morphology enables for optimal integration in curved geometries such as a prosthetic foot sole. The piezoelectric response of the sensor inserted in the prosthesis was comparable to that of a sensor embedded in a flat composite laminate, indicating that it might be used in biomedical applications.

3.3. Curled nanofibers for flexible electronics

3.3.1. Curled PLLA nanofibers

In this dissertation PLLA was chosen as polymer to produce crimped nanofiber through the electrospinning process. The PLLA material is usually used in the biomedical application due to the possibility to tune mechanical and biodegradable proprieties by changing the stereoregularity and copolymerization [141]. During the last years, there has been increasing research interest in the biomedical field of this aliphatic polyester, especially in form of nanofiber membranes for their intrinsic proprieties. A systematic study of the effect of different

EtOH treatments on physico-chemical and mechanical properties of the scaffold has been performed [61], [66], [142].

Characterization curled PLLA nanofibers

The preparation of the nanofiber network with controlled curvature was carried out according to the procedure reported in the paragraph *PLLA curled nanofibers*.

PLLA mats were fixed to the dispositive and immersed in EtOH bath in order to lead to a different degree of shrinkage. For this reason, to obtain 0% of degree shrinkage, the PLLA mat was completely bounded and labelled as 'bounded', while to allow return to a conformation in lower energy of the PLLA mat which corresponding to 100% of the degree shrinkage, it is left free, labelled as 'free'. Finally, to obtain the PLLA nanofiber with intermediate curvature between completely crumpled and completely stretched out, it was bounded at 50% and labelled as '50%bounded'.

As mentioned before, PLLA was chosen due to its facility to generate curled nanofibers when it interacts with the plasticizer. In this case, EtOH was used to increase the mobility of the macromolecular chain acting as a plasticizer and decreasing the Tg of the wet polymer. Indeed, the change of the molecular conformation due to chain relaxation occurs when the PLLA mat is placed in an EtOH bath [66].

Therefore, to investigate the effect of EtOH treatment on the PLLA nanofibers, the SEM inspection to evaluate the change of morphology and fiber diameter distributions were carried out and shown in Figure 55.

Specifically, bounded, 50% bounded and free PLLA mats were analysed after EtOH treatment and compared whit pristine PLLA nanofibers. Aligned orientation and bead-free nanofibers were maintained also after EtOH treatment but, as expected, the SEM inspection of the PLLA nanofibers revealed a change of morphology of the nanofibers EtOH treated with respect to the pristine (compare Figure 55a with Figure 55b-d) which depends on the value of the stretching of the PLLA mat into home-made device. In particular, the amplitude of the crimped fibers seems to increase as the degree of shrinkage (calculated with equation 1, reported in the paragraph *PLLA curled nanofibers)* was increased from 0% to 30% and the distribution of the nanofiber diameters slightly increased form 680 ± 160 nm for pristine nanofiber to value about of 820 nm ± 190 for treated PLLA mat. The two morphological modifications in shape and size of nanofibers can be attributed to the electrospinning process and EtOH treatment. It is known, indeed, that during the electrospinning process, the extreme elongation of the polymer jet leads

to the alignment of the macromolecules chain along the nanofiber axis, stretching them and then, the plasticizer effect of EtOH, allows the macromolecular chain to return in random coil conformation [142], obtaining crimped nanofibers with increased diameter.

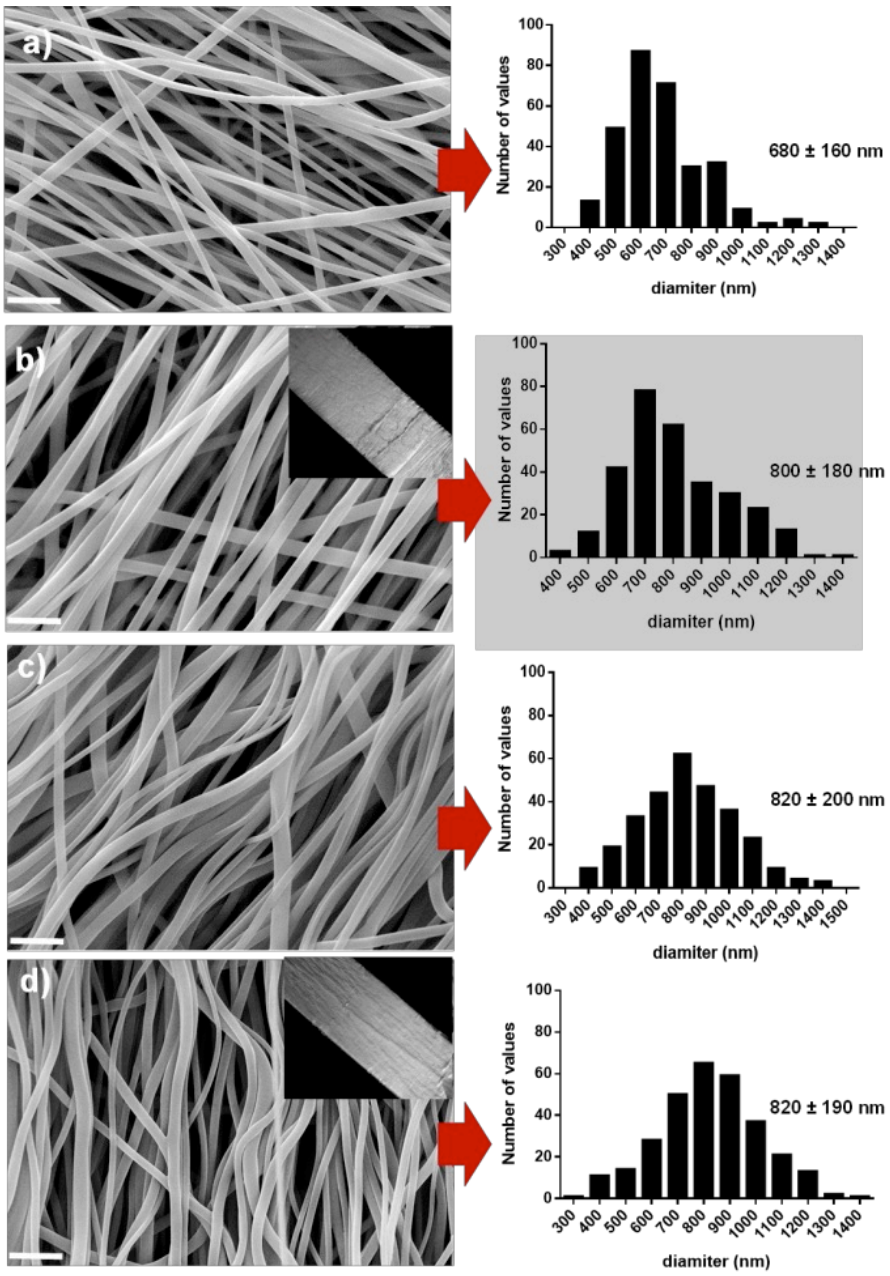

Figure 55: SEM micrograph of nanofibrous PLLA and relative histogram of the fiber diameter distributions (mean value ± standard deviation) of the pristine PLLA (a) and after immersion in EtOH bath for 20 minute at 25°C at different value of constrain: bounded (b), 50% bounded (c), free (d). The inserts show the macroscopically image of the nanofibrous PLLA after EtOH treatment completely bounded (a) and the macroscopically change of the morphology following the EtOH treatment completely free to relax (d). (SEM scale bar 5 µm)

Also the very fast solvent evaporation as well as the mechanical and electrical force during electrospinning process could lead to the formation the oriented amorphous phase but without

the formation of any crystals [143], [144], [145]. While, the permanence of the PLLA mat into EtOH bath could influences the crystalline phase, enlarging polymer crystallization window, leading a mechanical properties change[146].

In order to investigate possible chemical-physical modification, in term of crystalline phase of the PLLA mat, prior and after EtOH treatment was analysed by DSC (Figure 56). DSC curves shows, in all cases, three thermal transitions clearly observable: an endothermic heat flow related to the glass transitions (T_g) around 61 °C, an exothermic peak due to the cold crystallisation (89°C) and an endothermic peak related to the fusion of the crystalline phase (163°C). Enthalpies of both phenomena, crystallization and fusion, is about 38 J/g that, being of the same entity indicates that PLLA mat obtained through the electrospinning process was completely amorphous. Therefore, the only process that affected the crystalline phase was the electrospinning process and not the EtOH treatment, as can be seen comparing DSC curves of pristine and EtOH treat PLLA mat.

A very slight difference between pristine and EtOH treated mat can be found observing the glass transition step in the DSC curve of the polymer. In particular, an endothermic peak superimposed to the heat capacity step of the T_g, due to physical ageing, is more pronounced for the pristine mat than the treated mat where appears as a broad peak with reduced enthalpy relaxation [147].

Thus, the EtOH acting as a plasticizer and enhancing the mobility of the polymer chains forces them to release residual stress due to the electrospinning process, returning to a conformation in lower energy.

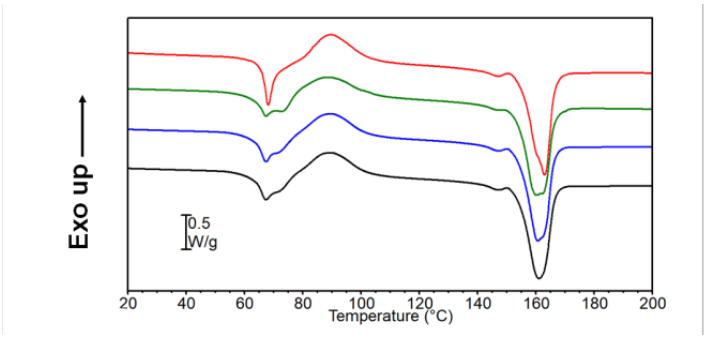

Figure 56: DSC curve of the first heating scan of PLLA nanofibrous before and after EtOH treatment: Pristine (red line), bounded (green line), 50% bounded (blue line) and free (black line).

3.3.2. PLLA curled fibers –based composite

Inspired by tendon tissue, to develop materials able to have a tuneable mechanical response as a function of the applied stress, a composite material based on a PLLA wavy nanofibrous network incorporated in the PDMS elastomeric matrix was chosen. In particular, this work carried out in collaboration with Prof. Tobias Cramer (Physics and Astronomy Department, Università di Bologna), the aims to modify the elastic response by combining the design of the hierarchical structure of nanofibrous network that provides different curvature of the single nanofibers.

Production and mechanical characterization of curled nanofiber composite

The preparation of the composite materials was carried out according to procedure reported in the paragraph *Curled nanofiber-based composite*. To produce three types of stretchable specimens, treated nanofibrous networks (bounded, 50% bounded and free PLLA mat) were embedded into PDMS elastomeric matrix on glass support. In addition, PDMS pristine was produced as a reference. To make easier to detach the composite material from the slide and avoiding fibers stretch, a thin layer of water-soluble polymer was previously deposited on the glass support. The PLLA mats were placed on covered glass support, PDMS was poured on it and the spin-coating process was carry out to obtain a uniform PDMS layer removing any excess. After the composite cure, it was detached from glass support solubilizing the water polymer.

However, to understand the relationship between the mechanical properties and geometry of electrospun fibers, measurement of the mechanical properties of single fibers is a vital need.
To investigate the mechanical properties at the nano and micro scale, AFM nanoindentation is the most suitable technique, as it allows a point-precise analysis of the mechanical properties of the sample together with a topography mapping of the area of interest.
To perform AFM measurements on single fiber, few fibers were collected on ITO covered glasses, on the conductive side. ITO was chosen to mimic the conductive surface of the ground collector during the electrospinning process. The nanofiber appears to be bound on the substrate surface therefore any treatment with EtOH would be effective as the nanofiber is not free to shrink. For this reason, AFM measurements were performed on pristine PLLA nanofibers. Through AFM built-in microscope, the fibers disposition in the glass can be investigated and the indentation region aimed.

Non-contact mode AFM technique is employed to map the topography of the fiber. This operation mode allows to map the surface without effectively touching it so without compromise the original fiber status. The nanofiber image in Figure 57: a shows the regular fiber shape resulting 423nm high, while the diameter is around one micron, confirming the half cylindrical shape. The surface appears smooth and free from undesired foreign particles that could compromise the following indentation experiments. So, from the topographic image of the fiber, in Figure 57: b, four indentation points with step indentation distances around 3nm, were highlighted on the surface of the 3D reconstruction of the AFM scan image. To investigate the mechanical properties performing the indentation experiment, the AFM was set in contact mode. For each point, the force-indentation curves present a similar behaviour. The elastic moduli differ of a few units remaining in the same order of magnitude. For what concerns the composite properties, the AFM image of the surface (Figure 57: c), as expected, does not show significant structures. The surface mapping shows a uniform surface with a height spread of a few nanometers, which wipes out any possibility to individuate the fiber mat incorporated in PDMS matrix. The force-indentation curves on composite, Figure 57: d, present a quasi-linear behaviour of the force response to the indentation. The tip indented the sample of 400nm and the behaviour of the composite does not move away from the reference PDMS.

However, although AFM indentation is an excellent technique for investigating the mechanical properties for the individual fibers at the nanoscale, investigating the bulk material is still difficult.

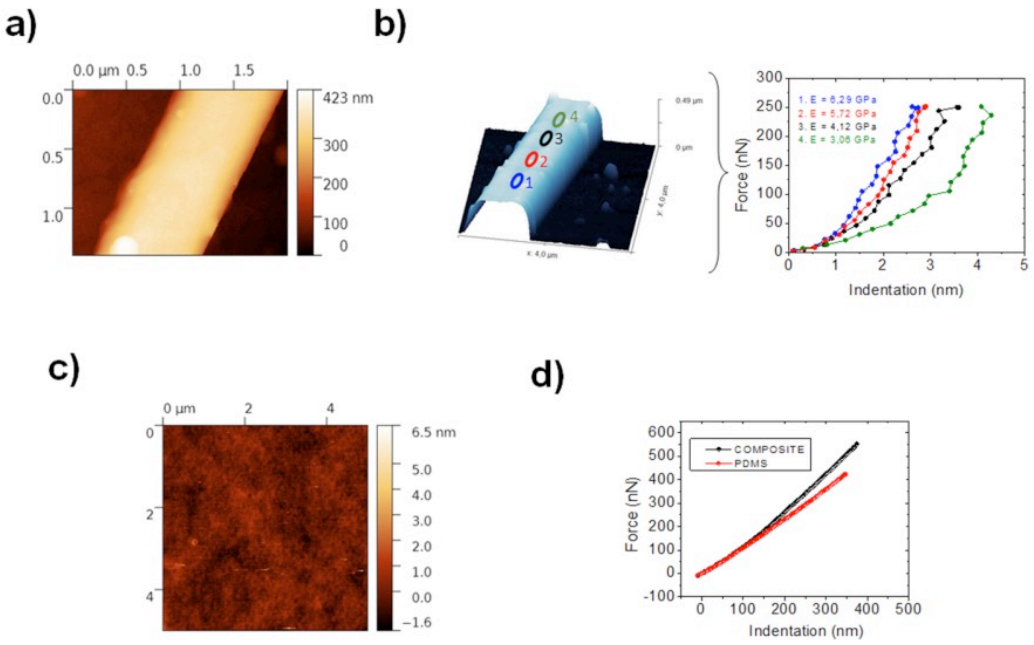

Figure 57: Micrometric estimation of mechanical properties via AFM nanoindentation on single nanofiber and composite material. a) AFM topographic image of single fiber; b) Nanoindentation on four points on the fiber surface, the colour of the points corresponds to the colour of the data. Elastic moduli E are reported as label. c) AFM Topographic image of the composite. d) comparison of nanoindentation on pure PDMS sample and composite material.

The tensile properties of 3D samples were measured by a conventional Dynamic Mechanical Analyser (DMA). The sample was cut into a specific dimension and mounted between two holders at a fixed distance. As described in *Dynamic Mechanical Analyser (DMA),* Stress-Strain cycles and Multi-strain tests were performed on both pristine PDMS sample and composite material to investigate the impact of the embedded nanofiber network on the elastic properties of the elastomeric matrix. Moreover, the effect of the three different network geometry (free, 50% bonded and bonded) on the mechanical properties of the composite material is studied to achieve a tuneable stiffening of the structure. From multi-strain tests, the ratio between the elastic component and the viscous losses in the three different cases is extracted to achieve a more detailed comparison. From stress-strain cycles, the differences in elastic modulus and, more generally, in the elastomeric behaviour from the pristine PDMS sample of the composites is highlighted. Figure 58a shows the stress response of PDMS in the stress-strain test performed with the DMA. The test involved a strain value up to 40 % to ensure the linear elastomeric behaviour and the possibility to relate its mechanical properties to the literature study, but here the zoom up to the 5% is considered to better compare it to the tests made on the composite material. As most elastomeric materials, the relation is quasi-linear and the elastic modulus,

given by the ratio between stress and strain, resulted 4MPa. As the straight PLLA fibers are inserted in the matrix, they provide an evident change in the stress response, as it is shown in Figure 58b. As the elastic modulus is greatly increased, no elongation greater than the 5% is allows, as the composite material sample breaks. As this became evident in prior experiments, stress-strain cycles have been decided to be performed within the 5% of strain to better compare the different nanofiber network geometry composites. Figure 58c depicts the stress response of the composite material with the completely shrunk fibers embedded. It shows a stiffening of the structure at the end of the cycle, from the 3% of strain, that prevents the material from undesired overstretching but maintaining the elastic capabilities of the elastomeric matrix. By comparing Figure 58b) and c), it is evident the higher impact on the elastic properties and on the stiffening of the structure of the matrix in the composite made with straight fibers. In this case, no elongation is allowed with an immediate high stress response. In the curved fiber case, a first elongation is achieved and then the stiffening behaviour acts. Both the cases differ consistently from the linear response of the pristine PDMS sample.

Figure 58d) and e) show the results of the multi-strain tests. In each figure is presented the comparison between the pristine PDMS sample and the composite material with embedded the three different nanofiber network geometry, the bonded, 50% bonded and free, i.e. completely straight, half curved and completely curved fibers. Figure 58d shows how increasing the straightness of the fibers, and so the hardness of the composite material bulk structure, more energy is needed to make the composite to oscillate at that given preload force. PDMS exhibits the lower storage modulus value while the straight fibers present a value two order of magnitude greater. As the curvature increases (50% bonded and then free) the storage modulus diminishes as can be expected. For what concern the loss modulus, no evident differences are shown between the half-curved and the completely curved fibers, meaning that no different changes in the composite structure is caused. On the other hand, from the elastomeric behaviour of the PDMS in which the loss modulus is around 0 MPa, to the straight fibers composite, the difference of almost 2.4 MPa of loss modulus indicates a high deformation of the original structure in the latter, mainly caused by plastic detaching of the fibers and the matrix. It is optically appreciable by a changing in the colour of the composite material, previous almost transparent and then white opaque after the multi-strain experiments.

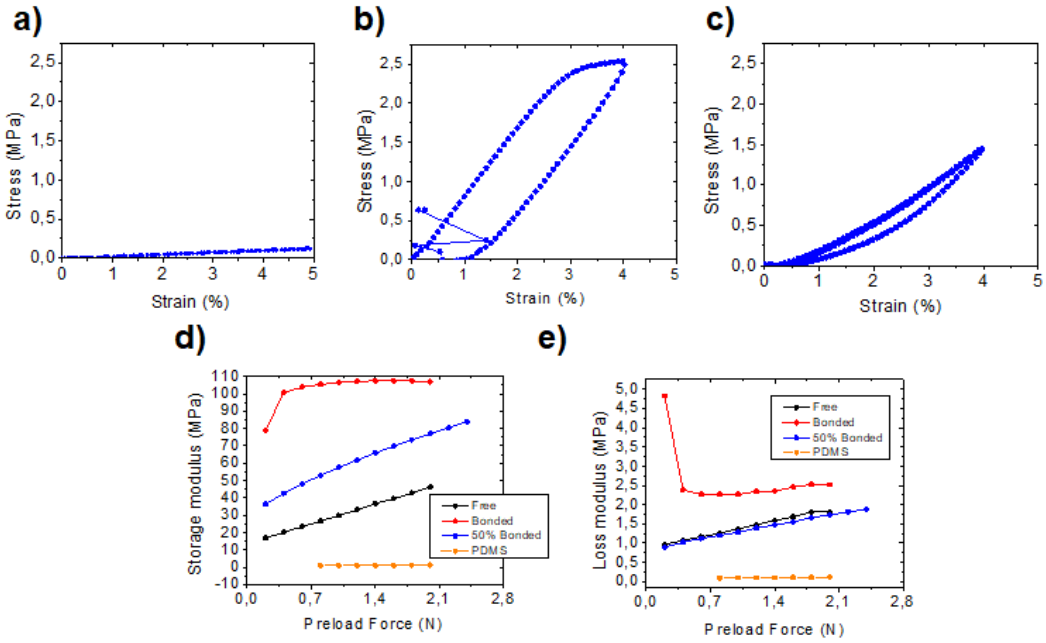

Figure 58: DMA stress-strain curves of a) PDMS, b) bonded and c) free composite material. DMA strain cycles procedure to obtain d) storage modulus and e) loss modulus of the specimens.

All the DMA tests performed highlighted the different mechanical response to the deformation by inserting the nanofiber network in the elastomeric matrix. The different curvature of the fibers shows a remarkably different generation and tuning capability of the stress response.

4. Conclusions

The present PhD project focused on the design, fabrication and characterization of nanostructured smart materials embedded into a polymeric matric to obtain a composite material that can be used as a functional component for medical devices. In particular, it has been demonstrated that composite materials based on piezoelectric components, both ceramic and polymeric, can be used as pressure sensors. Both devices could be used for vibrational energy harvesting from human movement to improve longer battery lives of current implantable and wearable medical devices, solving one of the biggest challenges in the field of wearable medical devices.

In particular, the research carried out on PZT powder-based composites leads the foundations for understanding the piezoelectric behaviour and defining design guidelines for the manufacture of such composite sensors through the series connection proposed in the model.

The effect of the PZT powder volume fraction on the electromechanical properties was experimentally investigated and the results were compared also with a piezoelectric laminate made with a PZT pristine sensor in bulk. Concerning the mechanical performance, the micrometric powder dispersion does not affect the impact resistance of the hosting composite laminate, while the embedded fragile PZT in bulk dramatically triggers the delamination.

The study of the mechanical properties made it possible to understand the volume fraction of PZT to be incorporated in the composite material to ensure good mechanical properties. A model was developed to define the design guidelines for the fabrication of intelligent composite piezoelectric materials with embedded piezoelectric phases, in terms of different materials and morphology.

Therefore, future developments will concern the realization of intelligent composite piezoelectric laminated materials through the use of the PZT electrospun nanofibers using the volumetric fraction parameters identified in order to evaluate the change in electromechanical performance between the various morphologies (powder and nanofiber made of the same PZT).

The PVDF-TrFE nanofiber-based composites represent a good alternative to create a self-sensing composite material by embedding in a flexible matrix piezoelectric nanofibers and carbon black nanoparticles, which act as electrodes. The sensor thus designed can be used for various applications that require a flexible device. Furthermore, the integration of this sensor in the sole of the prosthetic foot does not compromise its functionality as demonstrated in this Thesis.

Another related problem in medical devices has been found in flexible medical devices which have a mechanical discrepancy between rigid electronic materials/soft human tissues/different

materials that constitute electronic devices. The PLLA curled nanofibers-based composite can be a promising solution to avoid the local concentration of the stress which could lead to failure of the electronic device. This is possible thanks to the incorporated network of PLLA nanostructure, which tune the stress-strain response to the deformation by avoiding excessive deformation of the elastomeric matrix.

In conclusion, the field of medical devices is in great expansion and thanks to the collaboration between various specialized sectors it will be possible to solve the challenges still unsatisfied today. This Thesis work represents an example of collaboration between different areas of expertise, aimed at designing and developing functional components for medical devices using composite materials and nanostructured intelligent materials.

5. References

[1] H. C. Koydemir *et al.* "Wearable and Implantable Sensors for Biomedical Applications," *Annu. Rev. Anal. Chem.*, vol. 11, pp. 127–146, 2018, doi: 10.1146/annurev-anchem-061417-125956.

[2] L. Dong *et al.*, "Cardiac energy harvesting and sensing based on piezoelectric and triboelectric designs," *Nano Energy*, vol. 76, no. May, p. 105076, 2020, doi: 10.1016/j.nanoen.2020.105076.

[3] P. Dario *et al.* "Micro-systems in biomedical applications," 2000.

[4] M. Gong *et al.* "Polymer nanocomposite meshes for flexible electronic devices," *Prog. Polym. Sci.*, vol. 107, p. 101279, 2020, doi: 10.1016/j.progpolymsci.2020.101279.

[5] J. Han *et al.* "Bio-functional electrospun nanomaterials: From topology design to biological applications," *Prog. Polym. Sci.*, vol. 91, pp. 1–28, 2019, doi: 10.1016/j.progpolymsci.2019.02.006.

[6] F. Arab Hassani *et al.*, "Smart materials for smart healthcare– moving from sensors and actuators to self-sustained nanoenergy nanosystems," *Smart Mater. Med.*, vol. 1, no. July, pp. 92–124, 2020, doi: 10.1016/j.smaim.2020.07.005.

[7] M. De Santis *et al.* "Wireless implantable and biodegradable sensors for postsurgery monitoring: Current status and future perspectives," *Nanotechnology*, vol. 31, no. 25, 2020, doi: 10.1088/1361-6528/ab7a2d.

[8] M. Ha *et al.* "Wearable and flexible sensors for user-interactive health-monitoring devices," *J. Mater. Chem. B*, vol. 6, pp. 4043–4064, 2018, doi: 10.1039/c8tb01063c.

[9] A. Gloria *et al.*, "Technical features and criteria in designing fiber-reinforced composite materials : from the aerospace and aeronautical field to biomedical applications," *J. Biomater. Biomechan*, vol. 9, no. 2, pp. 151–163, 2011, doi: 10.5301/JABB.2011.8569.

[10] S. Das Mahapatra *et al.*, "Piezoelectric Materials for Energy Harvesting and Sensing Applications: Roadmap for Future Smart Materials," *Adv. Sci.*, vol. 8, no. 17, 2021, doi: 10.1002/advs.202100864.

[11] G. W. Comanor *et al.* "Nanocomposites: a brief review," *Compet. Policy Eur. North Am.*, pp. 55–57, 2020, doi: 10.4324/9781315014661-16.

[12] W. S. Chow *et al.* "Smart polymer nanocomposites: A review," *Express Polym. Lett.*, vol. 14, no. 5, pp. 416–435, 2020, doi: 10.3144/expresspolymlett.2020.35.

[13] S. Municoy *et al.*, "Stimuli-responsive materials for tissue engineering and drug delivery," *Int. J. Mol. Sci.*, vol. 21, no. 13, pp. 1–39, 2020, doi: 10.3390/ijms21134724.

[14] L. Dong *et al.* "Vibration-Energy-Harvesting System: Transduction Mechanisms,

Frequency Tuning Techniques, and Biomechanical Applications," *Adv. Mater. Technol.*, vol. 4, no. 1900177, pp. 1–28, 2019, doi: 10.1002/admt.201900177.

[15] R. Sheybani *et al.* "Insight : implantable medical devices," *Lab Chip*, vol. 14, pp. 3233–3240, 2014, doi: 10.1039/c4lc00127c.

[16] L. Wang *et al.* "Wearable, Implantable, and Interventional Medical Devices Based on Smart Electronic Skins," *Adv. Mater. Technol.*, vol. 6, no. 6, pp. 1–18, 2021, doi: 10.1002/admt.202100107.

[17] X. Wang *et al.* "Flexible Sensing Electronics for Wearable/Attachable Health Monitoring," *Small*, vol. 13, no. 25, pp. 1–19, 2017, doi: 10.1002/smll.201602790.

[18] L. Medeiros *et al.*, "Sensors and Systems for Physical Rehabilitation and Health Monitoring — A Review," *Sensors (Switzerland)*, vol. 20, no. 4063, 2020.

[19] Y. Zang *et al.* "Advances of flexible pressure sensors toward artificial intelligence and health care applications," *Mater. Horizons*, vol. 2, no. 2, pp. 140–156, 2015, doi: 10.1039/c4mh00147h.

[20] S. Y Chen *et al.* "Temperature–Time Texture Transition of Pb(Zr1−xTix)O3 Thin Films: II, Heat Treatment and Compositional Effects," *J. Am. Ceram. Soc.*, vol. 77, no. 9, pp. 2337–2344, 1994, doi: 10.1111/j.1151-2916.1994.tb04603.x.

[21] B. Llerena Zambrano *et al.*, "Soft Electronics Based on Stretchable and Conductive Nanocomposites for Biomedical Applications," *Adv. Healthc. Mater.*, vol. 10, no. 3, pp. 1–24, 2021, doi: 10.1002/adhm.202001397.

[22] Z. Luo *et al.*, "Structure-property relationships in graphene-based strain and pressure sensors for potential artificial intelligence applications," *Sensors (Switzerland)*, vol. 19, no. 5, pp. 1–27, 2019, doi: 10.3390/s19051250.

[23] J. Qiu *et al.*, "Rapid-Response, Low Detection Limit, and High-Sensitivity Capacitive Flexible Tactile Sensor Based on Three-Dimensional Porous Dielectric Layer for Wearable Electronic Skin," *ACS Appl. Mater. Interfaces*, vol. 11, no. 43, pp. 40716–40725, 2019, doi: 10.1021/acsami.9b16511.

[24] B. Herren *et al.* "PDMS sponges with embedded carbon nanotubes as piezoresistive sensors for human motion detection," *Nanomaterials*, vol. 11, no. 7, 2021, doi: 10.3390/nano11071740.

[25] J. C. Yeo *et al.* "Emerging flexible and wearable physical sensing platforms for healthcare and biomedical applications," *Microsystems Nanoeng.*, vol. 2, p. 16043, 2016, doi: 10.1038/micronano.2016.43.

[26] L. Dong *et al.*, "In vivo cardiac power generation enabled by an integrated helical piezoelectric pacemaker lead," *Nano Energy*, vol. 66, no. August, p. 104085, 2019, doi: 10.1016/j.nanoen.2019.104085.

[27] Y. Jung *et al.*, "A highly sensitive and flexible capacitive pressure sensor based on a porous three-dimensional PDMS/microsphere composite," *Polymers (Basel).*, vol. 12, no. 6, pp. 0–10, 2020, doi: 10.3390/polym12061412.

[28] Z. Zheng *et al.* "Dielectric Modulated Glass Fiber Fabric-Based Single Electrode Triboelectric Nanogenerator for Efficient Biomechanical Energy Harvesting," *Adv. Funct. Mater.*, vol. 31, no. 32, 2021, doi: 10.1002/adfm.202102431.

[29] M. Xie *et al.*, "Flexible Multifunctional Sensors for Wearable and Robotic Applications," *Adv. Mater. Technol.*, vol. 4, no. 3, pp. 1–29, 2019, doi: 10.1002/admt.201800626.

[30] M. Saeedifar *et al.* "Using passive and active acoustic methods for impact damage assessment of composite structures," *Compos. Struct.*, vol. 226, no. July, p. 111252, 2019, doi: 10.1016/j.compstruct.2019.111252.

[31] J. Jiang *et al.* "Detecting debonding between steel beam and reinforcing CFRP plate using active sensing with removable PZT-based transducers," *Sensors (Switzerland)*, vol. 20, no. 1, 2020, doi: 10.3390/s20010041.

[32] B. Yang *et al.*, "Damage Localization in Composite Laminates by Building in PZT Wafer Transducers: A Comparative Study with Surface-Bonded PZT Strategy," *Adv. Eng. Mater.*, vol. 21, no. 3, pp. 1–12, 2019, doi: 10.1002/adem.201801040.

[33] S. Butler *et al.*, "Effect of embedded sensors on interlaminar damage in composite structures," *J. Intell. Mater. Syst. Struct.*, vol. 22, no. 16, pp. 1857–1868, 2011, doi: 10.1177/1045389X11414225.

[34] Y. Xin *et al.*, "Wearable and unconstrained systems based on PVDF sensors in physiological signals monitoring: A brief review," *Ferroelectrics*, vol. 500, no. 1, pp. 291–300, 2016, doi: 10.1080/00150193.2016.1230440.

[35] G. Roopa Manjunatha *et al.* "Polyvinylidene fluoride film based nasal sensor to monitor human respiration pattern: An initial clinical study," *J. Clin. Monit. Comput.*, vol. 27, no. 6, pp. 647–657, 2013, doi: 10.1007/s10877-013-9486-x.

[36] S. Choi a *et al.* "A novel wearable sensor device with conductive fabric and PVDF film for monitoring cardiorespiratory signals," *Sensors Actuators, A Phys.*, vol. 128, no. 2, pp. 317–326, 2006, doi: 10.1016/j.sna.2006.02.012.

[37] A. Cranny *et al.* "Thick-film force and slip sensors for a prosthetic hand," *Sensors*

Actuators, A Phys., vol. 123–124, pp. 162–171, 2005, doi: 10.1016/j.sna.2005.02.015.

[38] J. Di *et al.*, "Stretch-Triggered Drug Delivery from Wearable Elastomer Films Containing Therapeutic Depots," *ACS Nano*, vol. 9, no. 9, pp. 9407–9415, 2015, doi: 10.1021/acsnano.5b03975.

[39] C. Xu Y *et al.* "Portable and wearable self-powered systems based on emerging energy harvesting technology," *Microsystems Nanoeng.*, vol. 7, no. 1, 2021, doi: 10.1038/s41378-021-00248-z.

[40] H. Ryu , *et al.* "Hybrid Energy Harvesters: Toward Sustainable Energy Harvesting," *Adv. Mater.*, vol. 31, no. 34, pp. 1–19, 2019, doi: 10.1002/adma.201802898.

[41] T. A. Arica , *et al.* "Advances in Electrospun Fiber-Based Flexible Nanogenerators for Wearable Applications," *Macromol. Mater. Eng.*, vol. 306, no. 8, 2021, doi: 10.1002/mame.202100143.

[42] F. R. Fan , *et al.* "Flexible Nanogenerators for Energy Harvesting and Self-Powered Electronics," *Adv. Mater.*, vol. 28, no. 22, pp. 4283–4305, 2016, doi: 10.1002/adma.201504299.

[43] X. S. Zhang *et al.* "High performance triboelectric nanogenerators based on large-scale mass-fabrication technologies," *Nano Energy*, vol. 11, pp. 304–322, 2015, doi: 10.1016/j.nanoen.2014.11.012.

[44] D. Jiang , *et al.* "Emerging Implantable Energy Harvesters and Self-Powered Implantable Medical Electronics," *ACS Nano*, vol. 14, no. 6, pp. 6436–6448, 2020, doi: 10.1021/acsnano.9b08268.

[45] B. Lu *et al.*, "Ultra-flexible Piezoelectric Devices Integrated with Heart to Harvest the Biomechanical Energy," *Sci. Rep.*, vol. 5, pp. 1–9, 2015, doi: 10.1038/srep16065.

[46] J. Chen *et al.* "Reviving Vibration Energy Harvesting and Self-Powered Sensing by a Triboelectric Nanogenerator," *Joule*, vol. 1, no. 3, pp. 480–521, 2017, doi: 10.1016/j.joule.2017.09.004.

[47] T. Li *et al.*, "Lightweight Triboelectric Nanogenerator for Energy Harvesting and Sensing Tiny Mechanical Motion," *Adv. Funct. Mater.*, vol. 26, no. 24, pp. 4370–4376, 2016, doi: 10.1002/adfm.201600279.

[48] Z. Yang *et al.*, "Recent Advances in Self-Powered Piezoelectric and Triboelectric Sensors : From Material and Structure Design to Frontier Applications of Artificial Intelligence," 2021.

[49] M. S. Sorayani Bafqi , *et al.* "Fabrication of composite PVDF-ZnO nanofiber mats by

electrospinning for energy scavenging application with enhanced efficiency," *J. Polym. Res.*, vol. 22, no. 7, pp. 1–9, 2015, doi: 10.1007/s10965-015-0765-8.

[50] C. K. Jeong *et al.* "Lead-Free Perovskite Nanowire-Employed Piezopolymer for Highly Efficient Flexible Nanocomposite Energy Harvester," *Small*, vol. 14, no. 19, pp. 1–8, 2018, doi: 10.1002/smll.201704022.

[51] X. Chen *et al.* "PVDF-Based Ferroelectric Polymers in Modern Flexible Electronics," *Adv. Electron. Mater.*, vol. 3, no. 5, 2017, doi: 10.1002/aelm.201600460.

[52] Y. Qi *et al.* "Piezoelectric ribbons printed onto rubber for flexible energy conversion," *Nano Lett.*, vol. 10, no. 2, pp. 524–525, 2010, doi: 10.1021/nl903377u.

[53] J. Kwon , *et al.* "A high performance PZT ribbon-based nanogenerator using graphene transparent electrodes," *Energy Environ. Sci.*, vol. 5, no. 10, pp. 8970–8975, 2012, doi: 10.1039/c2ee22251e.

[54] X. Chen *et al.* "1.6 v nanogenerator for mechanical energy harvesting using PZT nanofibers," *Nano Lett.*, vol. 10, no. 6, pp. 2133–2137, 2010, doi: 10.1021/nl100812k.

[55] H. J. Tseng, *et al.* "Flexible PZT thin film tactile sensor for biomedical monitoring," *Sensors (Switzerland)*, vol. 13, no. 5, pp. 5478–5492, 2013, doi: 10.3390/s130505478.

[56] R. Libanori, *et al.* "Stretchable heterogeneous composites with extreme mechanical gradients," *Nat. Commun.*, vol. 3:1265, pp. 1–10, 2012, doi: 10.1038/ncomms2281.

[57] Y. Gao, *et al.* "Flexible Hybrid Sensors for Health Monitoring : Materials and Mechanisms to Render Wearability," *Adv. Mater.*, vol. 32, no. 1902133, pp. 1–31, 2020, doi: 10.1002/adma.201902133.

[58] W. E. Teo a *et al.* "A review on electrospinning design and nanofibre assemblies," *Nanotechnology*, vol. 17, no. 14, 2006, doi: 10.1088/0957-4484/17/14/R01.

[59] T. U. Rashid *et al.* "Mechanical Properties of Electrospun Fibers — A Critical Review," *Adv. Eng. Mater.*, vol. 23, no. 2100153, pp. 1–26, 2021, doi: 10.1002/adem.202100153.

[60] H. Matsumoto *et al.* "Functionality in Electrospun Nanofibrous Membranes Based on Fiber's Size, Surface Area, and Molecular Orientation," *Membranes (Basel).*, vol. 1, pp. 249–264, 2011, doi: 10.3390/membranes1030249.

[61] W. Liu *et al.*, "Generation of Electrospun Nanofi bers with Controllable Degrees of Crimping Through a Simple , Plasticizer-Based Treatment," *Adv. Mater.*, vol. 27, no. 16, pp. 2583–2588, 2015, doi: 10.1002/adma.201500329.

[62] T. Lin *et al.* "Self-crimping bicomponent nanofibers electrospun from polyacrylonitrile and elastomeric polyurethane," *Adv. Mater.*, vol. 17, no. 22, pp. 2699–2703, 2005, doi: 10.1002/adma.200500901.

[63] R. Kessick , *et al.* “Microscale polymeric helical structures produced by electrospinning Microscale polymeric helical structures produced by electrospinning,” *Appl. Phys. Lett.*, vol. 4807, pp. 21–24, 2006, doi: 10.1063/1.1762704.

[64] D. C. Surrao , *et al.* “Self-Crimping , Biodegradable , Electrospun Polymer Microfibers,” *Biomacromolecules*, vol. 11, pp. 3624–3629, 2010.

[65] A. C. Trindade , *et al.* “First curl, then wrinkle,” *Macromol. Rapid Commun.*, vol. 34, no. 20, pp. 1618–1622, 2013, doi: 10.1002/marc.201300436.

[66] C. Gualandi *et al.*, “Ethanol disinfection affects physical properties and cell response of electrospun poly (L -lactic acid) scaffolds,” *Eur. Polym. J.*, vol. 48, no. 12, pp. 2008–2018, 2018, doi: 10.1016/j.eurpolymj.2012.09.016.

[67] P. Fratzl a *et al.* “Nature ’ s hierarchical materials . Progr Mater Sci Nature ’ s hierarchical materials,” no. January 2015, 2007, doi: 10.1016/j.pmatsci.2007.06.001.

[68] K. I. Jang *et al.*, “Soft network composite materials with deterministic and bio-inspired designs,” *Nat. Commun.*, vol. 6, no. 1, p. 6566, 2015, doi: 10.1038/ncomms7566.

[69] Y. Ma , *et al.* “Design and application of ‘{J}-shaped’ stress-strain behavior in stretchable electronics: a review,” *Lab Chip*, vol. 17, no. 10, pp. 1689–1704, 2017, doi: 10.1039/c7lc00289k.

[70] J. A. Rogers *et al.* “Materials and Mechanics for Stretchable Electronics,” *Science (80-.).*, vol. 327, pp. 1603–1608, 2010.

[71] M. Kaltenbrunner *et al.*, “An ultra-lightweight design for imperceptible plastic electronics,” *Nature*, vol. 499, no. 7459, pp. 458–463, 2013, doi: 10.1038/nature12314.

[72] C. S. Haines *et al.*, “Artificial muscles from fishing line and sewing thread,” *Science (80-.).*, vol. 343, no. 6173, pp. 868–872, 2014, doi: 10.1126/science.1246906.

[73] R. M. Erb *et al.*, “Locally Reinforced Polymer-Based Composites for Elastic Electronics,” *Appl. Mater.*, vol. 4, p. 2860−2864, 2012.

[74] R. Libanori , *et al.* “Hierarchical reinforcement of polyurethane-based composites with inorganic micro- and nanoplatelets,” *Compos. Sci. Technol.*, vol. 72, no. 3, pp. 435–445, 2012, doi: 10.1016/j.compscitech.2011.12.005.

[75] Y. Liu *et al.* “Lab-on-Skin: A Review of Flexible and Stretchable Electronics for Wearable Health Monitoring,” *ACS Nano*, vol. 11, pp. 9614–9635, 2017, doi: 10.1021/acsnano.7b04898.

[76] D. P. Skinner *et al.* “Flexible composite transducers,” *Mater. Res. Bull.*, vol. 13, pp. 599–607, 1978.

[77] Z. Huang, *et al.* "A review on polymer nanofibers by electrospinning and their applications in nanocomposites," *Compos. Sci. Technol.*, vol. 63, pp. 2223–2253, 2003, doi: 10.1016/S0266-3538(03)00178-7.

[78] L. M. Swallow , *et al.* "A piezoelectric fibre composite based energy harvesting device for potential," 2008, doi: 10.1088/0964-1726/17/2/025017.

[79] M. T. Chorsi *et al.*, "Piezoelectric Biomaterials for Sensors and Actuators," *Adv. Mater.*, vol. 1802084, pp. 1–15, 2019, doi: 10.1002/adma.201802084.

[80] S. Hiboux *et al.* "Domain and lattice contributions to dielectric and piezoelectric properties of Pb(Zrx,Ti1-x)O3 thin films as a function of composition," *J. Mater. Res.*, vol. 14, no. 11, pp. 4307–4318, 1999, doi: 10.1557/JMR.1999.0584.

[81] P. Papet *et al.* "Structural Transformation and Pressure-Induced Phase Transitions in PZT," *J. Electroceramics*, vol. 13, pp. 311–314, 2004.

[82] J. Rouquette *et al.*, "Pressure tuning of the morphotropic phase boundary in piezoelectric lead zirconate titanate," *Phys. Rev. B*, vol. 70, pp. 5–8, 2004, doi: 10.1103/PhysRevB.70.014108.

[83] N. Izyumskaya , *et al.* "Processing, structure, properties, and applications of PZT thin films," *Crit. Rev. Solid State Mater. Sci.*, vol. 32, no. 3–4, pp. 111–202, 2007, doi: 10.1080/10408430701707347.

[84] J. Pérez *et al.* "Sol-gel reaction stability studied: Influence in the formation temperature and properties of ferroelectric thin films," *Mater. Res. Bull.*, vol. 44, no. 3, pp. 515–521, 2009, doi: 10.1016/j.materresbull.2008.07.010.

[85] Y. Tai , *et al.* "Modulation of piezoelectric properties in electrospun PLLA nanofibers for application-specific self-powered stem cell culture platforms," *Nano Energy*, vol. 89, no. PB, p. 106444, 2021, doi: 10.1016/j.nanoen.2021.106444.

[86] V. F. Cardoso , *et al.* "Fluorinated polymers as smart materials for advanced biomedical applications," *Polymers (Basel).*, vol. 10, no. 2, pp. 1–26, 2018, doi: 10.3390/polym10020161.

[87] A. Taguet , *et al.* "Crosslinking of vinylidene fluoride-containing fluoropolymers," *Adv. Polym. Sci.*, vol. 184, no. July, pp. 127–211, 2005, doi: 10.1007/b136245.

[88] J. Zheng, A. He, J. Li, and C. C. Han, "Polymorphism control of poly(vinylidene fluoride) through electrospinning," *Macromol. Rapid Commun.*, vol. 28, no. 22, pp. 2159–2162, 2007, doi: 10.1002/marc.200700544.

[89] N. Meng *et al.*, "Multiscale understanding of electric polarization in poly(vinylidene fluoride)-based ferroelectric polymers," *J. Mater. Chem. C*, vol. 8, no. 46, pp. 16436–

16442, 2020, doi: 10.1039/d0tc04310a.

[90] N. A. Shepelin *et al.*, "New developments in composites, copolymer technologies and processing techniques for flexible fluoropolymer piezoelectric generators for efficient energy harvesting," *Energy Environ. Sci.*, vol. 12, no. 4, pp. 1143–1176, 2019, doi: 10.1039/c8ee03006e.

[91] P. Martins *et al.* "Electroactive phases of poly(vinylidene fluoride): Determination, processing and applications," *Prog. Polym. Sci.*, vol. 39, no. 4, pp. 683–706, 2014, doi: 10.1016/j.progpolymsci.2013.07.006.

[92] C. Wan *et al.* "Multiscale-structuring of polyvinylidene fluoride for energy harvesting: the impact of molecular-, micro- and macro-structure," *J. Mater. Chem. A*, vol. 5, no. 7, pp. 3091–3128, 2017, doi: 10.1039/c6ta09590a.

[93] Gulnur Kalimuldina *et al.* "A Review of Piezoelectric PVDF Film by Electrospinning and Its Applications," *sensor*, vol. 20, no. 5214, 2020.

[94] W. Xia *et al.* "Crystalline properties dependence of dielectric and energy storage properties of poly(vinylidene fluoride-chlorotrifluoroethylene)," *Appl. Phys. Lett.*, vol. 97, no. 22, pp. 1–4, 2010, doi: 10.1063/1.3518921.

[95] F. Oliveira , *et al.* "Process influences on the structure, piezoelectric, and gas-barrier properties of PVDF-TrFE copolymer," *J. Polym. Sci. Part B Polym. Phys.*, vol. 52, no. 7, pp. 496–506, 2014, doi: 10.1002/polb.23443.

[96] Y. Murata a *et al.* "Curie transition in copolymers of vinylidene fluoride and tetrafluoroethylene," *Polym. J.*, vol. 17, no. 9, pp. 1071–1074, 1985, doi: 10.1295/polymj.17.1071.

[97] B. Ameduri *et al.* "From vinylidene fluoride (VDF) to the applications of VDF-Containing polymers and copolymers: Recent developments and future trends," *Chem. Rev.*, vol. 109, no. 12, pp. 6632–6686, 2009, doi: 10.1021/cr800187m.

[98] R. Bagherzadeh *et al.* "A theoretical analysis and prediction of pore size and pore size distribution in electrospun multilayer nanofibrous materials," *J. Biomed. Mater. Res. - Part A*, vol. 101 A, no. 7, pp. 2107–2117, 2013, doi: 10.1002/jbm.a.34487.

[99] S. Megelski *et al.* "Micro- and nanostructured surface morphology on electrospun polymer fibers," *Macromolecules*, vol. 35, no. 22, pp. 8456–8466, 2002, doi: 10.1021/ma020444a.

[100] J. Doshi *et al.* "Electrospinning process and applications of electrospun fibers," *Conf. Rec. - IAS Annu. Meet. (IEEE Ind. Appl. Soc.*, vol. 3, pp. 1698–1703, 1993, doi:

10.1109/ias.1993.299067.

[101] G. Yi *et al.* "An acetic acid/water based sol-gel PZT process I: Modification of Zr and Ti alkoxides with acetic acid," *J. Sol-Gel Sci. Technol.*, vol. 6, no. 1, pp. 65–74, 1996, doi: 10.1007/BF00402590.

[102] T. I. Chang, *et al.* "Thermal behaviors and phase evolution of lead zirconate titanate prepared by sol-gel processing: The role of the pyrolysis time before calcination," *J. Am. Ceram. Soc.*, vol. 91, no. 8, pp. 2545–2552, 2008, doi: 10.1111/j.1551-2916.2008.02522.x.

[103] N. Dharmaraj, *et al.* "Pb($Zr_{0.5}$, $Ti_{0.5}$)O_3 nanofibres by electrospinning," *Mater. Lett.*, vol. 59, no. 24–25, pp. 3085–3089, 2005, doi: 10.1016/j.matlet.2005.05.040.

[104] J. S. Yun *et al.*, "The effect of PVP contents on the fiber morphology and piezoelectric characteristics of PZT nanofibers prepared by electrospinning," *Mater. Lett.*, vol. 137, pp. 178–181, 2014, doi: 10.1016/j.matlet.2014.08.139.

[105] O. Rozent *et al.* "Deformation Control during Thermal Treatment of Electrospun $PbZr_{0.52}Ti_{0.48}O_3$ Nanofiber Mats," *J. Am. Ceram. Soc.*, vol. 99, no. 5, pp. 1550–1556, 2016, doi: 10.1111/jace.14203.

[106] A. G. Gevorkyan *et al.* "Thermochimica Acta Rapid thermal processing of electrospun $PbZr_{0.52}Ti_{0.48}O_3$ nano fi bers," *Thermochim. Acta*, vol. 605, pp. 107–114, 2015.

[107] J. Wang *et al.*, "Fabrication and characterization of size-controlled single-crystal-like PZT nanofibers by sol-gel based electrospinning," *J. Alloys Compd.*, vol. 579, pp. 617–621, 2013, doi: 10.1016/j.jallcom.2013.07.099.

[108] T. M. Brugo *et al.*, "Self-sensing hybrid composite laminate by piezoelectric nanofibers interleaving," *Compos. Part B Eng.*, vol. 212, no. October 2020, p. 108673, 2021, doi: 10.1016/j.compositesb.2021.108673.

[109] R. A. Assink *et al.* "1H and 13C NMR Investigations of Pb(Zr,Ti)O3 Thin-Film Precursor Solutions," *Chem. Rev.*, vol. 5, no. 17, pp. 511–517, 1993.

[110] G. Yi *et al.* "An acetic acid/water based sol-gel PZT process II: Formation of a water based solution," *J. Sol-Gel Sci. Technol.*, vol. 6, no. 1, pp. 75–82, 1996, doi: 10.1007/BF00402591.

[111] A. Suárez-Gómez *et al.* "A Crystallization Study of Nanocrystalline PZT 53/47 Granular Arrays Using a Sol-Gel Based Precursor," *J. Mater. Sci. Technol.*, vol. 27, no. 6, pp. 489–496, 2011, doi: 10.1016/S1005-0302(11)60096-0.

[112] J. Ma *et al.* "Deposition and packing study of sub-micron PZT ceramics using electrophoretic deposition," *Mater. Lett.*, vol. 56, no. 5, pp. 721–727, 2002, doi:

10.1016/S0167-577X(02)00602-X.

[113] A. Suárez-Gómez *et al.* "The effects of aging and concentration on some interesting Sol-gel parameters: A feasibility study for PZT nanoparticles insertion on in-house prepared PAA matrices via electrophoresis," *J. Electroceramics*, vol. 22, no. 1–3, pp. 136–144, 2009, doi: 10.1007/s10832-007-9367-0.

[114] A. Wu *et al.* "Sol-gel preparation of lead zirconate titanate powders and ceramics: Effect of alkoxide stabilizers and lead precursors," *J. Am. Ceram. Soc.*, vol. 83, no. 6, pp. 1379–1385, 2000, doi: 10.1111/j.1151-2916.2000.tb01397.x.

[115] D. L. Perry *et al.* "Synthesis of high-purity α- And β-PbO and possible applications to synthesis and processing of other lead oxide materials," *Appl. Phys. A Mater. Sci. Process.*, vol. 89, no. 1, pp. 77–80, 2007, doi: 10.1007/s00339-007-4073-y.

[116] J. He *et al.* "A high-resolution flexible sensor array based on PZT nanofibers," *Nanotechnology*, vol. 31, no. 155503, p. 10, 2020.

[117] E. Mensur Alkoy, *et al.* "Processing conditions and aging effect on the morphology of PZT electrospun nanofibers, and dielectric properties of the resulting 3-3 PZT/polymer composite," *J. Am. Ceram. Soc.*, vol. 92, no. 11, pp. 2566–2570, 2009, doi: 10.1111/j.1551-2916.2009.03261.x.

[118] X. Shen, *et al.* "Fabrication and magnetic properties of composite Ni0.5Zn 0.5Fe_2O_4/Pb($Zr_{0.52}$Ti $_{0.48}$)O3 nanofibers by electrospinning," *J. Wuhan Univ. Technol. Mater. Sci. Ed.*, vol. 26, no. 3, pp. 384–387, 2011, doi: 10.1007/s11595-011-0234-0.

[119] M. Fan *et al.*, "Fabrication and piezoresponse of electrospun ultra-fine Pb(Zr 0.3, Ti 0.7)O 3 nanofibers," *Microelectron. Eng.*, vol. 98, pp. 371–373, 2012, doi: 10.1016/j.mee.2012.07.026.

[120] B. Rimez, *et al.* "The thermal degradation of poly(vinyl acetate) and poly(ethylene-co-vinyl acetate), Part I: Experimental study of the degradation mechanism," *Polym. Degrad. Stab.*, vol. 93, no. 4, pp. 800–810, 2008, doi: 10.1016/j.polymdegradstab.2008.01.010.

[121] B. Rimez *et al.* "The thermal degradation of poly(vinyl acetate) and poly(ethylene-co-vinyl acetate), Part II: Modelling the degradation kinetics," *Polym. Degrad. Stab.*, vol. 93, no. 6, pp. 1222–1230, 2008, doi: 10.1016/j.polymdegradstab.2008.01.021.

[122] D. Joly *et al.* "Electrospun materials for solar energy conversion: Innovations and trends," *J. Mater. Chem. C*, vol. 4, no. 43, pp. 10173–10197, 2016, doi: 10.1039/c6tc00702c.

[123] Y. Wang *et al.* "Synthesis and characterization of micro/nanoscopic Pb (Zr 0.52Ti0.48)O3 fibers by electrospinning," *Appl. Phys. A Mater. Sci. Process.*, vol. 78, no. 7, pp. 1043–1047, 2004, doi: 10.1007/s00339-003-2152-2.

[124] R. Bel-Hadj-Tahar *et al.* "Thermal analysis of the crystallization kinetics of lead zirconate titanate powders prepared via sol–gel route," *J. Therm. Anal. Calorim.*, vol. 144, no. 1, pp. 127–138, 2021, doi: 10.1007/s10973-020-09439-8.

[125] A. Sachdeva *et al.* "Synthesis and characterization of sol-gel derived PZT nano powder," *J. Nanosci. Nanotechnol.*, vol. 9, no. 11, pp. 6631–6636, 2009, doi: 10.1166/jnn.2009.1314.

[126] A. I. Kingon , *et al.* "The control of composition, microstructure and properties of Pb(Zr, Ti)O3 ceramics," *Mater. Sci. Eng.*, vol. 71, no. C, pp. 391–397, 1985, doi: 10.1016/0025-5416(85)90258-7.

[127] J. Yan *et al.*, "Polymer Template Synthesis of Flexible BaTiO3 Crystal Nanofibers," *Adv. Funct. Mater.*, vol. 1907919, pp. 1–9, 2019, doi: 10.1002/adfm.201907919.

[128] R. Bel *et al.* "Thermal analysis of the crystallization kinetics of lead zirconate titanate powders prepared via sol – gel route," *J. Therm. Anal. Calorim.*, vol. 144, no. 1, pp. 127–138, 2021, doi: 10.1007/s10973-020-09439-8.

[129] P. Muralt, "Texture control and seeded nucleation of nanosize structures of ferroelectric thin films," *J. Appl. Phys.*, vol. 100, p. 051605, 2007, doi: 10.1063/1.2337362.

[130] M. Khajelakzay *et al.* "Synthesis and characterization of Pb(Zr 0.52, Ti0.48)O 3 nanofibers by electrospinning, and dielectric properties of PZT-Resin composite," *Mater. Lett.*, vol. 75, pp. 61–64, 2012, doi: 10.1016/j.matlet.2012.01.082.

[131] R. Newnham *et al.* "Connectivity and piezoelectric-pyroelectric composites," *Mater. Res. Bull.*, vol. 13, pp. 525–536, 1978.

[132] M. Serridge *et al. Piezoelectric Accelerometers and Vibration Preamplifiers: Theory and Application Handbook*. Bruel & Kjaer, 1987.

[133] H. Naderiallaf *et al.* "Designing a HVDC Insulation System to Endure Electrical and Thermal Stresses under Operation. Part I: Partial Discharge Magnitude and Repetition Rate during Transients and in DC Steady State," *IEEE Access*, vol. 9, pp. 35730–35739, 2021, doi: 10.1109/ACCESS.2021.3062440.

[134] G. Selleri *et al.*, "Study on the polarization process for piezoelectric nanofibrous layers," 2021, pp. 31–34.

[135] H. Naderiallaf *et al.* "On the calculation of the dielectric time constant of DC insulators containing cavities," 2021.

[136] T. Wongwirat *et al.*, "Origins of Electrostriction in Poly(vinylidene fluoride)-Based Ferroelectric Polymers," *Macromolecules*, vol. 53, no. 24, pp. 10942–10954, 2020, doi: 10.1021/acs.macromol.0c02083.

[137] K. J. Kim *et al.* "Curie Transition, Ferroelectric Crystal Structure, and Ferroelectricity of a VDF/TrFE (75/ 25) Copolymer 1. The Effect of the Consecutive Annealing in the Ferroelectric State on Curie Transition and Ferroelectric Crystal Structure," *Polymer (Guildf).*, vol. 32, pp. 2435–2444, 1994.

[138] E. Ghafari *et al.* "Self-polarized electrospun polyvinylidene fluoride (PVDF) nanofiber for sensing applications," *Compos. Part B Eng.*, vol. 160, no. October 2018, pp. 1–9, 2019, doi: 10.1016/j.compositesb.2018.10.011.

[139] S. Park, *et al.* "Poling-free spinning process of manufacturing piezoelectric yarns for textile applications," *Mater. Des.*, vol. 179, p. 107889, 2019, doi: 10.1016/j.matdes.2019.107889.

[140] F. Calavalle *et al.* "Piezoelectric and Electrostatic Properties of Electrospun PVDF-TrFE Nanofibers and their Role in Electromechanical Transduction in Nanogenerators and Strain Sensors," *Macromol. Mater. Eng.*, vol. 305, no. 7, pp. 1–8, 2020, doi: 10.1002/mame.202000162.

[141] A. Toncheva *et al.* "Polylactide (PLA) -Based Electrospun Fibrous Materials Containing Ionic Drugs as Wound Dressing Materials : A Review Polylactide (PLA) -Based Electrospun Fibrous Materials Containing Ionic Drugs as Wound Dressing Materials : A Review," *Int. J. Polym. Mater. Polym. Biomater.*, vol. 63, no. 657–671, 2014, doi: 10.1080/00914037.2013.854240.

[142] E. R. Pavlova *et al.*, "Tuning the properties of electrospun polylactide mats by ethanol treatment," *Mater. Des.*, vol. 181, p. 108061, 2019, doi: 10.1016/j.matdes.2019.108061.

[143] X. Monnier *et al.* "Molecular dynamics in electrospun amorphous plasticized polylactide fi bers," *Polymer (Guildf).*, vol. 73, pp. 68–78, 2015.

[144] R. Inai, *et al.* "Structure and properties of electrospun PLLA single nanofibres," *Nanotechnology*, vol. 16, no. 2, pp. 208–213, 2005, doi: 10.1088/0957-4484/16/2/005.

[145] X. S. Zong *et al.* "Structure and process relationship of electrospun bioabsorbable nanofiber membranes," *Polymer (Guildf).*, vol. 43, pp. 4403–4412, 2002, doi: 10.1016/S0032-3861(02)00275-6.

[146] G. Perego *et al.* "Effect of Molecular Weight and Crystallinity on Poly (lactic acid) Mechanical Properties," *J. Appl. Polym. Sci.*, vol. 59, no. 1, pp. 37–43, 1996.

[147] L. Dobircau *et al.*, “Molecular mobility and physical ageing of plasticized poly(lactide),” *Polym. Eng. \& Sci.*, vol. 55, no. 4, pp. 858–865, Apr. 2015, doi: 10.1002/pen.23952.